Hydrogen trapping and embrittlement in metals – A review

Yi-Sheng Chen [a,b,c,*], Chao Huang [a,b], Pang-Yu Liu [a,b], Hung-Wei Yen [c,d], Ranming Niu [a,b], Patrick Burr [e], Katie L. Moore [f,g], Emilio Martínez-Pañeda [h,j], Andrej Atrens [i], Julie M. Cairney [a,b,**]

[a] Australian Centre for Microscopy and Microanalysis, The University of Sydney, Australia
[b] School of Aerospace, Mechanical and Mechatronic Engineering, The University of Sydney, Australia
[c] Department of Materials Science and Engineering, National Taiwan University, Taiwan
[d] Advanced Research Center for Green Materials Science and Technology, National Taiwan University, Taiwan
[e] School Mechanical and Manufacturing Engineering, University of New South Wales, Australia
[f] Department of Materials, The University of Manchester, United Kingdom
[g] Photon Science Institute, The University of Manchester, United Kingdom
[h] Department of Civil and Environmental Engineering, Imperial College London, United Kingdom
[i] School of Mechanical and Mining Engineering, The University of Queensland, St Lucia, 4072, Australia
[j] Department of Engineering Science, The University of Oxford, United Kingdom

ARTICLE INFO

ABSTRACT

Hydrogen embrittlement in metals (HE) is a serious challenge for the use of high strength materials in engineering practice and a major barrier to the use of hydrogen for global decarbonization. Here we describe the factors and variables that determine HE susceptibility and provide an overview of the latest understanding of HE mechanisms. We discuss hydrogen uptake and how it can be managed. We summarize hydrogen trapping and the techniques used for its characterization. We also review literature that argues that hydrogen trapping can be used to decrease HE susceptibility. We discuss the future research that is required to advance the understanding of HE and hydrogen trapping and to develop HE-resistant alloys.

1. Introduction

Hydrogen (H), the simplest and the most abundant element in the universe, is widely used in industry for chemical processing, including oil refining and the production of ammonia and methanol. It can also be used be used to store, transport, and deliver energy. Recent years have seen a dramatic increase in its use in emerging energy technologies.

The hydrogen molecule (H_2) has an energy density of 120 MJ/kg, which is 3 times higher than that of gasoline and is the highest among all known fuels [1]. Hydrogen electrolysis and hydrogen fuel cells consume and produce electricity on demand, potentially alleviating load-demand issues in intermittent renewable energy grids. Hydrogen fuel can be used for combustion and electrification and is free of intrinsic carbon emission. It can hence facilitate the decarbonization of the transportation sector, which currently depends heavily on fossil fuels. Hydrogen can also serve as a reductant or fuel to decarbonize hard-to-abate high-emission sectors such as steelmaking [2–4]. It is possible to produce hydrogen at scale from a variety of sources, including natural gas, coal, biomass, waste plastics, water electrolysis [5], and nuclear power [6]. Production methods that have a carbon footprint may be combined with carbon capture and storage technologies to reduce the embodied carbon emissions of hydrogen production [1]. Hydrogen is being increasingly considered as an essential commodity to replace fossil fuels [1,5]. Worldwide, national and international initiatives are underway to develop a 'hydrogen economy', including in the USA [5,7], Japan [8], UK [9], Germany [10], Norway [11], Canada [12], China [13], and Australia [14]. However, challenges must be addressed to enable this vision. Hydrogen is flammable in air at a concentration above the lower explosive limit [15] and requires careful handling [1]. Moreover, hydrogen can degrade metallic materials, reducing their fracture toughness, fatigue resistance and ductility. This effect is called hydrogen embrittlement (HE).

HE is one of the biggest obstacles for the deployment of hydrogen energy infrastructure, including the repurposing of natural gas pipelines
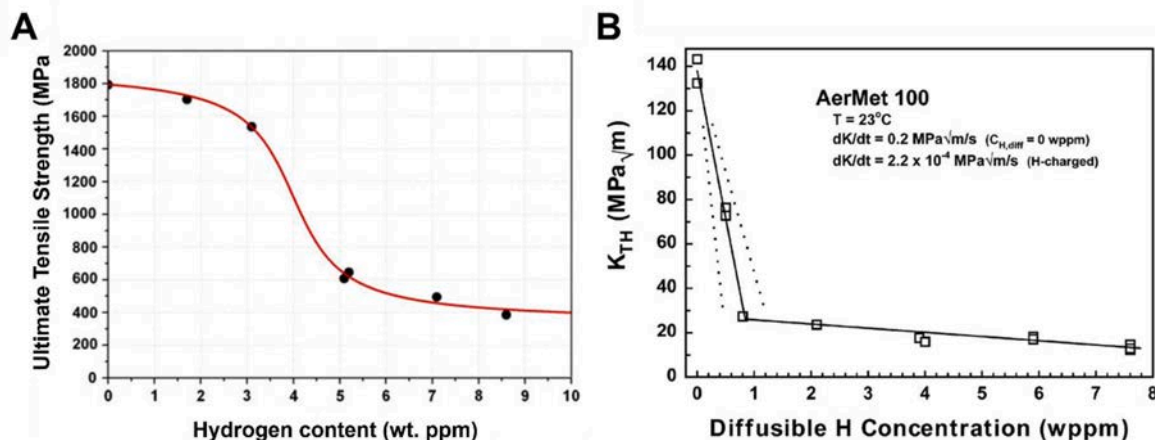
Fig. 1. Hydrogen content in common metals and HE susceptibility. (A) The material notch strength (defined by the ultimate tensile strength) of a hydrogen-charged untempered martensitic steel decreased with increasing hydrogen content, reaching low values for hydrogen contents above 5 wt ppm, reproduced from Ref. [60]. (B) The threshold stress intensity factor (K_{TH}) decreased with increasing diffusible hydrogen content in an AerMet 100 martensitic steel in the near peak aged condition with a nominal 1765 MPa yield strength. Hydrogen was charged with increasing cathodic potential to increase the hydrogen concentration. Reproduced from [62].

for the transport of gaseous hydrogen [5,9,12,14,16–19]. Failure of energy infrastructure due to HE could lead to life-threatening accidents – just one major incident could cause a setback in the worldwide application of hydrogen for decarbonization [20–22]. In fact, a recent Australian national survey testing public acceptance of hydrogen energy indicated that safety is the most important factor in determining people's willingness to use hydrogen [23]. On a 5-point scale where 5 signifies the highest level of importance, 'safety' received an average rating of 4.5, higher than reliability (4.3), cost (4.2), and convenience (3.6). Beyond the energy sector, HE is an ongoing issue for the use of high-strength materials in defense, transport, and construction [24–26].

Although HE is a longstanding industrial problem, in recent years there has been potential mitigation approaches being proposed and verified based on microstructural hydrogen trapping, the advances of which were enabled through the improved characterization and modeling tools. Here we provide a contemporary overview of HE, summarize the latest efforts in using hydrogen trapping for mitigating HE, and outline promising future research directions.

2. Hydrogen embrittlement

Hydrogen can embrittle metals and alloys, a phenomenon that was first reported almost 150 years ago. In 1874, Johnson [27] found significant decreases in the breaking strain of steel and iron specimens after immersion in hydrogen-bearing solutions. This mechanical degradation was recovered after the hydrogen was fully desorbed, demonstrating that this degradation was a result of hydrogen uptake. Johnson also found that HE in higher-strength specimens was more significant than for those with similar compositions but with lower strength. Since this report, over 38,000 papers have been published on the subject [28], reflecting the engineering importance, multidisciplinary nature, and complexity of HE. Some previous review articles have provided a description of the HE phenomena and some understanding of the mechanistic causes [16,26,29–59].

Before going into detail, it is necessary to distinguish between internal hydrogen embrittlement (IHE) and environmental hydrogen embrittlement (EHE). IHE refers to hydrogen-induced failure caused by the presence of pre-existing hydrogen in the alloy and is typically limited by hydrogen supply. EHE is the response of the material to hydrogen when a specimen is subject to a mechanical load with simultaneous hydrogen charging. For EHE, the extent of hydrogen uptake depends on the charging time and the hydrogen diffusivity within the material. EHE failure typically initiates at the specimen surface, where environmental

effects are most severe.

2.1. Variables and metrics
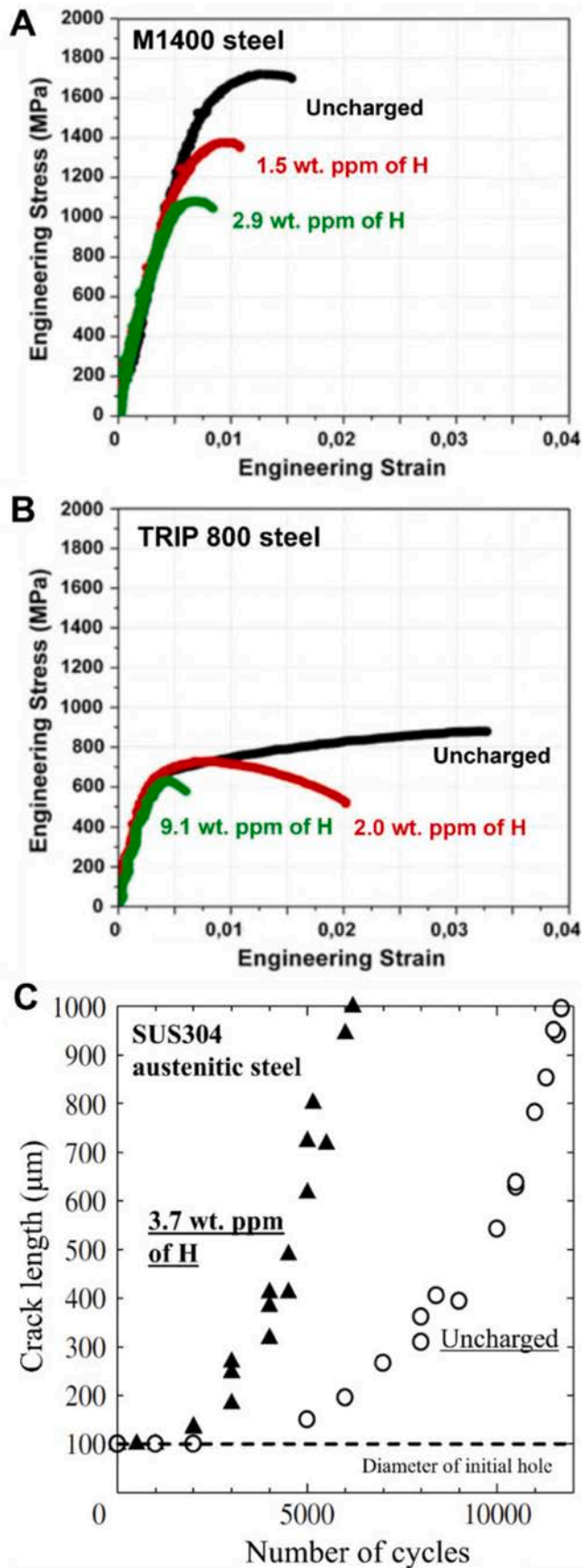
2.1.1. Hydrogen content

HE only occurs when a specimen is subjected to a sufficiently high stress (either applied or residual) and contains a hydrogen content above a critical level, as defined in Fig. 1. The exact critical stress and hydrogen content depend on the type of alloy. Metals that require energy to absorb hydrogen (i.e., endothermic hydrogen solution), such as Fe and Ni, have low hydrogen solubility at ambient temperatures and pressures. These metals generally have a low critical hydrogen content, as low as parts per million in weight (wt. ppm, wppm, or μg/g). Fig. 1A shows the ultimate tensile strength (UTS) of a martensitic steel as a function of hydrogen content. Just 5 wt ppm of hydrogen significantly reduces the UTS, but less than 2 wt ppm has little influence [60]. The hydrogen content in this figure was measured by using hydrogen thermal desorption analysis (TDA) [61] and the notched UTS was determined using a slow strain rate tensile test (SSRT) on ex-situ electrolytically hydrogen-charged specimens [45]. Fig. 1A shows that hydrogen-induced fracture for hydrogen concentrations above 7 wt ppm occurred at approximately 30% of the UTS in the absence of hydrogen. Fig. 1B shows the threshold stress intensity factor for hydrogen assisted cracking (K_{TH}) versus diffusible hydrogen content for a martensitic steel (AerMet 100) [62], showing decreased K_{TH} with increasing hydrogen content.

The service environment determines the hydrogen content in a material, and its measured HE susceptibility may be low if that environment causes a hydrogen content that is below the critical value for that material. For example, the advanced high-strength steel shown in Fig. 1A is unlikely to experience HE in automotive applications because the hydrogen concentration in service is generally lower than 1 wt ppm [63]. Note also that hydrogen uptake is sensitive to the mechanical stress state, as the solubility depends on the hydrostatic stress [64,65].

2.1.2. Mechanical properties

HE can reduce alloy strength and/or ductility in tensile tests, as shown for two different steels in Fig. 2A and B. Common metrics for HE susceptibility for tensile type specimens are strength and ductility loss:

$$Strength\ loss\ index = \frac{\sigma_{ref} - \sigma_H}{\sigma_{ref}} \tag{1}$$

ARTICLE IN PRESS

Y.-S. Chen et al.   International Journal of Hydrogen Energy xxx (xxxx) xxx

Fig. 2. The effect of HE on strength, ductility, and fatigue resistance. HE of (A) M1400 martensitic steel and (B) TRIP 800 ferritic/bainitic/austenitic showing reduction of UTS and elongation in a slow strain rate test. The samples were ex-situ charged with hydrogen and the hydrogen content was measured by thermal desorption analysis. (A) and (B) are reproduced from Ref. [60]. (C) HE of a SUS304 austenitic steel in a constant-loading fatigue test. The mechanical loading was applied at an amplitude of 280 MPa in both tension and compression and a frequency of 1.2 Hz. (C) is reproduced from Ref. [66].

$$Ductility\ loss\ index = \frac{RA_{ref} - RA_H}{RA_{ref}} \qquad (2)$$

where σ_H (or RA_H) is the strength (or reduction in area) in hydrogen and σ_{ref} (RA_{ref}) is the strength (or reduction in area) in a hydrogen-free condition, typically air or an inert gas. Increased susceptibility to HE is manifested by a lower strength σ_H or reduced ductility RA_H in hydrogen, leading to a larger value for the strength or ductility loss index. HE may also cause faster fatigue crack growth. This is shown in Fig. 2C for an austenitic steel, which required around half the number of cycles in the presence of hydrogen to reach the same crack length as sample without hydrogen [66]. Strength and ductility loss indices are used throughout this paper to compare HE susceptibility, although we note issues with their suitability as HE metrics when the applied stress intensity factor is greater than the threshold stress intensity factor, which can lead to sub-critical crack growth [67–70].

HE can also manifest as hydrogen-induced delayed fracture, which can be characterized by the time-to-fracture in a U-bend test under constant loading, where the time-to-fracture decreases with increasing hydrogen content, stress, and/or strain [71,72]. These tests, which load the specimen below the UTS (hence without immediate failure) indicate that the presence of hydrogen can decrease the threshold stress intensity factor required for crack growth or cause sub-critical cracking for certain stress conditions [31,42,43,73,74]. This type of HE can occur at approximately half of the yield stress with crack velocities up to 10^{-4} m/s [73,74]. A threshold time-to-fracture is generally defined (e.g., 300 h in the case of Fig. 3A) with a given bending radius (R in the insert figure), and this information informs the time required for manufacturing high-strength steel products in the automotive industry. The U-bend test can be used to create a HE fracture map, as shown in Fig. 3B, offering a guide for the manufacturing conditions that would avoid HE.

The effects of hydrogen on alloys are not always detrimental. Exposure to hydrogen occasionally results in an increase in yield strength and ductility, particularly in materials that have higher hydrogen solubility such as face-centered cubic (FCC) iron. An example, shown in Fig. 4A–is an annealed Fe–24Cr–19Ni-0.02C austenitic FCC steel [75]. Fig. 4B shows cup and cone fracture surfaces, consistent with ductile dimple rupture. Higher hydrogen levels led to smaller dimples, indicating that hydrogen facilitated ductile fracture. Hydrogen-induced strengthening was attributed to solid-solution strengthening, and the increased ductility was attributed to the facilitation of mechanical twinning by the hydrogen in solution in the austenite [75,76].

Hydrogen has even been proposed as a temporary alloying element to increase the formability of Ti alloys [77,78]. The Ti alloy is held at a relatively high temperature in hydrogen. The absorbed hydrogen induces a phase transformation from α-Ti (hexagonal close-packed, HCP) to more ductile β-Ti (body-center cubic, BCC). The Ti alloy is then mechanically worked at a high temperature and subsequently, the hydrogen is removed by exposure to a low hydrogen fugacity (in a vacuum or an inert gas).

2.1.3. Fracture mode

The fracture modes of embrittled alloys are normally characterized by taking scanning electron microscope (SEM) images of the fracture surface from above or in cross-section. Examples are presented in Fig. 5A (top view) and B (cross-section), respectively, showing hydrogen-
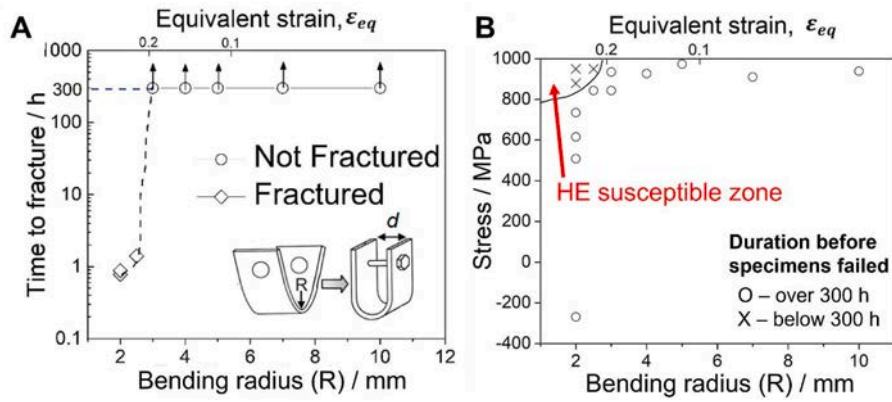
(caption on next column)

ARTICLE IN PRESS

Y.-S. Chen et al. International Journal of Hydrogen Energy xxx (xxxx) xxx

Fig. 3. U-bend test for characterizing H-induced fracture. (A) Time-to-fracture as a function of strain using a 300-h limit. (B) Stress-strain HE fracture map with the stress evaluated by either X-ray measurement or finite element calculation. Reproduced from [71].
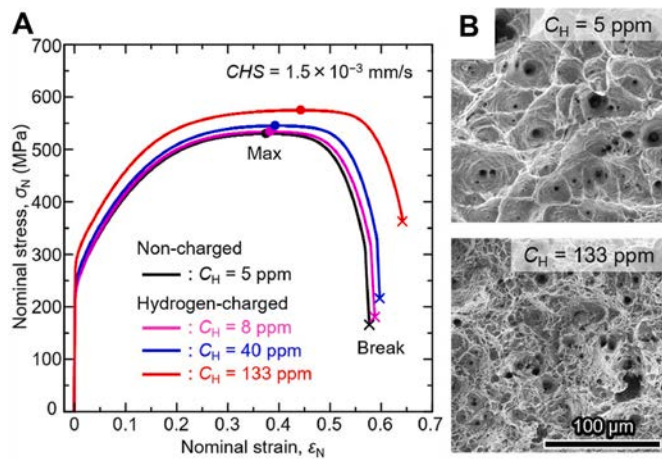

Fig. 4. Hydrogen-induced strengthening and enhanced ductility in an austenitic steel. (A) Stress-strain curves for an annealed Fe–24Cr–19Ni-0.02C austenitic steel with hydrogen concentrations from 5 wt ppm to 133 wt ppm, showing that both strength and ductility increased with increasing hydrogen content. (B) Fractography indicates cup and cone fracture. The specimen with more hydrogen has a smaller dimple size, indicating that hydrogen facilitated the ductile dimple rupture. Reproduced from [75].

induced intergranular fracture along prior-austenite grain boundaries (GBs) in a tempered martensitic steel [31]. Best practice for the examination of fracture surfaces requires observations at a tilted angle and at a high resolution so that critical but subtle HE features can be properly captured and correctly linked with associated mechanisms, as detailed in Section 2.2 [30,31]. For example, Fig. 5C provides a low-magnification image that may be considered as a manifestation of brittle fracture; however, a high-resolution image from the same specimen indicated the presence of fine dimples, as shown in Fig. 5D, indicating some plastic deformation during the hydrogen-induced fracture [79]. HE typically causes a macroscopic loss of ductility; nevertheless, there are many microscopic fracture modes including voiding, brittle fracture, and transgranular quasi-cleavage with micro-ridges as shown in Fig. 5E and F [80]. For ductile fracture, as shown in Fig. 4, increased density of dimples in HE-affected specimens indicates that hydrogen facilitates micro-void nucleation and growth.

2.1.4. Temperature and strain rate

HE susceptibility depends on temperature and is often most severe at close to ambient temperature, as shown in Fig. 6 [81]. The influence of temperature is related to the kinetics of hydrogen diffusion and transport toward susceptible areas in the material microstructure [81,82]. At
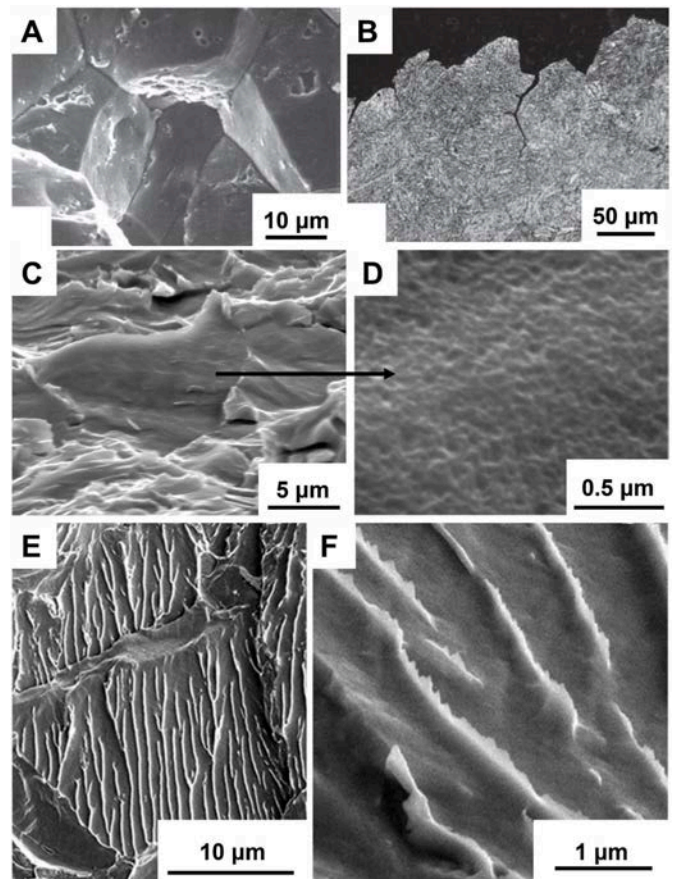

Fig. 5. Fractography of hydrogen-induced macroscopically brittle fractures. (A) and (B) SEM surface and cross-sectional images of a hydrogen-embrittled tempered martensitic steel, showing mainly intergranular failure due to HE. Source: [31]. (C) and (D) low- and high-magnification SEM images of a hydrogen-embrittled API X60 pipeline steel, showing how tilting and high-resolution imaging reveals dimples on the fracture surface. Source: [66]. (E) and (F) low and high magnification SEM images of a hydrogen-embrittled API X60 pipeline steel specimen, showing the quasi-cleavage fracture surface and its micro-ridges. Source [80].

a low temperature, hydrogen does not have sufficient mobility to facilitate the diffusion-controlled HE mechanisms that lead to fracture, although HE can still take place through a mechanism that does not require hydrogen diffusion (such as grain boundary decohesion) [83]. At a high temperature, hydrogen is too mobile to be pinned by dislocations.
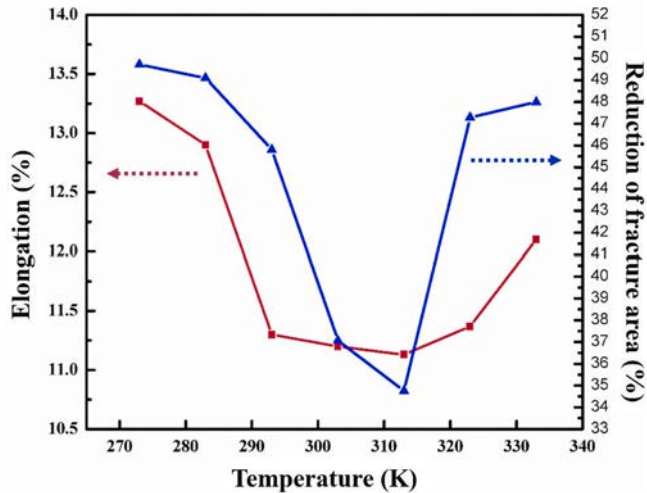
Fig. 6. Temperature window for HE. The extent of HE of hydrogen-charged ferritic/bainitic *X*90 pipeline steel specimens in terms of the reductions of elongation (red) and fracture area (blue). The HE reaches a maximum (300–320 K) close to room temperature (293 K). Properties were measured using slow strain rate tests with continuous hydrogen charging. Reproduced from [81] (For interpretation of the references to color in this figure legend, the reader is referred to the Web version of this article.)

Similar to temperature, the kinetics of hydrogen movement affects HE susceptibility at different strain rates. Fig. 7A shows that, in the presence of hydrogen, the UTS and the elongation (ductility) of a martensitic steel are lower (more susceptible to hydrogen) at low strain rates [84]. Fractographic analysis (Fig. 7B) indicated a higher fraction of the embrittled (intergranular) characteristics at lower strain rates.

2.1.5. Strength

As a rule-of-thumb, within a class of alloys, the alloys with higher strength tend to be more susceptible to HE [31,35]. As such, extreme care should be taken when considering the use of steel with a strength greater than 1 GPa in a hydrogen-containing environment. This strength-susceptibility relationship can be attributed to the strong interaction of hydrogen with crystal defects such as dislocations and GBs, which largely determine the strength of the material [29–31,36,50, 85–88] and higher stresses (and thus hydrogen concentrations) attained in the fracture region [58,89,90]. Correlations of HE susceptibility with dislocation density and grain size, for a wide range of bainitic and martensitic steels with similar strengths, are shown in Fig. 8A and B, respectively.

2.2. Hydrogen embrittlement mechanisms

Many mechanisms have been proposed to explain HE, based on macro- and micro-scale evidence, but agreement has not been reached on a universally applicable mechanism. In recent years it has become increasingly accepted that several mechanisms may operate simultaneously [29–31,56,92]. The mechanisms described here for hydrogen-induced sub-critical crack growth have also been covered in Refs. [29–32,40]. Mechanistic interpretations are used to build predictive models and to provide an explanation for experimental results, particularly for fractography [93–96].

2.2.1. Hydride formation

Westlake proposed in 1969 [97] that HE was the result of brittle hydride formation. This embrittlement mechanism is most relevant to alloy systems that have a high tendency to form hydrides such as Zr [41, 98,99], Nb [100], Ti [41,101], and Mg [38,102,103]. Hydrogen is an interstitial solute in a metal lattice and can rapidly diffuse and segregate
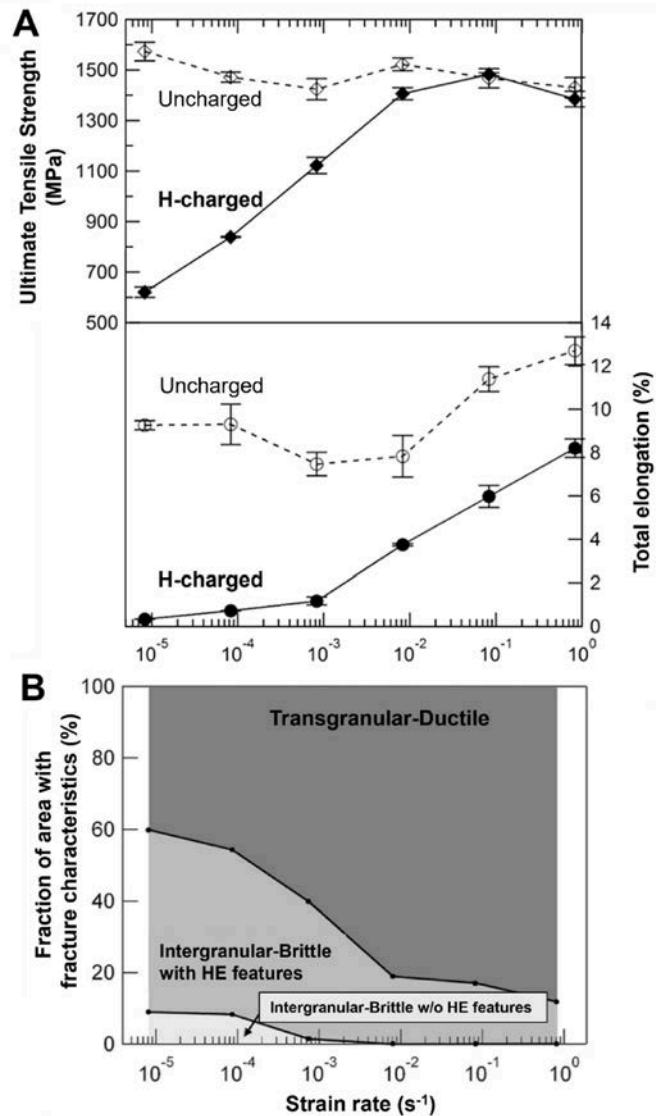

Fig. 7. The effect of strain rate on HE. (A) The UTS and the elongation of hydrogen-charged and uncharged low-carbon martensitic steel specimens decreased with decreasing strain rate in uniaxial tensile tests, showing HE is greater at lower strain rates. (B) Fractographic analysis of the specimens in (A) showing the surface area fraction of ductile and brittle features, indicating a change from transgranular-ductile to intergranular-brittle fracture with decreasing strain rate. Reproduced from [84].

to the zone of high hydrostatic stress at a crack tip (Fig. 9A). Hydrides form when the hydrogen content exceeds the solubility (Fig. 9B), and cleavage of the brittle hydride subsequently occurs along the crystallographic direction on which the hydride forms (Fig. 9C). The crack is arrested when it meets the ductile matrix (Fig. 9C), and another round of this sequence begins. Crack propagation can be further facilitated by the presence of pre-existing hydrides within the microstructure along the crack path.

In hydride-forming alloys with non-isotropic crystal structure, texture engineering can be used to mitigate HE by promoting the formation of hydrides along crystallographic planes that are less detrimental to the embrittlement of the component. This has been extensively used in the hexagonal Zr alloys, where individual nano-sized hydrides preferentially grow on the basal {0001} plane of the hcp α-phase. Macroscopic hydride plates align approximately on the {10–17} habit plane. In these alloys, tubes and plates are manufactured with a strong "split basal" texture where the c-axis of the hcp crystal is
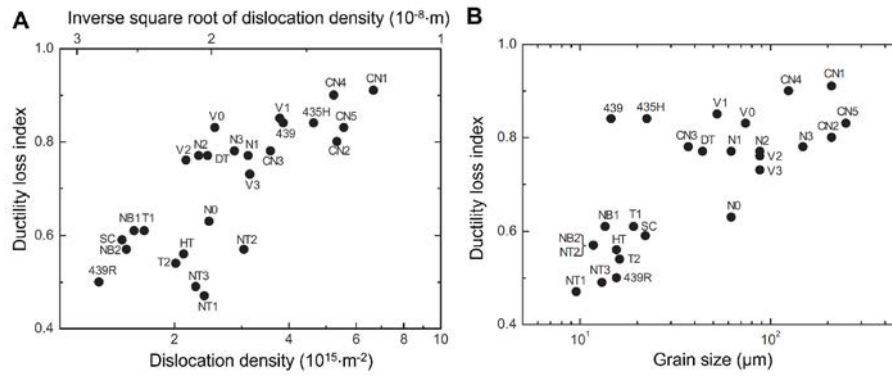
Fig. 8. Dislocation and grain size vs. environmental hydrogen embrittlement susceptibility. Ductility loss index (HE susceptibility, Equation (2)) as a function of (A) dislocation density and (B) grain size in a range of bainitic and martensitic steels with similar strengths (853–1142 MPa). The ductility differences were measured by comparing the SSRT results in a gaseous hydrogen environment of 45 MPa and in air. Reproduced from [91].
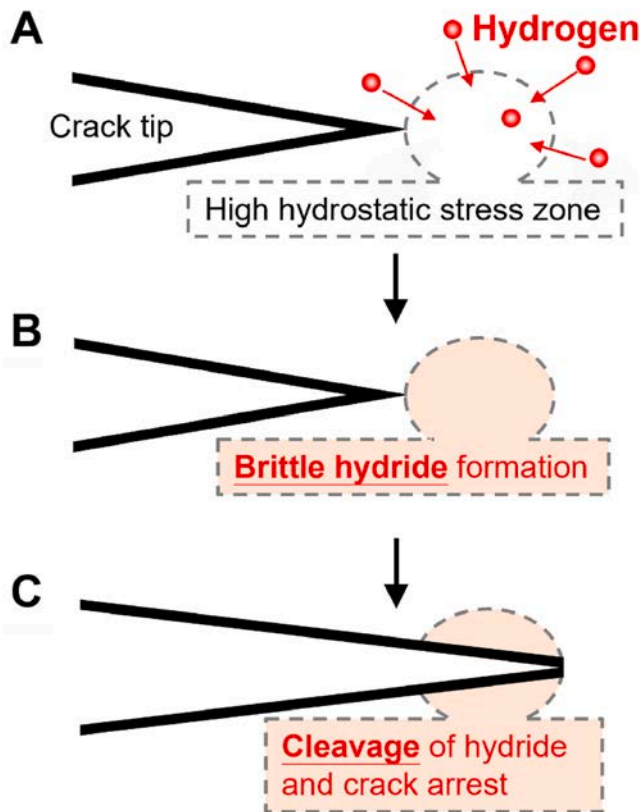

Fig. 9. Schematic of the mechanism of hydride-induced hydrogen cracking for sub-critical crack growth.

predominantly aligned within 30° of the normal direction of rolling, towards the tangential direction. This encourages hydrides to form parallel to the surface, where they pose the least concern for crack growth. One drawback of this mitigation strategy is that the orientation of hydrides also depends on stress fields, thus upon mechanical loading the hydrides may re-orient across the thickness of the plate or tube, especially after a thermal cycle in which the hydrides are partially or fully dissolved and then re-precipitate upon cooling [98,99].

For non-hydride forming alloys such as Fe or Ni, theoretical models have attempted to relate their transgranular and intergranular failures of HE with the presence of hydrides [104–107]. However, hydride formation at ambient temperature in these alloy systems requires extremely high hydrogen fugacities (e.g., 3.5 GPa for iron [108]), which

are unlikely to be relevant in most service conditions.

2.2.2. Hydrogen-enhanced decohesion

In the 1960s and 1970s, Troiano and Oriani proposed the theory of hydrogen-enhanced decohesion (HEDE), which postulates that hydrogen can directly reduce the cohesive strength of the atomic bonds in the metal lattice, leading to brittle fracture, as illustrated in Fig. 10A [109,110]. While earlier atomistic studies suggested reductions in fracture energy and cohesive strength of up to 90% [111,112], recent studies suggest that any reduction is limited to 20–40% [113–115]. Given that the lattice/grain boundary strength is roughly 10 times the yield stress, a 20–40% reduction in the cohesive strength is insufficient to trigger decohesion in the context of conventional continuum theories [116]. However, theoretical predictions that account for the role of geometrically necessary dislocations and plastic strain gradients lead to much higher stresses and hydrogen levels at the crack tip [117,118], providing a modern mechanistic rationale for HEDE.

HEDE is most widely accepted in the context of inducing intergranular failure (Fig. 10B) or phase-boundary failure (Fig. 10C) [117,119, 120], particularly for high-strength materials [33,121–125]. Atomistic modeling suggests that the presence of more than one atomic layer of solute segregation can lead to a higher degree of cohesive strength reduction [119]. Experimental evidence of HEDE includes the intergranular failure observed in a hydrogen-charged Ni alloy tested at a cryogenic temperature, where hydrogen-dislocation interactions are effectively suppressed, suggesting that hydrogen-induced GB decohesion is responsible for the HE [83].

2.2.3. Hydrogen-enhanced local plasticity

Hydrogen-enhanced ductile fracture with dimpled fracture surfaces (e.g., Fig. 4B) was described by the hydrogen-enhanced local plasticity (HELP) mechanism by Beachem in 1970s. The theory is that i) interstitial hydrogen atoms concentrate at high tensile hydrostatic stress zones, and ii) hydrogen segregates to lattice defects such as dislocations [126, 127], and increases their mobility [128]. This hydrogen segregation is a 'Cottrell atmosphere', a known effect that reduces the strain energy around dislocations [121,129,130]. Fig. 11 illustrates this process. Facilitation of the generation and motion of dislocations promotes the formation of microvoids and their coalescence, allowing sub-critical hydrogen-induced cracks to propagate, resulting in dimpled fracture surfaces.

The central hypothesis of HELP is that hydrogen atmospheres enhance dislocation mobility (Step 2 in Fig. 11). This was experimentally demonstrated by using an environmental transmission electron microscope (E-TEM) with in-situ mechanical loading on a specimen in a hydrogen atmosphere [128,131,132]. A derivative model of HELP was proposed that associates the crack path with failure along low energy
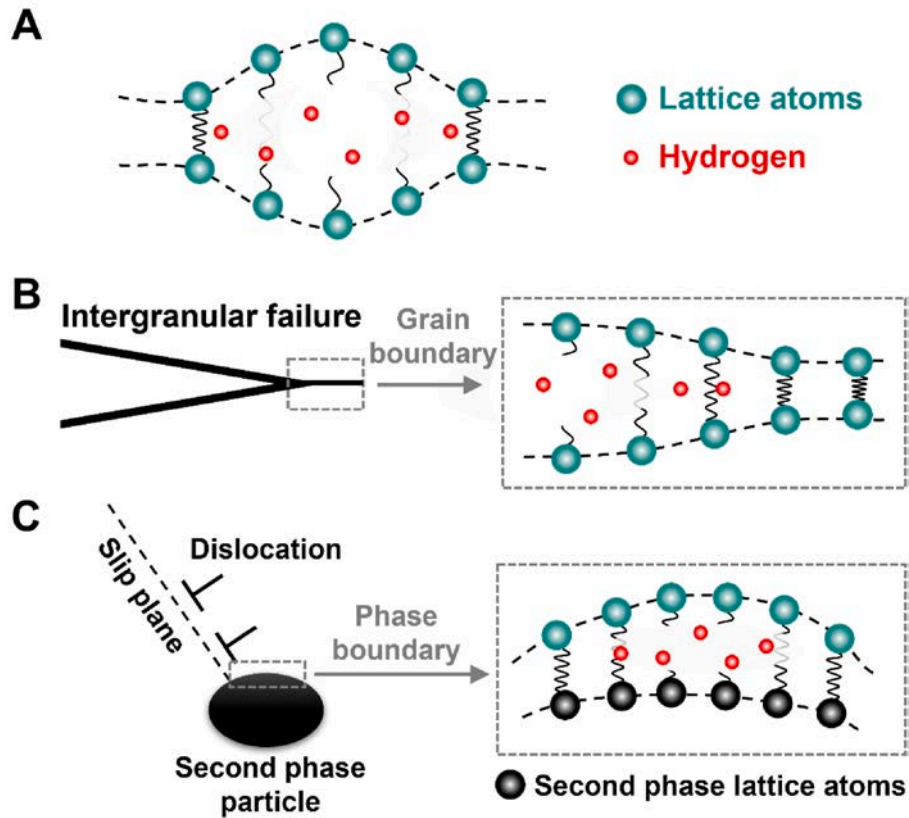
Fig. 10. Schematic of the hydrogen-enhanced decohesion mechanism (A) in the lattice, (B) at a grain boundary, and (C) at a phase boundary.
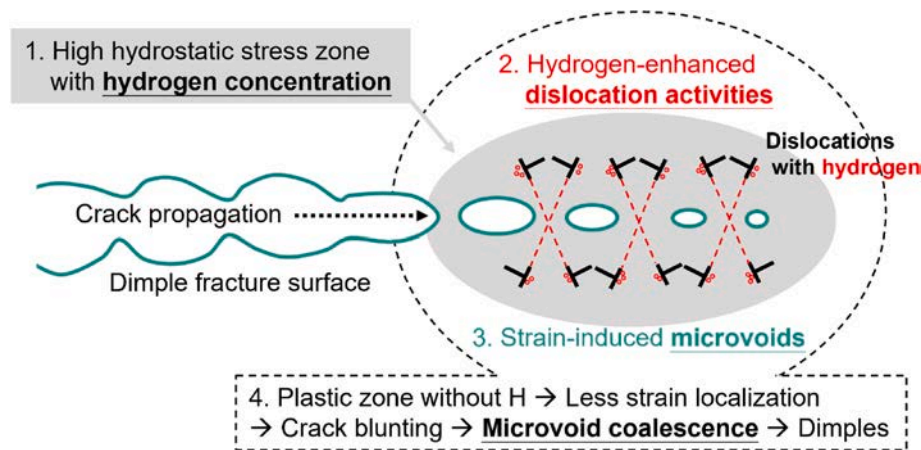

Fig. 11. Schematic of the hydrogen-enhanced local plasticity mechanism.

dislocation cell walls that form as a result of the enhanced dislocation mobility in nanoprecipitation-strengthened steels [92]. Noting here again that grain boundary decohesion can still take place in the absence of hydrogen-dislocation interactions in some systems such as nickel alloys [83]. The HELP mechanism is a qualitative description of the effects that lead to embrittlement and does not directly provide a means of evaluating the extent of HE.

2.2.4. Adsorption-induced dislocation emission

The adsorption-induced dislocation emission (AIDE) mechanism proposed by Lynch describes HE that arises from hydrogen adsorption at the surface, instead of hydrogen in solution in the bulk [31]. Fig. 12 illustrates the mechanism: HE is caused by the hydrogen adsorption in

the metal subsurface [133], which facilitates dislocation activity and boosts dislocation emission from a stressed surface. This dislocation emission facilitates inward strain and leads to the formation of microvoids in the crack-front plastic zone, which coalescence for crack propagation, resulting in a dimpled fracture surface. The AIDE mechanism can explain ductile H-induced crack growth that is induced by an external source of hydrogen, particularly prevalent in specimens with pre-existing surface damage. A similar mechanism, 'hydrogen-assisted micro-fracture', proposed by Atrens and co-workers [134], also attributes HE to the hydrogen effect at specimen surface but stresses that the fracture propagation in the HE of steels (at the UTS) can be as fast as 61–130 m/s, which exceeds the typical velocity of ductile fracture of 46 m/s, suggesting the possible presence of another process that leads to the
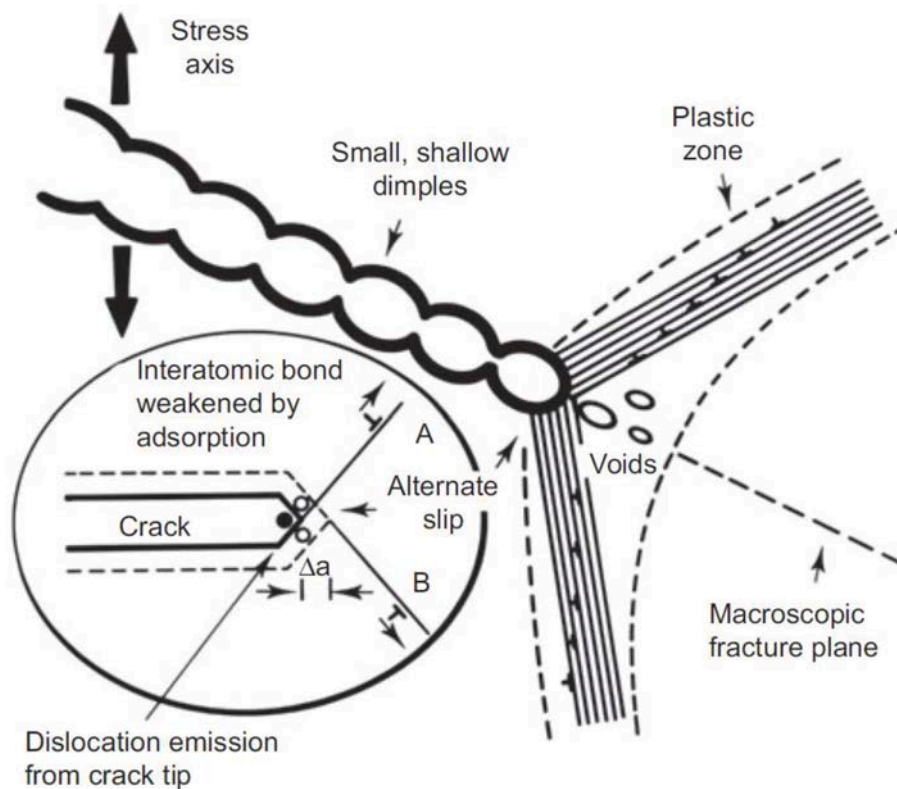
Fig. 12. Schematic of the AIDE mechanism. Reproduced from [31].

bulk HE [135].

2.2.5. Hydrogen-enhanced strain-induced vacancies

Based on the fact that hydrogen facilitates the formation of vacancies [121,129], Nagumo and Takai proposed the mechanism of hydrogen-enhanced strain-induced vacancies (HESIV), which attributes the observed dimpled fracture surface (e.g., Fig. 4B) to an abundance of hydrogen-stabilized vacancies that are transported by hydrogen-activated dislocations and subsequently combined into nano-voids during deformation [47]. Nagumo combined thermal desorption analyses with delicately controlled straining and annealing to introduce and remove vacancies, respectively, in steel specimens. Hydrogen-vacancy interactions were correlated with HE. Positron annihilation spectroscopy, which can detect both hydrogen and vacancies, was also used to provide evidence of the relationship between hydrogen-vacancy interaction and HE [136–138].

2.3. Hydrogen uptake and inhibition

Understanding how hydrogen enters materials, and hydrogen uptake can be inhibited, is essential for developing strategies to reduce HE. This section provides an overview of hydrogen entry, how hydrogen entry can be managed, and introduces methods that relate laboratory test results to HE problems in the field.

2.3.1. Internal hydrogen embrittlement: hydrogen uptake and liberation

Hydrogen is a byproduct of many material fabrication processes, and hydrogen uptake can lead to IHE [130,131]. An example occurs in the application of an aluminum-silicon (Al–Si) alloy coating, a common component of the automotive hot-stamping steels [139–141]. Al and Si oxidation in the presence of ambient moisture produces hydrogen, some of which dissolves into the steel substrate [142]:

$$2Al + 3H_2O \rightarrow Al_2O_3 + 6H \tag{3}$$

$$Si + 2H_2O \rightarrow SiO_2 + 4H \tag{4}$$

This problem is of particular concern in the automotive industry, where high-strength steel is desirable for weight reduction [142]. Another example is the exposure of hot or molten steel to air humidity during steel production. Hydrogen can be generated and absorbed by the steel when the surfaces encounter ambient moisture at high temperatures [112,115]:

$$3Fe + 4H_2O \rightarrow Fe_3O_4 + 8H \tag{5}$$

$$2Fe + 3H_2O \rightarrow Fe_2O_3 + 6H \tag{6}$$

$$Fe + 4H_2O \rightarrow FeO + 8H \tag{7}$$

Other treatments that can lead to hydrogen uptake by steels are acidic pickling, electroplating for chromium [143], zinc or cadmium [144–148], welding [46,149–151], and in-service corrosion [63]. A famous example of HE following electroplating is the catastrophic failure of tightening bolts during the construction of the San Francisco Bay bridge span in California, USA, which cost 40 million US dollars for rectification [152].

Hydrogen uptake during steel production can be removed by pre-service baking [144,153]. For example, baking at 200 °C for 10 min was found to be sufficient to remove the pre-existing hydrogen in a hot-stamped martensitic steel specimens with an Al–Si coating [153]. This approach requires consideration of the effect of the heat treatment on the microstructure and mechanical properties, which may be problematic for some high-strength alloys [145,154].

2.3.2. Environmental hydrogen embrittlement: hydrogen surface entry and inhibition

Hydrogen in the environment absorbed through the metal surface can lead to EHE [155]. The hydrogen supply can be either finite, leading to conditions similar to those of IHE, or infinite (relative to the solubility
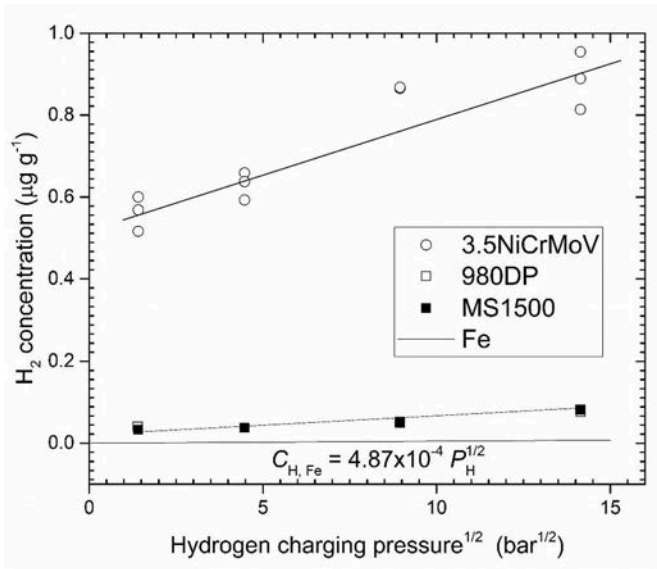
ARTICLE IN PRESS

Y.-S. Chen et al.											International Journal of Hydrogen Energy xxx (xxxx) xxx

Fig. 13. Equilibrium hydrogen concentration versus charging pressure in 3.5NiCrMoV steel, 980DP and MS1500 steels for various pressures of gaseous hydrogen from 1 to 200 bar at room temperature, measured using gaseous hydrogen charging [156–158], compared with literature data for annealed pure Fe [159].
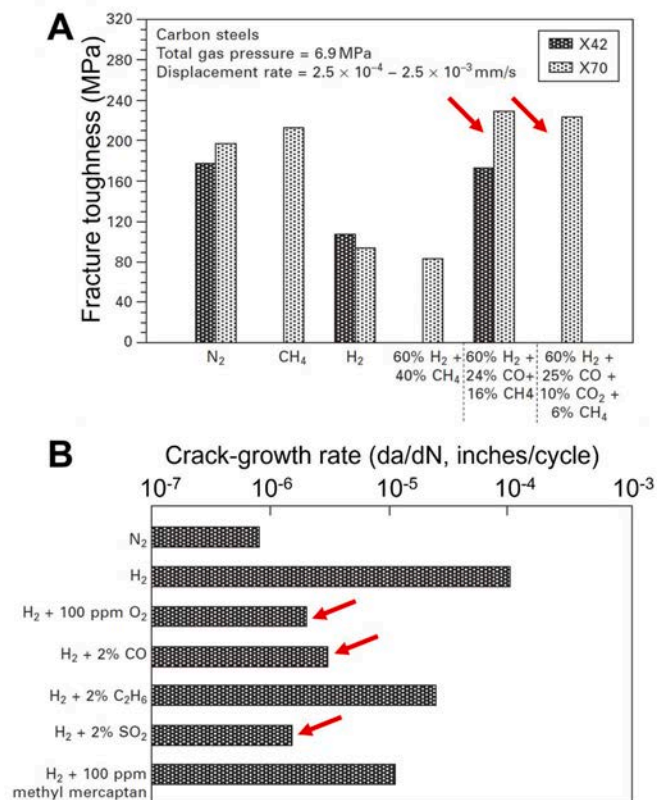

Fig. 14. EHE susceptibilities for pipeline steels exposed to different gas mixtures with hydrogen. (A) The fracture toughness of X42 and X70 pipeline steels and (B) fatigue crack growth of X42 steel in the gases that contain various contents of hydrogen, showing the inhibition of EHE by O_2, CO, SO_2. Reproduced from Ref. [133].

in the material at the relevant fugacity), as is the case for gas transmission pipelines carrying hydrogen. Hydrogen from H_2 gas molecules in the local environment dissociate, adsorb on the surface, and are absorbed into the metal lattice. The process can be formulated as:

$$\frac{1}{2}H_2(g) \leftrightarrow H_{ads} \leftrightarrow H_{abs} \leftrightarrow H_{lattice} \tag{8}$$

The absorbed hydrogen content in the material (c_H) follows the modified Sieverts' law relating to the solubility constant (S), which is specific to the material and its surface condition, the hydrogen pressure or fugacity (f_{H2}) in a material, and the amount of pre-existing and trapped hydrogen (c_T):

$$c_H = c_T + S\sqrt{f_{H_2}} \tag{9}$$

The hydrogen fugacity is the pressure that hydrogen would apply if the hydrogen acted as an ideal gas and is essentially equal to the hydrogen pressure below 200 bar. Fig. 13 indicates that the hydrogen concentration in the steels follows the modified Sieverts' Law for hydrogen pressures up to 200 bar [156–158]. Hydrogen traps are filled rapidly with hydrogen as it becomes available (i.e., at hydrogen pressures less than 1 bar), which explains the apparent y-axis intercept in Equation (9) and Fig. 13. The low hydrogen content in the annealed iron sample indicates that the intrinsic hydrogen solubility in pure iron is quite low, and that the more substantial hydrogen solubility in steels is associated with hydrogen in traps. Sieverts' law, i.e., Equation (9), can be derived using statistical mechanics, as shown in Ref. [156], assuming i) the hydrogen in the steel is in equilibrium with the hydrogen in the gas phase, ii) N_H hydrogen atoms occupy N_S sites in the steel lattice having N_t trap sites; and iii) only one hydrogen atom can occupy each of the N_S sites. Note that in many applications (e.g., pipelines, pressure vessels, pumps) the metal is exposed to H_2 gas for prolonged periods (relative to temperature and fugacity) and the dissociation/adsorption/absorption reaches a dynamic equilibrium (Reaction (8)). This means that hydrogen atoms recombine at the surface and the dissolved hydrogen also desorbs back out of the surface. This is not the case for alloys exposed to transients of high hydrogen fugacity but is the case when the source of environmental hydrogen is from corrosion of the alloy.

In addition to the simplest case of direct contact with gaseous hydrogen, contact with hydrogen-bearing gases such as hydrogen sulfide (H_2S) can also lead to HE [17,44,53,59,160]. For an inert gas like methane, the hydrogen solubility in the steel can be determined by Sieverts' law using the hydrogen partial pressure in the gas phase. The hydrogen solubility is much higher (up to an order of magnitude higher) in the presence of an active gas like hydrogen sulfide that inhibits the recombination of hydrogen atoms into hydrogen molecules at the metal surface, thereby increasing the hydrogen fugacity at the metal surface. For this reason, HE due to hydrogen sulfide is a major concern in gas and oil pipes. The usual approach to tackle H_2S embrittlement is to impose a hydrogen gas pressure in service that is one or several orders of magnitude lower than the level that causes HE [161]. An alternative approach is to use thicker pipe walls of low-strength steels that are less susceptible to HE, but this can lead to reduced gas transmission efficiency and results in higher weight and installation costs [161].

In contrast, some gases such as oxygen (O_2), carbon monoxide (CO), and sulfur dioxide (SO_2) can inhibit EHE. Fig. 14A shows that the fracture toughness of X42 and X72 steels in gaseous hydrogen was significantly lower than that measured in inert gases like N_2 and CH_4. However, when the gases were combined, the fracture toughness in hydrogen + CO (indicated by the red arrows) was similar to the fracture toughness in an inert gas, indicating that the CO in the gas mixture inhibited EHE [162]. Similarly, Fig. 14B shows that O_2, CO, and SO_2 inhibited hydrogen fatigue crack growth [133]. These inhibitor gases, particularly oxygen, absorb preferentially at active sites on the surface and prevent hydrogen from reaching the steel surface and being adsorbed [163–166]. Based on the compelling laboratory evidence for gas inhibition of EHE, additional research is now required to properly
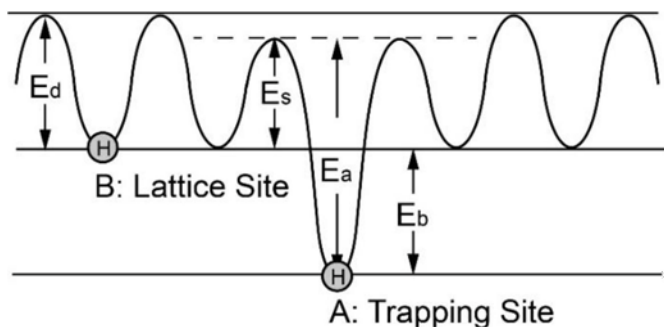
Fig. 15. Schematic energy profile of hydrogen in the lattice and in a trap. Classical lattice diffusion of hydrogen requires E_d to hop between interstitial sites. This may vary near trapping sites to E_s. Detrapping of hydrogen requires an energy of $E_a = E_b + E_s$.

quantify this effect to allow for the use of a gas mixture strategy to address HE problems in gas transmission pipelines.

Surface coatings such as iron oxide and aluminum oxide have also been found to reduce EHE by preventing hydrogen entry [28,167–171]. This approach has the advantage that it can be applied to existing structures. Hydrogen is an effective reductant, so surface oxides tend to be reduced by hydrogen, which may limit the coating life. However, this reduction reaction occurs slowly at room temperature [172]. Metallic coatings and mechanical surface treatments can also be used to increase HE resistance, as demonstrated in Refs. [112,142,173–175], respectively. However, coatings can crack (particularly in aggressive environments), so surface modification is ineffective for abrasive environments such as bearings [28]. In addition, surface diffusion barriers and gas mixtures only reduce the kinetics of hydrogen uptake and do not alter the thermodynamic factors [156]. Unless hydrogen entry kinetics are sufficiently low, materials will eventually become saturated with hydrogen with continuous hydrogen contact, such as in a gas transmission pipeline that might be used for over 30 years.

2.3.3. Laboratory hydrogen charging

Laboratory tests use in-situ (concurrent) and ex-situ (prior) hydrogen charging [31,45] to simulate service environments. In-situ charging during a mechanical test (and often also beforehand to achieve a uniform hydrogen content) is optimal for evaluating HE susceptibility. Ex-situ charging is simpler to achieve in practice, but hydrogen loss can affect the quality of results for materials with high diffusivity or where long-duration tests (e.g., fatigue) are required. Erroneously high HE resistance can result from hydrogen depletion at the surface, where hydrogen cracking typically initiates. During hydrogen charging, surface oxides present on the metal surface may prevent hydrogen uptake, which can be mitigated by an activation procedure.

Gaseous charging generally requires a high pressure and/or high temperature to enable hydrogen uptake [176]. This approach is thus demanding in terms of laboratory safety and equipment. In contrast, cathodic charging requires only an electrolytic cell, which allows the specimen (the cathode) to be charged in an acidic, neutral, or alkaline solution [146]. Cathodic charging allows for easy generation of high fugacity hydrogen (at the level of GPa) within the specimen with an overpotential of less than 1 V [156,177,178]. Much higher hydrogen fugacities are possible if a hydrogen recombination poison is also added to the cathodic charging solution. Depending on the charging parameters, the resulting microstructure can display a strong hydrogen concentration gradient within the samples with a hydrogen-rich (or even hydride) surface and a hydrogen-poor core, thus cathodic charging is often followed by a low-temperature heat treatment to redistribute the hydrogen within the bulk specimen. The simplicity and effectiveness of cathodic charging have led to its widespread use for HE testing [148], despite the fact that quantifying hydrogen uptake is not as

straightforward as it is for gaseous charging. Hydrogen can also be introduced by charging from a plasma [179,180], but this approach is less common and it remains uncertain whether the low pressure required allows for the introduction of sufficient hydrogen to trigger HE [181,182].

To better understand the effective cathodic charging fugacity, Atrens and co-workers developed a method to relate the hydrogen fugacity to the equivalent hydrogen pressure during gaseous charging [156–158, 177]. This approach is based on the assumptions that i) the hydrogen inside the metal has no memory of whether it originates from gaseous charging or cathodic charging and ii) the fugacity during cathodic charging is equivalent to the fugacity during gaseous charging for the same hydrogen concentration. The hydrogen fugacity (f_{H_2}) for pure iron is related to the applied electric potential (E_c) by:

$$f_{H_2} = \alpha \, exp \left[\frac{-\left(E_c - E_H^0\right)F}{\beta RT} \right] \tag{10}$$

where F, R, and T are the Faraday constant, gas constant, and absolute temperature, respectively. E_H^0 is the equilibrium potential of the hydrogen evolution reaction at the sample surface for hydrogen charging at 1 atm of fugacity, hence $(E_c - E_H^0)$ is the overpotential that controls the hydrogen fugacity. The constants α and β relate to the hydrogen evolution reaction (i.e., the acidity of the charging solution) at the sample surface. These constants can be determined for pure iron, which does not have hydrogen traps, based on literature value of the Sieverts' constant S in Equation (9) (Fig. 13). For a steel, the hydrogen solubility data (e.g., Fig. 13 in which hydrogen concentration is measured for each cathodic charging condition) can be used to experimentally establish the relationship between hydrogen content and hydrogen fugacity [177]. These studies have been further improved by electro-chemo-mechanical models that resolve all the reaction rates involved in the hydrogen evolution reaction [183].

This quantification provides the hydrogen fugacity (and equilibrium hydrogen content) at the specimen surface. Time is required to establish a uniform hydrogen concentration throughout the specimen. The penetration of hydrogen can be predicted using hydrogen diffusion equations. Often measurements of the overall hydrogen content in the specimen are used to assess the rate of penetration. In addition to the charging parameters, the hydrogen content in the specimen can be influenced by the surface condition, particularly surface oxides, which can affect the hydrogen uptake [156]. Another important experimental consideration is time-to-test after hydrogen charging, which affects the extent of hydrogen desorption [184]. Even quite short times can alter the measured degree of HE in some materials. Where possible, in-situ charging during mechanical testing is ideal. When reporting HE results using hydrogen charging, it is necessary to give a clear and complete description of the experimental conditions to enable comparison with the literature.

3. Hydrogen trapping

In addition to *extrinsic* approaches to mitigate HE hydrogen by degassing or surface coating, a popular *intrinsic* approach is to introduce additional hydrogen traps into the alloy microstructure. Pressouyre [155] proposed the concept of introducing microstructural hydrogen traps to mitigate HE in the 1980s. Certain microstructural features act as hydrogen traps, which may reduce the amount of hydrogen that is available to reach the crack tip. This concept assumes that the trapped hydrogen is passive and that it is the lattice hydrogen or diffusible hydrogen that leads to HE [27,28,31,32]. However, as shown in Fig. 13, the presence of hydrogen traps increases the solubility of hydrogen in all alloys, including commercial steels, and these sites can therefore provide a future source of hydrogen available for HE.

An optimal microstructure to resist hydrogen embrittlement is one in which the traps do not contribute to embrittlement themselves, nor do
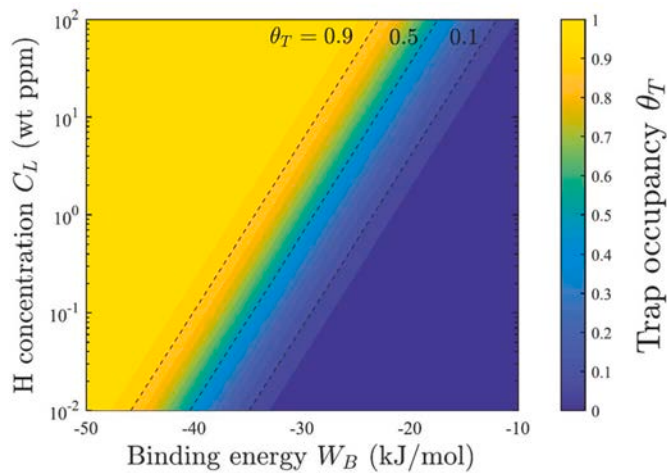
ARTICLE IN PRESS

Y.-S. Chen et al.   International Journal of Hydrogen Energy xxx (xxxx) xxx

Fig. 16. Relationship between hydrogen content and trap occupancy as a function of trapping/binding energy at absolute temperature. As the lattice hydrogen concentration (C_L) increases, traps with low binding energies (W_B) are filled and the trap occupancy (θ_T) increases. Reproduced from [196].
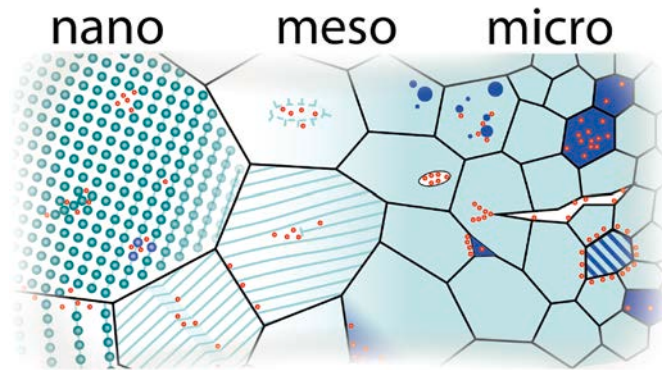

Fig. 17. Illustration of various microstructural hydrogen traps in an alloy. Hydrogen can be trapped at interstitial lattice sites, grain boundaries, vacancies, alloying solutes, stacking faults, twins, dislocations and their cell walls, strain field, voids, second phases and their boundaries, and the free surfaces of microcracks.

they provide an easy source of hydrogen that can contribute to embrittlement effects. Here we review the fundamental understanding of hydrogen trapping in metals and alloys to establish a scientific ground to underpin the design of a HE-resistant microstructure, discussed in the final section.

3.1. Principle

A hydrogen atom in solution in an alloy can either be a free-moving solute in the lattice or it can reside in a trap. Fig. 15 presents the energy states for a hydrogen atom: i) the activation energy needed for classical migration of hydrogen in a lattice site (E_d), ii) the activation energy needed for migration close to a trapping site (E_s), iii) the de-trapping energy needed for a trapped hydrogen atom to diffuse in the lattice (E_a), and iv) the binding energy of the hydrogen atom to a trapping site (E_b). These energies can be understood in terms of a simple reaction model where the rate of detrapping $\frac{dx}{dt}$ is given by Ref. [185]:

$$\frac{dx}{dt} = A(1-x)exp\left(\frac{-E}{RT}\right) \tag{11}$$

where x is the fraction of free (detrapped) hydrogen, and R and T are the gas constant and absolute temperature, respectively.

For BCC structures at room temperature, interstitial hydrogen atoms preferentially occupy tetrahedral sites rather than octahedral sites [186–188]. In FCC alloys at room temperature, hydrogen atoms tend to reside in octahedral sites, which are larger and have lower multiplicity for hydrogen migration [186]. This leads to a lower diffusivity and a larger E_d in FCC crystals (e.g., 44 kJ/mol for FCC iron [189]) compared to other crystal lattices (e.g., 4.5–5.5 kJ/mol for BCC iron [190]).

Negative trapping energies reflect that the hydrogen atom in the potential well of the trap is more stable and remains in the trap longer than it does in a lattice site. Both E_a and E_b in Fig. 15 have been defined as the 'hydrogen trapping energy' in the literature, depending on the measurement techniques. The difference (E_s, differs from E_d) is due to local atomic-structural heterogeneity near the microstructural trap with respect to an ideal lattice, such as the strain field around a dislocation [191]. E_s may also be affected by multiple trapping sites in a single microstructural feature, e.g., the interface and the precipitate structure in second-phase precipitates [192–194].

The value of E_a is often used to indicate the reversibility of a hydrogen trap. At room temperature, a trap with -E_a larger than 50 kJ/mol is considered as 'irreversible' since there is a negligible probability of escape of a trapped hydrogen atom [28,155]. Irreversible traps act as sinks until they are saturated, whereas reversible traps can act either as sinks or sources of hydrogen. For example, if a dislocation (a mobile trap) passes a reversible trap that has a trapping strength lower than that of the dislocation, then the hydrogen in the reversible trap can be transferred to the dislocation and be carried along with the dislocation [155]. Hydrogen trapping/de-trapping is a thermally activated process, so a higher trap strength is needed to confine hydrogen at a higher temperature. This is an important consideration in certain application environments, such as in the components of a nuclear reactor [195].

Considering that hydrogen is highly mobile, equilibrium between the hydrogen in the lattice and in trapping sites can be reached rapidly in most circumstances [42,43]. The relationship between mobile and trapped hydrogen concentrations can be plotted against trap strength, as shown in Fig. 16 [196]. For a 10^{-2} wt ppm hydrogen in the BCC iron lattice (at the bottom of Fig. 16), the strong traps with 50 kJ/mol trapping energy have a >90% occupancy ($\theta_T > 0.9$); whereas weak traps with 10 kJ/mol are less than 10% full ($\theta_T = 0.1$), so that most of the hydrogen is in the lattice.

Finally, it is important to note that Fig. 15 depicts the classical hopping mechanism of atomic migration. Hydrogen is sufficiently light that quantum tunneling, and nuclear quantum effects can play a significant role in migration [191,197–200]. Recent computational work showed that quantum tunneling can result in a non-linear Arrhenius diffusivity of hydrogen in BCC iron up to the temperature range of 400–500 K, reveal that quantum effects play a crucial role in the process of H migration even at ambient temperatures [201,202]. Nuclear quantum effects were also demonstrated to influence hydrogen solubility, mobility, and trapping in the presence of strain [202,203]. It has been shown that nuclear quantum effects can increase the rate of trapping and decrease the rate of escape when hydrogen atoms interact with vacancies in BCC iron at low temperatures [204]. Similar findings were obtained in diamond [205–207], and it is likely that the consideration of quantum effects are essential for the behavior of hydrogen in other material systems. Quantum effects should be considered in the study of hydrogen behavior, especially in cases where the effects are most significant, such as in low temperature hydrogen trapping, high-pressure phase stability, mixed hydrogen isotopic composition, and hydrogen migration [208,209].

Overall, hydrogen behaves similarly to other interstitial elements in a metallic matrix, i.e., it segregates to any location where its location causes the energy to be lower [210,211], or where atoms are dragged by vacancies, dislocations, or other mobile defects. In fact, 'hydrogen trapping' highlights the uniquely high mobility of hydrogen compared to other interstitial solute atoms with larger atomic volumes and masses. Fig. 17 illustrates the wide array of microstructural features of
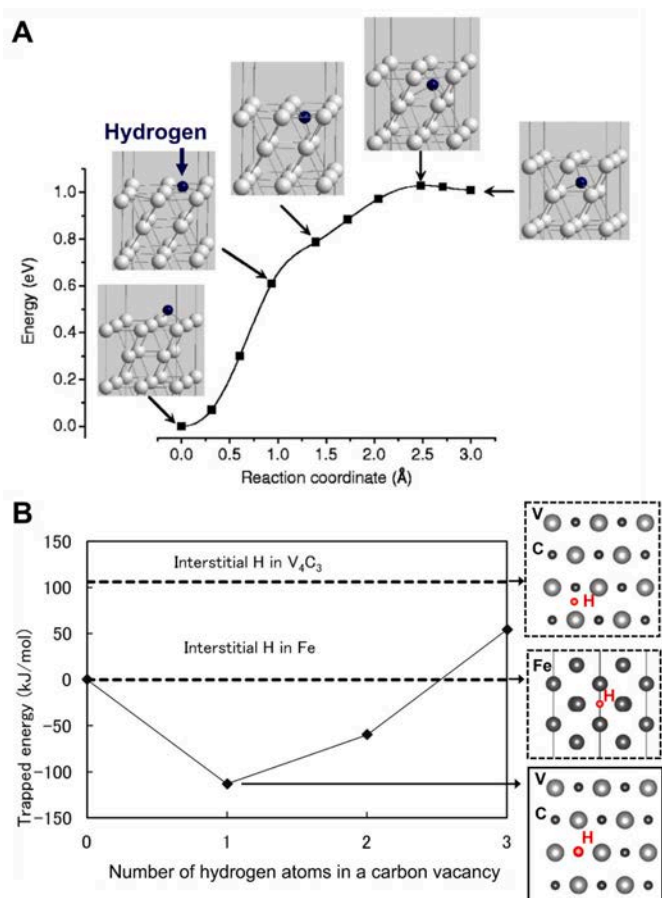
ARTICLE IN PRESS

Y.-S. Chen et al.   International Journal of Hydrogen Energy xxx (xxxx) xxx

Fig. 18. DFT calculation of hydrogen solute energy. (A) At the ferrite surface [166]. (B) At an interstitial site or a carbon vacancy of vanadium carbide (V$_4$C$_3$) [214].

Fig. 19. 2D slice of a MM/QM model to simulate a hydrogen atom. The small grey sphere in the inset is the hydrogen atom in a screw dislocation in an FCC lattice, where the color indicates the level of theory used to compute forces on those atoms: orange indicates quantum mechanics (typically DFT), purple indicates classical molecular mechanics potentials (e.g., embedded atom method, EAM), and blue indicates a buffer region where both approaches are used to avoid discontinuities. (For interpretation of the references to color in this figure legend, the reader is referred to the Web version of this article.)

engineering alloys that can act as hydrogen traps, for several length scales. Hydrogen trapping can take place at many feature types, including dislocations, vacancies, second phase interfaces, and gain boundaries [212].

3.2. Techniques for studying hydrogen trapping

This section introduces the computational and experimental techniques that are used for understanding hydrogen trapping. An overview of the techniques is followed by typical results for various common hydrogen traps. This establishes the foundation for the subsequent discussion about the roles of hydrogen traps in developing HE-resistant materials.

3.2.1. Atomic-scale modeling

The performance of atomic-scale simulations of hydrogen in metals requires consideration that hydrogen often displays complex chemical binding, especially with transition metals. Additionally, hydrogen is amphoteric and has charge states of -1 (hydride ion), 0 (atomic hydrogen) and $+1$ (proton). Thus, atomic-scale simulations of hydrogen require a level of theory capable of capturing these nuanced chemical interactions. For this reason, first-principle simulations using density functional theory (DFT) have been the main approach for understanding hydrogen tapping, as they rely on a quantum mechanical description of the electronic system. DFT simulations, either static or dynamic, provide both thermodynamic and kinetic information by determining the ground state energy of hydrogen in crystal lattices and at traps, and the activation energy for migration, dissociation, adsorption, and absorption. The example in Fig. 18A describes the energy for the absorption of
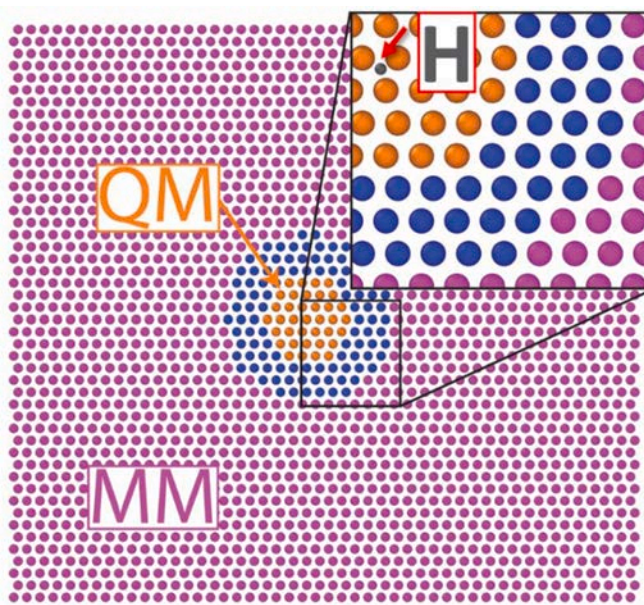
a hydrogen atom into the tetrahedral interstitial site of BCC iron from the (100) surface [213]. The other example in Fig. 18B compares trapping/solution energies of single and multiple hydrogen atoms in various positions in a ferrite matrix containing vanadium carbide (V$_4$C$_3$) [214], indicating that hydrogen is preferentially trapped in the carbon vacancy of V$_4$C$_3$ rather than the interstitial sites of both ferrite and V$_4$C$_3$. This result also shows that it is possible for a vacancy to accommodate up to two hydrogen atoms. This behavior is observed in many other materials. In some cases a single vacancy can accommodate up to 12 hydrogen atoms [215–220]. DFT is also used for studying the interaction of hydrogen atoms with alloying solute atoms [188,221,222], grain boundaries [223–225], and second phase precipitates [188,214, 226–233].

Recent DFT studies have shown that the ground state energy of hydrogen in an interstitial site is strongly dependent on the composition of its immediate surroundings and is relatively insensitive to crystal features and defects beyond the first shell of nearest neighbors [188,222, 231,234–237]. This insight is being used to develop a high throughput simulation method based on DFT simulations of the local environment, thus avoiding the computational burden of modeling a large simulation cell representative of the true alloy [188].

The significant computational cost of DFT limits the scale to a few hundred atoms. This size of model does not allow a full description of many of the microstructural features involved in HE mechanisms and hydrogen trapping. Even a simple dislocation requires over 1000 atoms for a full description of the core and local structure. Longer length scales requires use of classical molecular dynamics (MD) or tight-binding [238], which is an approximation of DFT with a tunable degree of assumptions and thus a sliding scale between DFT and classical MD. However, a recent study of Zr–H potentials showed that reliable Zr–H tight-binding simulations require a similar level of computational cost to DFT [239]. Also, there are few tight-binding codes available, and these are typically not as evolved or approachable as DFT codes. On the other hand, classical MD lacks the chemical accuracy and transferability of
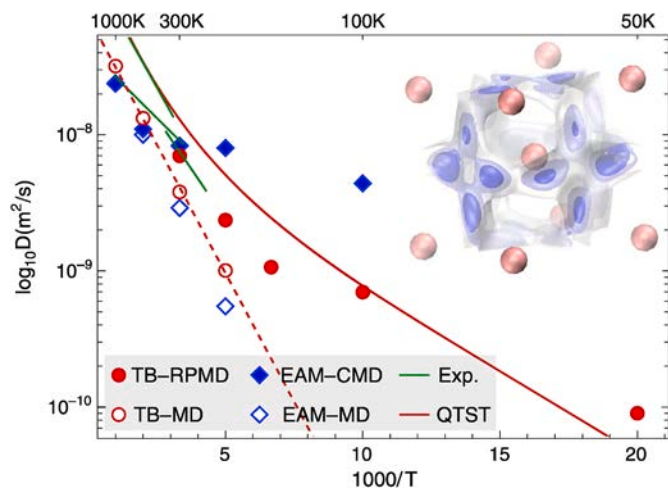
Fig. 20. Effect of including nuclear quantum effects (including tunneling) on the calculated diffusivity of hydrogen in BCC-Fe. Hollow points only consider classical mechanisms (classical molecular dynamics). Filled points include nuclear quantum effects through path integral methods. Red points use tight-binding to describe inter-atomic interaction from Ref. [203], blue points use classical potentials from Ref. [201]. The green line is experimental data from Refs. [159,258] and the red line is quantum transition state theory (which also accounts for quantum tunneling) from Ref. [207]. Inset is the density distribution of hydrogen (blue iso-surfaces) in the BCC-Fe lattice (red sphered). Reproduced from [203] (For interpretation of the references to color in this figure legend, the reader is referred to the Web version of this article.)
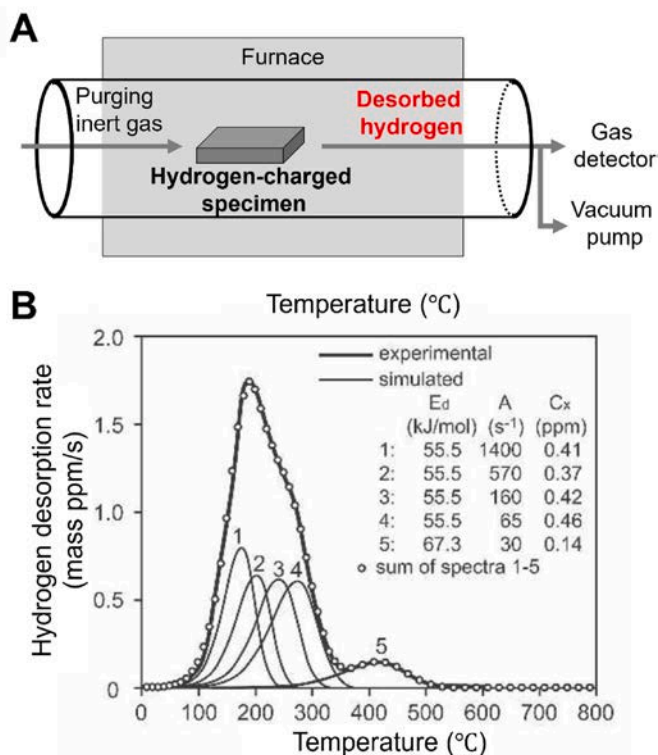

Fig. 21. Thermal desorption analysis for the study of hydrogen trapping. (A) Thermal desorption spectrometer setup with inert gas purging. (B) Example TDA data and peak deconvolution from a martensitic steel quenched from the austenite temperature (experimental and simulated datasets) [259].

DFT because it relies on a pre-defined description of inter-atomic forces. Some of the more complex and advanced interatomic potentials can describe multiple charge states of hydrogen [240,241], but these come at greater computational cost and have shown limited robustness and transferability. Recent developments of machine-learning potentials for MD also show good promise to facilitate HE research [242–244].

In contrast, the hybrid quantum mechanics-molecular mechanics (QM-MM) method is a promising development for larger-scale simulations of hydrogen in metals. This approach divides a simulation cell into two or three concentric regions. Fig. 19 shows an example in which an inner region centered around the hydrogen atoms uses DFT to describe the chemical interactions with quantum mechanical accuracy, while the outer region uses classical potentials to describe the long-range structure of the microstructural feature of interest. An intermediate "buffer" region where both DFT and classical potentials are used is often also added to provide convergence and eliminate artifacts of discontinuity between the two regions. QM-MM has proven successful for molecular and biological systems [245], but it has only recently started to be used for solid-state metallic systems, for example, in the investigation of the interaction between hydrogen and dislocation in BCC Fe [246]. More applications of this new method with the continuing increase of computational power can be expected in near future.

The methods above can be paired with other techniques when nuclear quantum effects are important. An example is path integral molecular dynamics (PIMD) [247,248], which has made progress in the last decade to make it approachable even at the DFT level of theory [208, 249–254]. In PIMD, instead of following one trajectory of motion dictated by Hook's and Newtown's laws, the simulation follows several imaginary trajectories and integrates between them to yield a probability of the hydrogen position and vector. These additional aspects indicate changes to the properties of hydrogen. Fig. 20 shows that the predicted diffusivity of hydrogen in BCC iron can be underestimated by several orders of magnitudes if nuclear quantum effects are not included [203], and this is supported by literature findings [201,202,255]. The same study found that approximately 30% of the hydrogen binding to a vacancy in BCC iron is due to finite temperature effects, and about half of that arises from nuclear quantum fluctuations [203]. In addition to PIMD, the Many-Interactive-World theory of Hall, Deckert, and Wiseman [256], recently implemented by Sturniolo [257], has received increasing attention in hydrogen modeling. This approach complements PIMD and describes the ground state rather than a dynamic state at a finite temperature. These approaches provide a path to include quantum effects in understanding hydrogen trapping.

3.2.2. Thermal desorption analysis

Experimentally, thermal desorption analysis (TDA) and hydrogen permeation tests are both used to measure hydrogen trapping. A TDA set-up is illustrated in Fig. 21A. A hydrogen-charged bulk specimen is placed in a programmable furnace that connects to a gas detector (either a gas chromatograph or a quadrupole mass spectrometer), a vacuum pump to evacuate the desorbed gas, and, in some cases, an inert purging gas (typically nitrogen or helium) to minimize artifacts from residual ambient gas in the chamber [184] and to avoid gas-surface reactions. Desorbed hydrogen is measured as the specimen is heated (Fig. 21B). Hydrogen desorption peaks at different temperatures are attributed to the desorption of hydrogen from various microstructural hydrogen traps. This is supported by knowledge of the specimen microstructure obtained by using advanced characterization techniques such as transmission electron microscopy (TEM) [259,260]. Hydrogen de-trapping is a thermally activated process, so the de-trapping energy of a peak associated with a specific hydrogen trap can be evaluated by repeating desorption experiments with different heating rates on the same material (but not the very same specimen since the heating can change the surface and microstructure of the specimen) [61]. TDA has also been used in isothermal mode to allow the measurement of hydrogen diffusion at various temperatures [261,262].
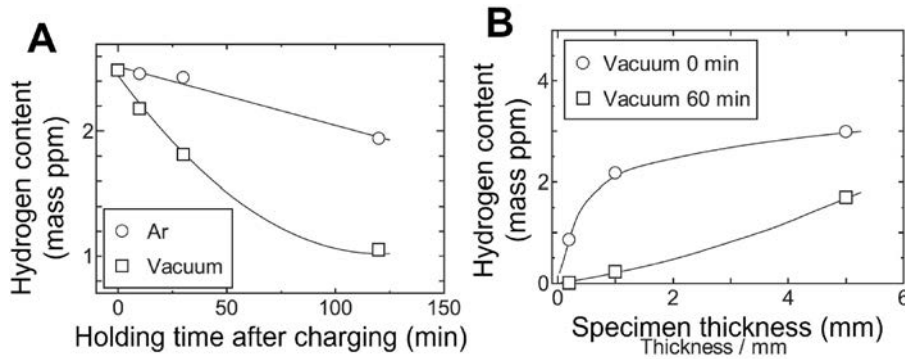
ARTICLE IN PRESS

Y.-S. Chen et al.   International Journal of Hydrogen Energy xxx (xxxx) xxx

Fig. 22. The influence of TDA experimental parameters. Hydrogen in iron samples as a function of (A) holding time after hydrogen charging in both argon and vacuum environments and (B) thickness after exposure to vacuum for two different durations [153].
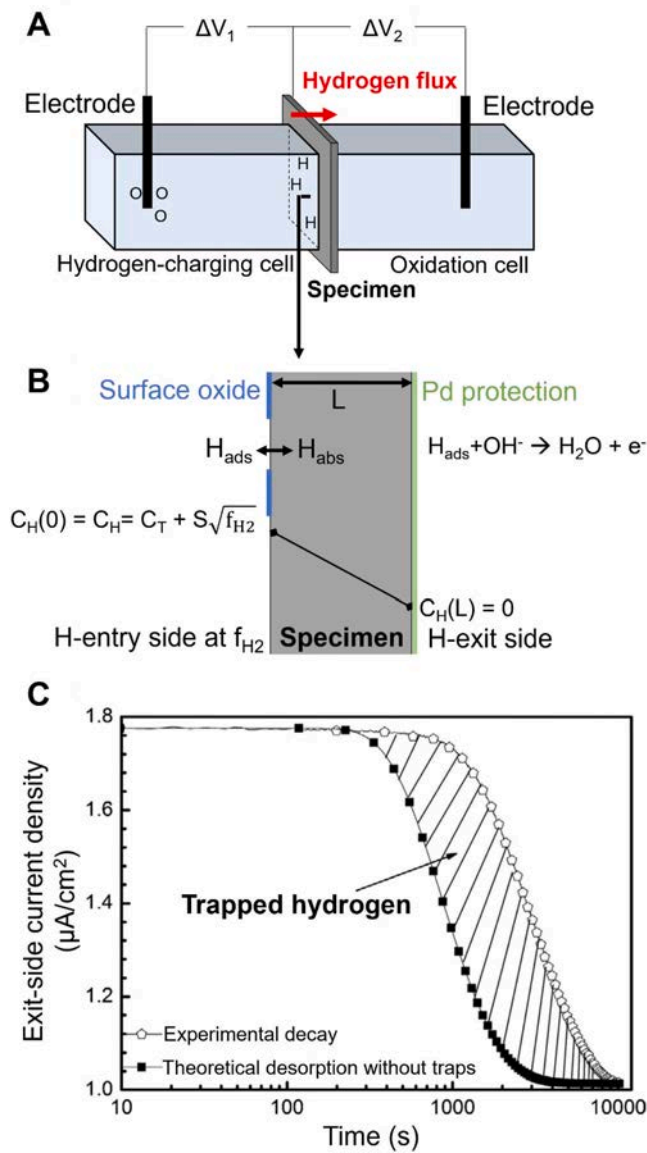

Fig. 23. Hydrogen permeation. (A) Schematic of the hydrogen permeation experiment. (B) Activities at the specimen surface. (C) Example hydrogen trapping measurement by a decay transient (from −1.2 V to −1.1 V). A 3.5NiCrMoV medium strength steel and 0.1 NaOH charging solution were used. (C) is reproduced from Ref. [265].
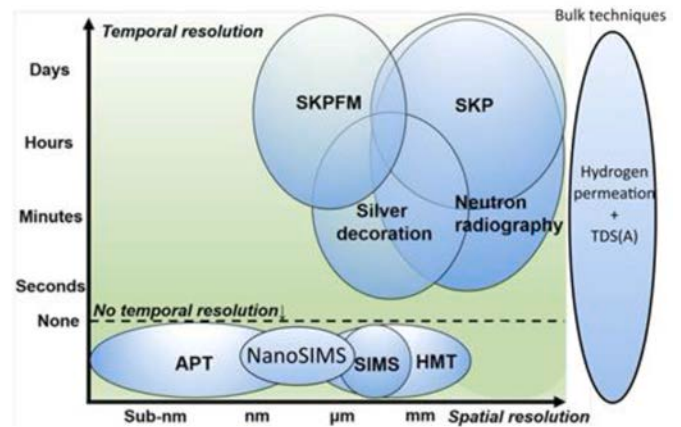

Fig. 24. Overview of spatial and temporal resolutions of common hydrogen mapping techniques. SKP(FM): scanning Kelvin probe (force microscopy). APT: atom probe tomography. SIMS: secondary ion mass spectroscopy. HMT: hydrogen microprint technique. TDS(A): thermal desorption spectroscopy (analysis). Reproduced from Ref. [86].

Additional insight about the link between specific microstructural features and hydrogen desorption peaks is possible by comparing the TDA of specimens that have different heat treatments or different compositions [177]. However, the assignment of peaks can be speculative [184] and it is common for a large peak to have contributions from multiple overlapping constituent peaks, (e.g., Fig. 21B), which then requires a deconvolution process to link the constituent peaks with individual microstructural features [204]. Contemporary hydrogen trapping research usually combines TDA data about the trapped hydrogen content and trapping energies with data obtained using complementary analytical techniques [73,160,204,179].

The time-to-test, the environment, and the specimen dimensions are the most significant variables for hydrogen quantification by TDA [153]. Fig. 22A shows that the amount of hydrogen loss from iron specimens over time (where hydrogen absorption is endothermic) is greater if the specimens were held in vacuum than in argon, Fig. 22B shows that smaller specimens retain less hydrogen, and that there is fast hydrogen loss in vacuum, consistent with findings in Ref. [263]. These issues explain some of inconsistency of hydrogen measurements between research groups and raise issues that need to be considered for quantitative hydrogen analyses on microscopic specimens where hydrogen egress is rapid, such as specimens prepared for microscopy experiments. Recent developments in low-temperature TDA (L-TDA, or cryogenic TDA as C-TDA) addresses some of the challenges in retaining hydrogen that desorbs at room temperature or below [181,182].
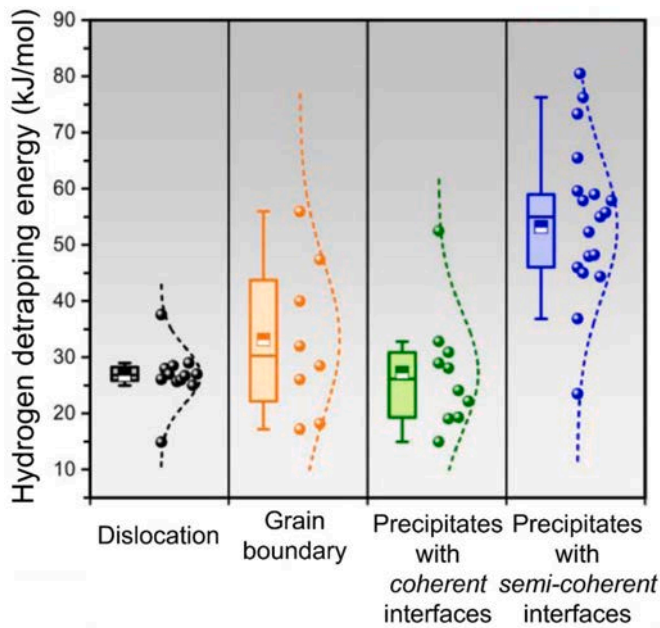
Fig. 25. Comparison of literature data for hydrogen trapping energies ($-E_b$) for common features in the BCC iron matrix. Reversibility of hydrogen trapping is defined as 50 kJ/mol. Reproduced from [229].

3.2.3. Hydrogen permeation

A hydrogen permeation setup and the steady-state hydrogen concentration profile through the specimen are illustrated in Fig. 23A and B [183]. The specimen is generally in the form of an approximately 1 mm thick sheet (L in Fig. 23B), and is the working electrode of both electrolytic cells in Fig. 23A. Hydrogen is generated at the specimen surface in the left-hand cell by cathodic hydrogen charging either at a constant potential (ΔV_1), as noted in the figure, or a constant current density. The applied potential generates a hydrogen fugacity that is designated as f_{H2} in Fig. 23B, which establishes an equilibrium hydrogen content (C_H) in the specimen that can be evaluated via Sieverts' law, i.e. Equation (9), and can be evaluated from the steady state hydrogen flux through the specimen. The hydrogen diffuses through the metallic specimen from the hydrogen-charging side to the exit side where the hydrogen flux is measured as a current as the hydrogen is oxidized in the oxidation cell by the application of a suitable potential (ΔV_2) to the working electrode. The technique is sensitive to small hydrogen fluxes through the specimen as it is possible to reliably measure a small current [156,177,264, 265].

A typical permeation experiment uses an inert gas such as nitrogen sparged into the hydrogen entry cell to prevent the evolution of surface gas bubbles that can affect the active area for the reaction. De-aeration of the solution in the oxidation cell is used to remove the current associated with the oxidation of dissolved oxygen in the solution. The exit surface of the specimen is typically coated with Pd (or Ni) to prevent oxidation. Generally, there is a surface oxide on any metal specimen (regardless of the specimen preparation method), and long-term precharging has been shown to be required for hydrogen charging of steels at moderate hydrogen fugacities to reduce the surface oxide to a stable condition and avoid irreproducible hydrogen permeation transients. The hydrogen concentration is linear across the specimen toward the exit side where $C_H = 0$ under steady state conditions.

Any alloy specimen has reversible hydrogen traps, as indicated in Fig. 13, and the decrease of the hydrogen charging potential (ΔV_1) decreases the entry-side hydrogen fugacity leading to a decay transient measured at the exit side. Fig. 23C shows how the hydrogen decay transient can be used to estimate the amount of reversibly trapped hydrogen by comparing it with the simulated data for a trap-free

Table 1
Trapping energies of common hydrogen traps in the BCC iron matrix.

Trap type	Binding energy ($-E_b$, kJ/mol)	Characterization technique	Reference
Solute elements			
Si, Cr, Mn, Co and Mo	Approx. 0	First Principle	[221]
C (interstitial)	9	First Principle	[221]
N (interstitial)	13	Magnetic Relaxation	[300]
Nb	−7[a]	First Principle	[221]
Ti	−8[a]	First Principle	[221]
Mg	−15[a]	First Principle	[221]
Sc	−20[a]	First Principle	[221]
Y	−25[a]	First Principle	[221]
Crystal defects			
Single vacancy	24–78	First Principle, Diffusion Analysis	[221, 301–304]
Micro-voids	40	TDA	[305]
Dislocations (bulk)	60	Diffusion Analysis	[306]
Screw dislocations	26	First Principle	[200]
Dislocation strain field	12–27	Diffusion Analysis, TDA	[190,307, 308]
Grain boundary	9–49	Mechanical Analysis, TDA	[308–311]
Prior austenite grain boundary	47	Permeation	[312]
Second phases			
Incoherent TiC	60–129	Permeation, TDA	[259,313, 314–316]
Semi-coherent TiC	48	TDA	[259]
Incoherent V_4C_3	40	TDA	[317]
Semi-coherent V_4C_3	25–28	TDA	[318,319]
Incoherent NbC	55–60	TDA	[320]
Semi-coherent NbC	28–56	TDA	[320,321]
Coherent Mo_2C	11–34	TDA	[322–324]
Cementite/α interface	11–18	Permeation, TDA	[308,325, 326]
ϵ carbide	12–65	Permeation, TDA	[327,328]
ϵ copper	27	TDA	[311]
Dispersed oxide	45	Permeation, First Principle	[329,330]
MnS interface	64	TDA	[305,307]
Austenite/Ferrite interface	44	Permeation	[331]
Iron oxide interface	43–62	TDA	[332]
Al_2O_3 interface	71	TDA	[333]

[a] Negative value means repulsive.

specimen. The trapping energy can also be obtained by adjusting the energetic factors such as temperature [265].

3.2.4. Microscopy techniques

In recent years, microscopy has been used to correlate hydrogen and microstructural features. Microscopic characterization of hydrogen is challenging for four reasons. First, hydrogen is mobile in metallic specimens and can desorb from the specimen rapidly. Second, microscopic specimens have generally small dimensions and total hydrogen egress is faster from a specimen with small dimensions (see Fig. 22B). Third, conventional electron microscopes typically cannot detect hydrogen, due to the low atomic mass of hydrogen and low interactivity with the incident electron beam [266–269]. For this reason, electron-based techniques are not generally useful for the characterization of hydrogen unless it is chemically bonded in stable phases. Fourth, residual hydrogen gas is present in the vacuum system of ion beam or electron microscopes [270–272], so the source of any detected hydrogen is uncertain [273,274]. The techniques available for the characterization of hydrogen trapping are summarized in a comprehensive review by Koyama et al. [86]. Here we introduce these techniques in three groups according to their mode of hydrogen detection.

Firstly, neutron beams can provide a contrast between hydrogen isotopes and other elements based on their distinct scattering cross-
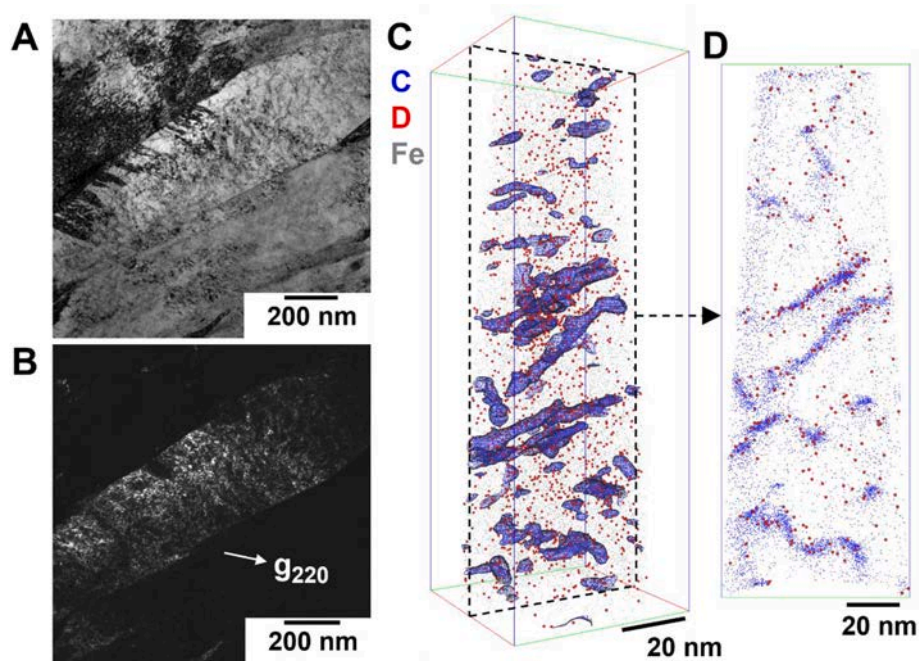
ARTICLE IN PRESS

Y.-S. Chen et al.
International Journal of Hydrogen Energy xxx (xxxx) xxx

Fig. 26. Dislocation hydrogen trapping in steel. (A) Bright-field image of dislocations in a martensitic steel, (B) dark-field image of (A). (C) 3-D APT map of carbon (blue), deuterium (red) as a marker for hydrogen, and iron (grey) with isoconcentration surfaces (blue surfaces) highlighting the location of dislocations represented by clustered carbon. (D) 2-D slice from the marked region in (A) showing the coincident locations of carbon (blue, i.e., dislocations) and deuterium (red). Reproduced from [87] (For interpretation of the references to color in this figure legend, the reader is referred to the Web version of this article.)

sections [275]. Neutron imaging can be used to map the distribution of hydrogen with sub-millimeter precision by comparing specimens with and without hydrogen [276,277]. Neutron imaging is non-destructive and can also provide reconstructed 3-D data.

Secondly, spatial distribution of hydrogen can be mapped by using spatially resolved mass spectroscopy techniques such as secondary ion mass spectroscopy (SIMS) [278] and atom probe tomography (APT) [29,86]. The methods utilize ion bombardment and field evaporation, respectively, to remove and detect atoms from the specimen, including hydrogen, allowing the creation of atom maps at the micro- and nano-scale. Both techniques are sensitive to light elements, but the analysis of hydrogen is complicated by the presence of hydrogen as a residual gas in their vacuum chambers. Uncertainty over the origin of the hydrogen detected can be circumvented by using deuterium (^{2}H or D), the second most abundant hydrogen isotope. Deuterium has a larger atomic mass that is easily differentiated from the primary isotope of hydrogen (protium, ^{1}H) by mass spectrometers, and can be used during charging (if charging with hydrogen is a part of the experiment) [87,194,231,278–285]. The different masses and hence slightly different diffusivities of ^{1}H and ^{2}H [255] do not normally significantly influence the distribution of hydrogen within samples at ambient conditions [286]. Hydrogen loss is a particular problem because of the small specimen size for SIMS and APT [285]. For APT, hydrogen loss has been mitigated using cryogenic sample transfer to inhibit hydrogen desorption, which led to cryo-APT [87,194,280,281,283,284,287–289]. Cryogenic transfer/analysis for SIMS is also possible and has been demonstrated for a ferritic steel [290], but is not yet available for the NanoSIMS. Even without cryogenic capabilities, NanoSIMS has been successfully used to analyze hydrogen charged samples for a range of metallographic systems [231,282,291–293].

Thirdly, hydrogen trapping can also be characterized by decorating the sample with a chemical or physical agent that can interact with the hydrogen and can represent the location of hydrogen. The techniques using silver decoration and an integrated microscope with good spatial resolution was designated. The silver ions on the surface of a hydrogen-charged specimen are reduced by the hydrogen that is desorbed from the

specimen bulk according to the following reaction:

$$Ag^+ + H_{ads} \rightarrow Ag + H^+ \tag{12}$$

The Ag^+ ion can be deposited on the surface using an Ag-containing chemical such as AgBr. The reduced metallic Ag atoms reveal the hydrogen-rich regions. The hydrogen microprint technique (HMT) operates similarly to the silver decoration method, relying on the reduction and deposition of silver atoms [294–296]. The main distinction lies in the use of an $Ag(CN)_2$ aqueous solution, immersing the specimen surface for silver decoration, in contrast to the approach using an AgBr emulsion. Another similar method decorates the sample surface with hydride-forming materials such as palladium to induce a localized change in conductivity, which can be measured using a scanning Kelvin probe (SKP) which detects hydrogen at the sample surface. The technique in combination with high-resolution scanning probe microscope is called scanning Kelvin probe force microscopy (SKPFM) [297–299]. These techniques require a surface that is oxide-free prior to the application of the hydrogen-sensitive decoration. The temporal and spatial resolutions of these techniques were summarized by Koyama et al. as shown in Fig. 24 [86].

3.3. Characterization of hydrogen trapping

The different microstructural features that act as hydrogen traps were illustrated in Fig. 17. Fig. 25 and Table 1 illustrate the hydrogen trapping energies of common traps (-E_b) in a BCC iron matrix. The scatter is attributed to both the trap structure and measurement details [184]. Fig. 25 indicates that lattice defects (dislocations and GBs) and precipitates with coherent interfaces have a median trapping energy less than 50 kJ/mol (often defined as the reversibility limit); whereas less coherent precipitates have higher hydrogen trapping energies. Many early studies (particularly those before 1990 [279,280]) did not consider the contribution of the substructures of the trapping features, e.g. vacancies in carbides. It may now be prudent to revisit the trapping properties of some of these trap types now that better techniques are available to measure the hydrogen within different phases and at
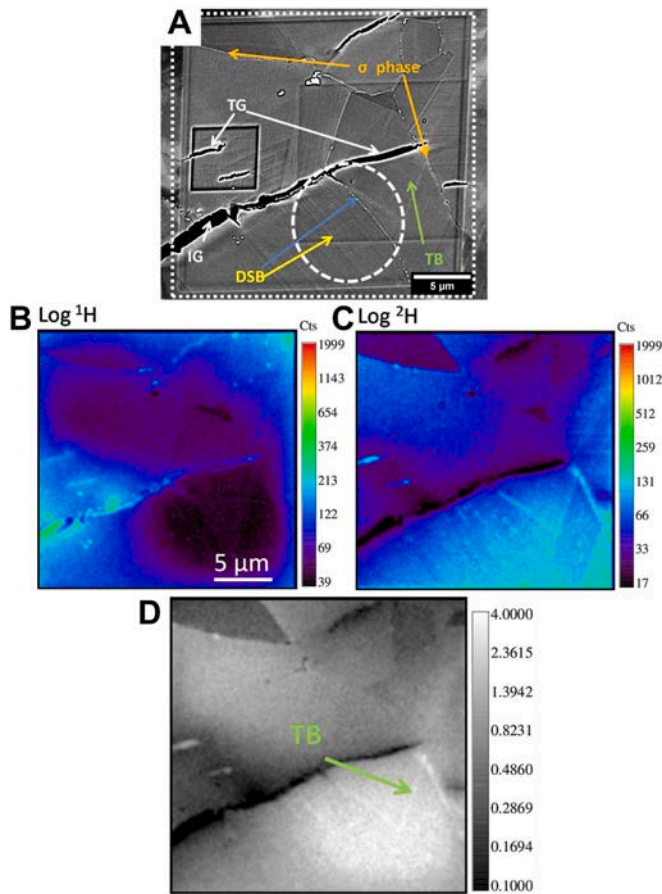
Fig. 27. NanoSIMS evidence of twin boundary hydrogen trapping in a nickel-based alloy. (A) Secondary electron image of a region of interest (ROI) at the proximity of a crack in a deuterium-embrittled alloy 625+ sample. The ROI contains the secondary σ phase, dislocation slip band (DSB), transgranular and intergranular cracks (TG and IG, respectively), and deformation twin boundary (TB). (B) and (C) are the logarithmic secondary ion intensity maps of protium (^{1}H) and deuterium (^{2}H), respectively. (D) is the ratio of the logarithmic ^{2}H to logarithmic ^{1}H ratio map which shows the concentration of deuterium at TB (green arrowed region). Reproduced from [282] (For interpretation of the references to color in this figure legend, the reader is referred to the Web version of this article.)

different microstructural features.

3.3.1. Solute elements

Hydrogen trapping at a solute element in a metal matrix is generally insignificant compared to other microstructural traps. Counts et al. used first-principle techniques to study the interaction energies of various solutes with hydrogen in a BCC iron matrix [221]. The interstitial carbon solute atom was found to prefer to occupy the octahedral site, unlike hydrogen which prefers the tetrahedral site [186]. The interaction between the two atoms, 9 kJ/mol as noted in Tables 1 and is insignificant compared to the diffusion energy in the BCC matrix (4.5–5.5 kJ/mol as per [190]). The substitutional solute atoms were found to be either inert or repulsive to nearby hydrogen atoms (Table 1), and the presence of these elements does not significantly influence the interaction between a hydrogen atom and a vacancy, meaning that the hydrogen trapping at the atomic scale is dominated by the vacancy itself, regardless of the presence of solute elements. These findings were supported by later research [334].
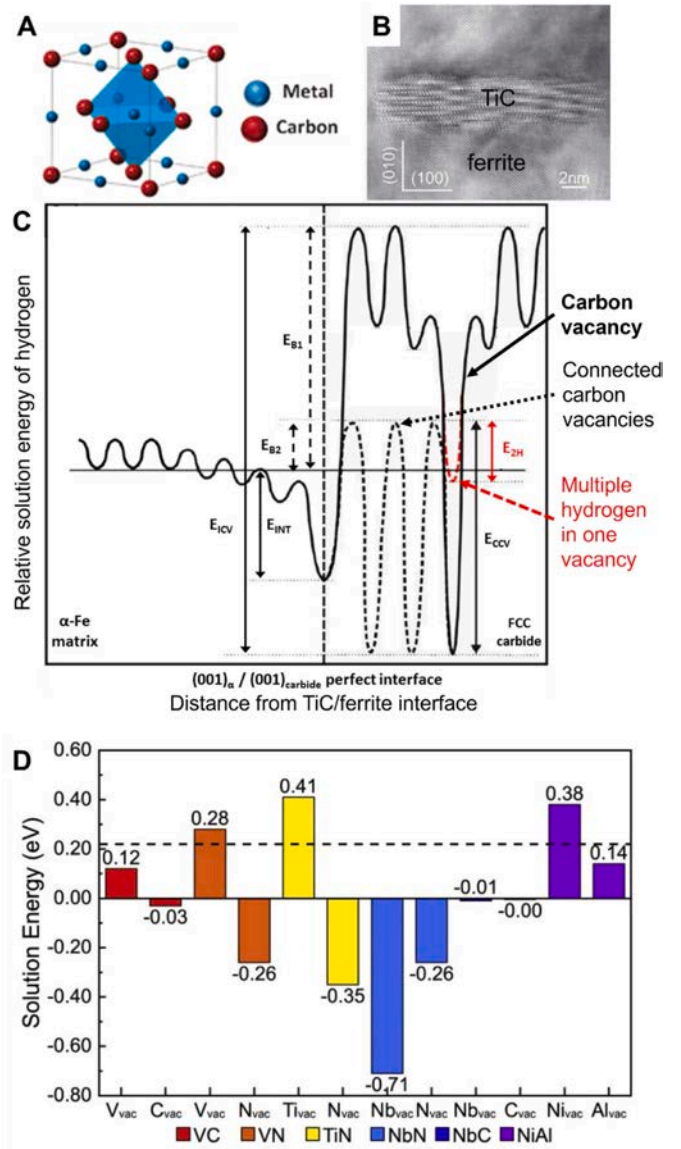

Fig. 28. Density function theory (DFT) calculations for hydrogen trapping in TiC. (A) Schematic of the FCC carbide structure. (B) Typical TEM image of TiC in ferrite [259]. (C) Solution energy of hydrogen around a TiC precipitate with different configurations [361]. (D) Solution energy of hydrogen in metal and non-metal vacancies for common FCC precipitates [230]. It is important to note that the hydrogen potential differs between (C) and (D) and, as such, cannot be directly compared.

3.3.2. Crystal defects

3.3.2.1. Hydrogen-enhanced strain-induced vacancies. Part 3.3.2 describes hydrogen-enhanced strain-induced vacancies as a mechanism for embrittlement. Hydrogen stabilizes vacancies in many metals and alloys [32,47,121,129,218,221,335–340]. Nagumo and Takai [47] reviewed this phenomenon and described how hydrogen-enhanced vacancy formation and subsequent vacancy clustering can lead to the formation of microvoids, which then coalescence, leading to hydrogen-induced crack propagation by ductile micro-void coalescence. An extremely high hydrogen charging fugacity (GPa level) can lead to the formation of stable hydrogen-vacancy clusters in an abnormally high concentration (up to 30 atomic percent), referred to as 'superabundant vacancies' by Fukai [341].

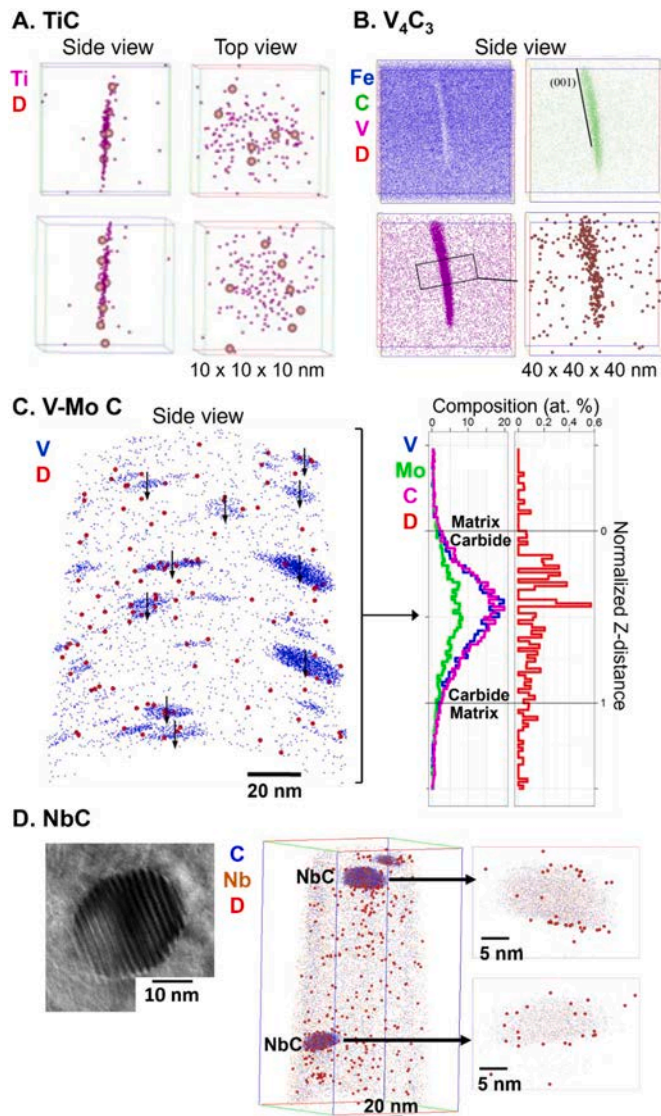Hydrogen can also be trapped by dislocations, similar to the Cottrell

Fig. 29. APT characterization of hydrogen trapping by face-centered cubic/rocksalt-structure carbides. (A) Hydrogen (deuterium) in TiC [281]. (B) Result for V_4C_3 [194]. (C) Result for V–Mo carbide from Ref. [192]. (D) Result for NbC from Ref. [87].

atmosphere formed by other interstitial solute atoms such as carbon in steel [121,129,130]. Hydrogen trapping at dislocations in an untempered martensitic steel specimen was directly observed by Chen et al. using cryo-APT [87]. Fig. 26A and B are bright- and dark-field TEM images of the dislocation-dense martensitic structure. The APT reconstruction in Fig. 26C contains carbon isosurfaces that mark the position of dislocations. Fig. 26D shows the colocalization of atoms of carbon (blue) and deuterium (red) at the dislocations, providing evidence supporting the HELP model [30,31]. The opposite effect - hydrogen-*reduced* dislocation mobility was found by Xie et al. [342] in an aluminum alloy using TEM with in-situ mechanical loading in a hydrogen-containing environment. The authors suggested that this could be caused by an additional interplay with vacancies. Hydrogen enhanced mobility occurs for both edge and screw dislocations [343]. Calculations indicate that the dislocation core interacts with hydrogen more strongly than the elastic field of the dislocation and that the increase in core radii and decrease in core energy leads to the reduction of dislocation line energy by H [344].

In addition to acting as a hydrogen trap, a mobile dislocation can also drag hydrogen. Hydrogen transport by dislocations can dominate

hydrogen re-distribution [345–347]. NanoSIMS analysis of a 625 Ni alloy showed deuterium enrichment at dislocation slip bands after a crack growth test with in-situ charging. However, when the alloy was charged but not strained, there was no deuterium localization, indicating deuterium transport by mobile dislocations [282]. Dislocation movement induced by hydrogen diffusion has also been recently recorded [348].

Since GBs interfere with dislocation glide, hydrogen transport by dislocations can lead to hydrogen accumulation at GBs, which may promote hydrogen-induced decohesion and subsequent intergranular fracture [349,350]. This relationship between strain and hydrogen distribution may also explain the strain rate dependence of HE, as discussed in Section 2.1.4. A high strain rate results in high-speed dislocations that cannot transport hydrogen, reducing hydrogen drag and causing less embrittlement. A low strain rate produces slower-moving dislocations that transport hydrogen, contributing to HE.

Grain boundaries can also trap hydrogen, which has been observed by APT [87]. Compared to vacancies and dislocations, hydrogen behavior is more complex at GBs, and depends on the crystal structure of the host matrix and the geometric structure of the GB. In BCC metals, GBs generally act as trapping sites since the hydrogen diffusivity at GBs is lower than the lattice diffusivity. In BCC iron, hydrogen generally reduces the GB cohesion, which leads to fracture at a sufficiently high hydrogen concentration [262]. Prior-austenite GBs are particularly susceptible [123]. In FCC metals, where lattice diffusion of hydrogen is slower, GBs can act as hydrogen traps and offer a rapid diffusion path for hydrogen, depending on the relative diffusivity in the FCC lattice and along the particular GBs [351]. In austenitic steel, $\Sigma5$ and $\Sigma9$ GBs trap hydrogen, but not $\Sigma3$ GBs [352]. HE in FCC nickel alloys generally leads to intergranular fracture. The effect of hydrogen on grain boundary behavior remains difficult to predict. The exact interplay of GBs with hydrogen is a topic deserving of more emphasis in future research [113, 353].

Twin boundaries (TB) are more prevalent in FCC metals such as nickel. Using SKPFM and TDA, Koyama et al. concluded that TB trapping is only slightly stronger than other reversible traps such as dislocations [33,354]. Aboura et al. used NanoSIMS to identify deuterium localization at twin boundaries in a deuterium-embrittled nickel alloy [282]. Fig. 27A is a secondary electron image from this study that contains a region with a deformation-induced twin boundary (TB, green arrow). Protium (^1H, the reference hydrogen background in this experiment), and deuterium (^2H, real signal) were mapped, as shown in Fig. 27B and C, respectively. The ratio between the logarithmic concentrations of ^2H and the logarithmic concentration of ^1H from Fig. 27B and C, respectively, then led to Fig. 27D which shows a bright line (high ^2H intensity) along the identified TB, showing deuterium trapped at the TB. Although trapping at TB has been observed, the exact role of TB for bulk HE, i.e., whether hydrogen at TB facilitates or mitigates HE, is still a topic of discussion [33,354].

3.3.3. Precipitates and second phases

Precipitates and second phase particles in a solid solution matrix can act as benign hydrogen traps and can significantly increase HE resistance by reducing the available hydrogen [17,28,49,289,355]. In ferritic steels, fine precipitates of the carbides of transition metals, e.g., Ti, V, Nb, and Mo, can be produced with a high number density, with tunable hydrogen trap strengths, which are thought to be controlled by their interface coherencies [356–360].

DFT has been used to investigate the hydrogen trapping mechanism of carbides with a rock-salt (NaCl) structure (Fig. 28A), such as TiC (TEM image in Fig. 28B), V_4C_3, and NbC [214,361]. Fig. 28C shows the calculated hydrogen solution energy around the interface between a TiC particle (right-hand side) in ferrite (left-hand side) [361]. The authors found that i) the interface of the TiC particle is an effective trap; ii) a carbon vacancy inside the TiC bulk is the strongest trap, however it is difficult for hydrogen to reach this trap because of the high energy
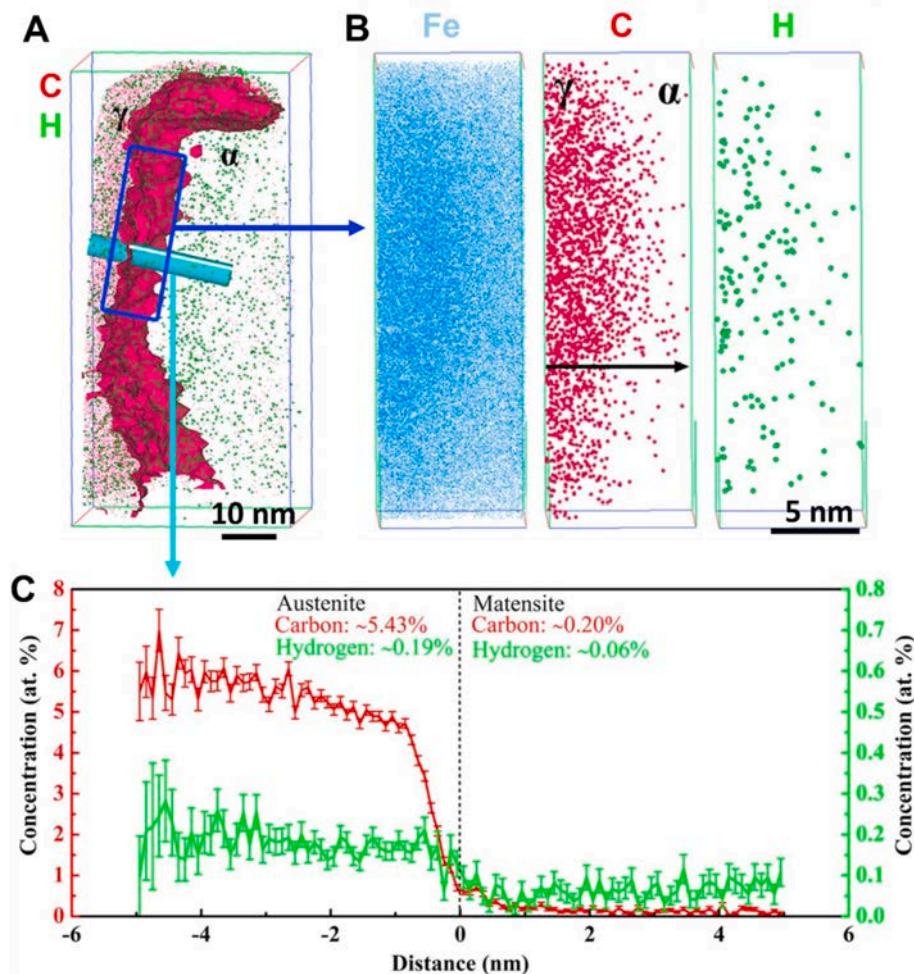
Fig. 30. Hydrogen trapping in retained austenite in ferrite. (A) 3-D APT map with austenite-ferrite interface highlighted by a carbon isoconcentration surface. (B) Atom maps of iron, carbon, and hydrogen (^{1}H, not deuterium) from the highlighted region in (A). (C) Atomic concentration across the interface from cylindrical the region highlighted in (A) [351].

barrier; iii) this energy barrier can be lowered in the presence of a high number of carbon vacancies that form a channel for hydrogen penetration into the TiC bulk (black broken line); and iv) the presence of extra hydrogen atoms in a trap can significantly reduce the de-trapping energy and facilitate the penetration of hydrogen, which is likely the case for high-fugacity/electrolytic hydrogen charging (red broken line). Fig. 28D shows the trapping energies of a range of metal and non-metal vacancies in common FCC precipitates evaluated using DFT [230]. This calculation suggests that carbon vacancies are stronger hydrogen traps than metal vacancies.

APTq has been used to study hydrogen trapping at fine FCC carbide precipitates [194,280,281,283,284]. Takahashi and co-workers pioneered the use of gaseous hydrogen charging and cryo-APT to study hydrogen trapping at TiC and V_4C_3 as shown in Fig. 29A and B, respectively, confirming that these carbides act as hydrogen traps in steels [194,281]. Later, Chen et al. [192] used cryoAPT to investigate the hydrogen trapping mechanism of a deuterium-charged V–Mo-mixed carbide. They concluded that hydrogen was located within the precipitates using a statistical approach to normalize and superimpose the concentration profiles across all of the measured particles, as shown in Fig. 29C.

The V–Mo carbides studied by Chen et al. had more carbon vacancies than those studied by Takahashi et al. due to the presence of molybdenum as a substitutional metal element at vanadium sites [234]. Chen et al.'s finding of interior trapping of hydrogen in

carbon-vacancy-containing carbide was consistent with Di Stefano et al.'s numerical prediction about hydrogen penetration in the presence of abundant carbon vacancies and charged hydrogen [361]. More recently, Chen et al. used the same protocol to investigate hydrogen trapping in a well-annealed, spherical, incoherent NbC, which should have few carbon vacancies. Fig. 29D shows that hydrogen was trapped at the NbC/ferrite interface, consistent with the computational prediction that the interface acts as a hydrogen trap [229]. Similarly, SKPFM studies showed trapping at the interface for large, incoherent TiC particles in a ferritic matrix [362]. Hydrogen trapping in this type of FCC carbide is therefore related to both the interface and the presence of defects within the precipitate.

In addition to transition metal carbides, cementite and epsilon (ε) carbide in steels also act as hydrogen traps as demonstrated in Refs. [279,363–365], respectively. These carbides are believed to primarily trap hydrogen in the carbon vacancies at the interface, although high-resolution observations are required for verification.

Apart from carbides, metallic particles (such as copper) have also been identified as hydrogen traps [311,366–368], although the exact trapping sites for these particles has not been demonstrated. In oxide dispersion strengthened (ODS) steels, simulations suggest that hydrogen trapping occurs through oxygen-vacancy pairs at the interface of oxide particles [369]. Some sulfide inclusions such as MnS can in theory also trap hydrogen strongly, and such inclusions are known to cause local HEDE at their incoherent interfaces where the hydrogen concentration
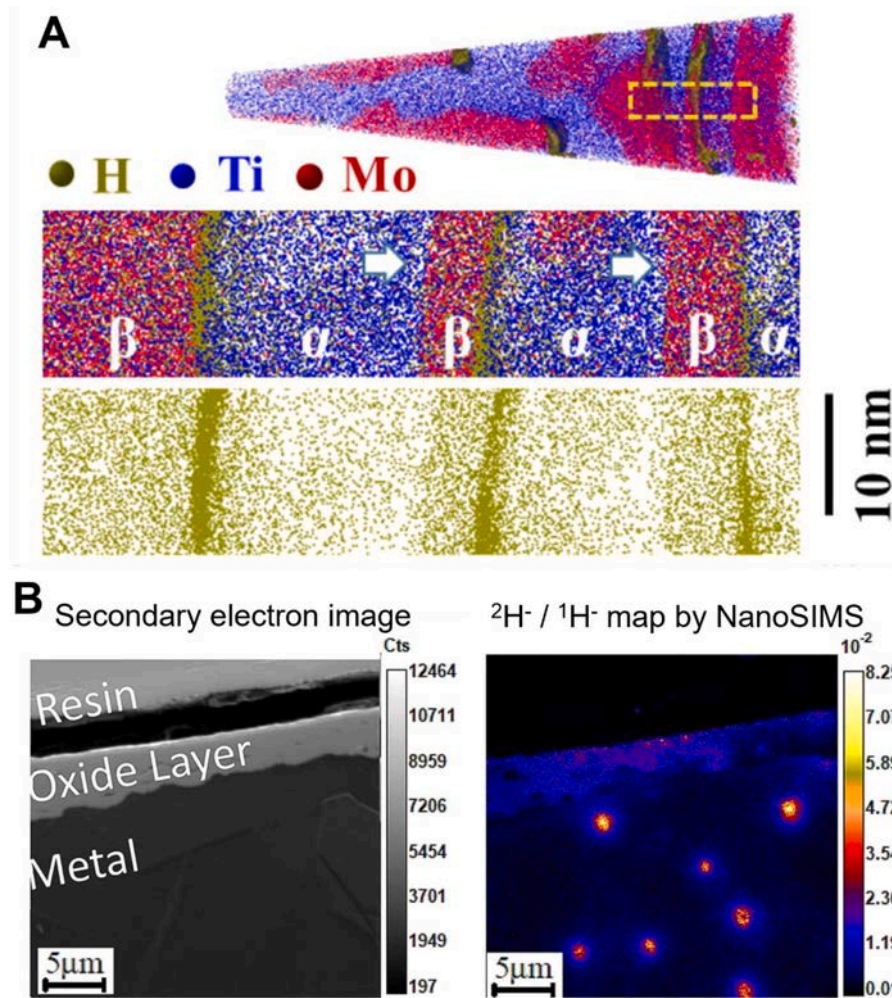
Fig. 31. Second phase hydrogen trapping in titanium and zirconium alloys. (A) APT atom maps of the primary α-Ti phase (blue), secondary β-Ti-Mo phase (red), and hydrogen (dark yellow) [388]. (B) NanoSIMS mapping of hydrogen trapping in Zr–Fe/Cr phases in zirconium alloys [231] (For interpretation of the references to color in this figure legend, the reader is referred to the Web version of this article.)

leads to fracture initiation [370,371–375].

Retained austenite, an FCC phase in the BCC iron matrix, is also an important hydrogen trap. Hydrogen has a much lower diffusivity and a much higher solubility in austenite than in ferrite or martensite [376–382]. APT visualizations of hydrogen in retained austenite are shown in Fig. 30 [377]. In some advanced high-strength steels, retained austenite in the microstructure can undergo an austenite-to-martensite phase transformation during deformation. This transformation-induced plasticity (TRIP) can significantly increase ductility [383]. However, this transformation releases any hydrogen dissolved in the austenite (as the austenite transforms) into the freshly formed martensite, which can be severely embrittled by the hydrogen [28,378,380,384]. Therefore, the use of austenitic phases as hydrogen traps requires caution that any subsequent loading or thermal environment does not lead to detrimental hydrogen release [385,386].

In hydride-forming metals such as titanium and zirconium, some second phase particles have also been found to trap hydrogen [232, 387–389]. APT observations of a Ti–Mo alloy, Fig. 31A, revealed that hydrogen can be trapped at the interface of the Mo-rich second phase [388]. NanoSIMS observations have also shown the hydrogen trapping at the Fe- and Cr-rich phases in a Zr–Fe–Cr alloy, Fig. 31B [231]. These hydrogen traps can play an essential role in the redistribution of hydrogen upon thermal cycling in the nuclear applications in which these Zr alloys are used, which can cause precipitation and re-orientation of hydrides and can lead to delayed hydride cracking

[98].

4. Microstructural engineering of hydrogen traps for embrittlement mitigation

For a closed system with a finite amount of hydrogen (i.e., IHE), the addition of microstructural hydrogen traps is expected to be effective for HE mitigation [28]. Where hydrogen supply is infinite (i.e., EHE), traps are not generally thought to be viable strategy for mitigation, as the traps saturate in an open system with a permanent source of hydrogen [390], however modeling has suggested that trapping can reduce the critical hydrogen concentration in open systems under cyclic loading [196]. In this section, we review the role of hydrogen traps for the mitigation of HE.

Exploiting trapping behavior in the design of embrittlement-resistant alloys requires a better understanding of the relationship between microstructural hydrogen trapping and macroscopic HE mitigation. First, we reiterate the key considerations proposed by Pressouyre [28, 155,391] to define whether a trap is 'good' or 'bad' for reducing HE susceptibility in a particular application.

1. What is the form and the possible amount of the hydrogen supply? i. e., is hydrogen supply internal or environmental, continuous or intermittent, infinite or finite?
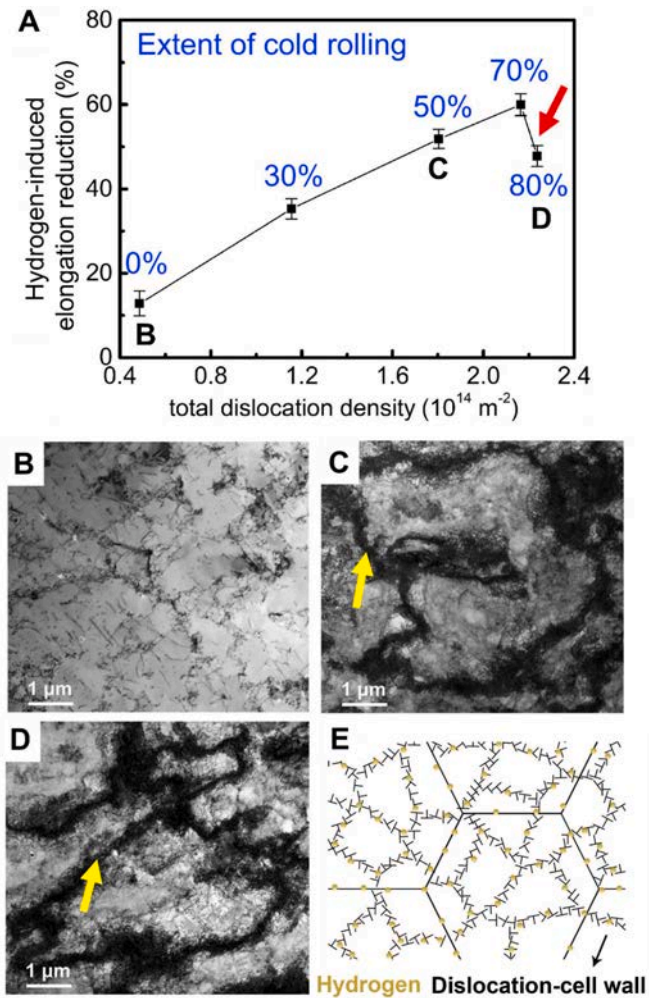
ARTICLE IN PRESS

Y.-S. Chen et al.   International Journal of Hydrogen Energy xxx (xxxx) xxx

Fig. 32. Effect of dislocation cells on internal hydrogen embrittlement (IHE) susceptibility. (A) IHE susceptibility (defined by elongation loss) as a function of dislocation density, relating to the extent of cold work. TEM micrographs of dislocation structures in (B) undeformed, (C) 50%-deformed, and (D) 80%-deformed specimens. (E) Schematic illustration of the dislocation cells trapping hydrogen to increase the HE resistance. Reproduced from [408].

2. Is the material subjected to elastic or plastic deformation in the presence of hydrogen? i.e., what is the interplay of dislocations and plasticity with hydrogen?
3. What microstructural sites are most susceptible to HE? i.e., does the HE-induced fracture occur transgranularly, intergranularly or at a second phase interface?
4. What is the strength of the benign hydrogen traps in a material compared to that of the HE-susceptible features at the temperature of service? i.e., do the benign traps compete with the features that also attract hydrogen, but contribute to HE, such as dislocations or MnS interfaces? Are the traps reversible?

4.1. Grain boundaries and dislocations

A finer grain size and a lower dislocation density increase EHE resistance (Fig. 8) [91]. Grain refinement is effective in a range of alloy systems including ferritic steels [392,393], martensitic steels (prior-austenite grain size) [123,394], austenitic steels [395–400], nickel [401], and FCC high-entropy alloys [402,403]. The benefit is attributed to increased hydrogen trapping due to more GB areas and, for the case where hydrogen supply is finite, less hydrogen per unit GB area [404]. A
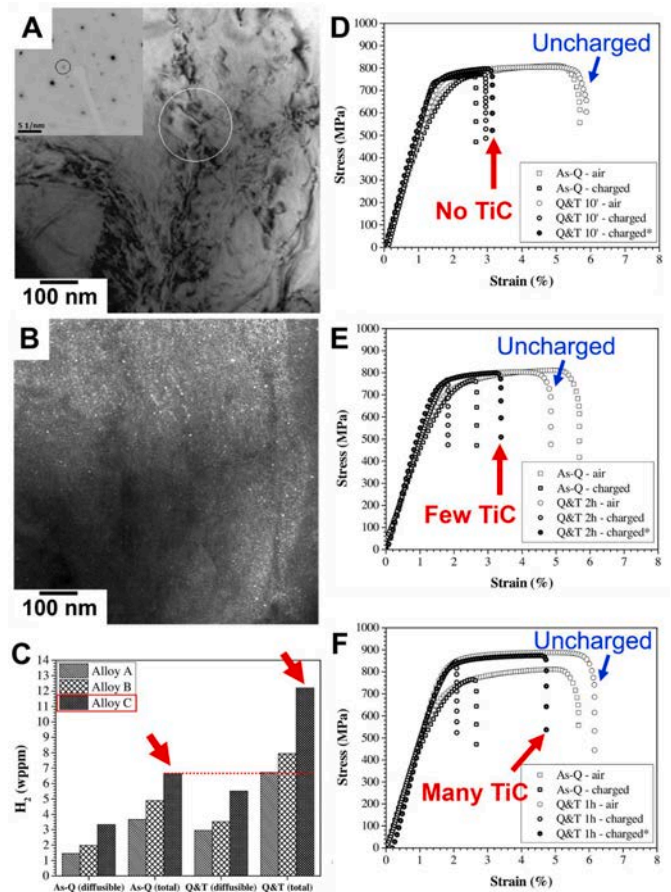

Fig. 33. Efficacy of TiC for internal hydrogen embrittlement (IHE) resistance. (A) Bright-field TEM micrograph of a specimen with high density of TiC (Alloy C charged for 1 h, corresponding to the data shown in (F)). (B) Dark-field TEM micrograph of (A) from the second-phase diffraction spot indicated inset in (A). The bright spots are TiC precipitates. (C) Saturated hydrogen content in various tested materials showing the greater capacity for H in the sample with precipitates (Alloy C, Q&T). (D), (E), and (F) highlight the tensile properties of uncharged specimens (blue arrows) and the specimens charged with 7% hydrogen (red arrows) from the materials containing negligible, low, and high numbers, of TiC. Reproduced and adapted from [416] (For interpretation of the references to color in this figure legend, the reader is referred to the Web version of this article.)

graded grain structure with fine-grains at the surface can also provide better HE resistance than a homogeneous grain structure [405], while retaining a high strength-ductility combination [406].

Dislocations are generally considered to be traps that are unfavorable for HE mitigation [407]. In an exception, it was recently reported that for severe deformation of pure iron by cold work, above a certain dislocation density, the HE drops slightly due to the trapping effect of dislocation cell walls [408]. Fig. 32A shows that HE increased as cold work increased from 0% to 70% and decreased thereafter (red arrow). TEM revealed that the 80% cold work specimen has a substructure of dislocation cells, as shown in Fig. 32D. The authors attribute this decrease of HE susceptibility an effect similar to grain refinement, i.e., increasing the density of trapping sites and limiting the availability of hydrogen within the dislocation cells, as illustrated in Fig. 32E.

It has also been possible to fabricate alloys with desired GB orientations to mitigate GB fracture, an approach known as 'grain boundary engineering' [409,410]. The efficacy of GB engineering for reducing HE susceptibility in FCC alloys was demonstrated by Bechtle et al. [124]. Lower HE susceptibility was measured in the Ni alloy specimens with more low-energy boundaries (such as twin boundaries). Similar results
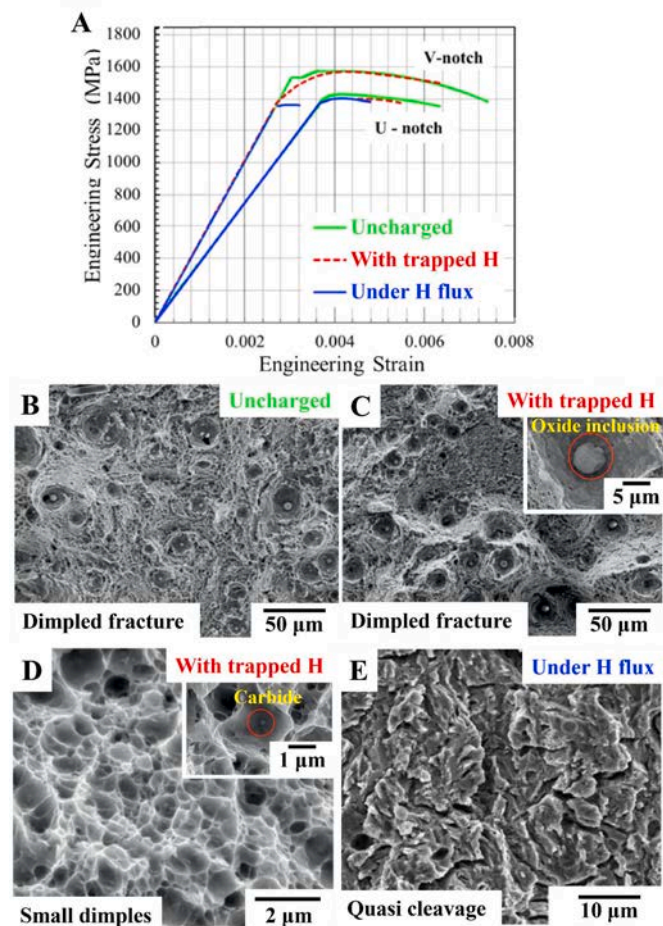
Fig. 34. The role of trapped and diffusible hydrogen in HE. (A) SSRT results from a Fe-0.3C-0.4Si-0.5Mn-1.0Cr-0.8Mo-0.05V-0.04Nb (wt. %) martensitic steel with small amounts (less than 0.04 wt%) of Al, S, Cu, Co and Ca, which is austenitized, quenched, and tempered at 710 °C for 30 min. Both V- and U-shaped notches were used in plate tensile samples. The ductility decreased in the following order: specimen without hydrogen (green curves), specimens with trapped hydrogen (red curves), and specimens with diffusible and trapped hydrogen (blue curves). SEM fracture surface observations of (B) uncharged specimen with dimpled features, (C) specimen with trapped hydrogen, also with dimpled features showing oxide inclusions at the centers of the dimples, (D) the specimen with trapped hydrogen showing additional carbide inclusions at the centers of the dimples. (E) Quasi-cleavage for specimens with both trapped and mobile hydrogen. Note the scale difference among the micrographs. Reproduced from [370] (For interpretation of the references to color in this figure legend, the reader is referred to the Web version of this article.)

were later measured for other FCC alloy systems [411–414]. The concept is that a higher density of 'special' GBs that have higher coherency with adjacent grains (i.e., Σ number ≤29, such as Σ3, Σ5, etc.) lead to a lower tendency to trap hydrogen atoms. This GB engineering approach has only been demonstrated for FCC alloys, which are more susceptible to hydrogen-induced intergranular failure than BCC alloys.

The interaction of hydrogen and other species segregated at GBs is still largely unknown, particularly the effects on hydrogen trapping and HE [211]. Segregation also varies from boundary to boundary and depends on the boundary structure. Correlative TEM-APT [415] allows measurement of both structure and elemental segregation at GBs. Future studies may also use NanoSIMS, cryo-APT and/or mechanical testing to enable a better understanding of the relationship between elemental segregation, hydrogen trapping and HE.

4.2. Hydrogen trapping at particles

Fine precipitates have drawn the most attention in the area of hydrogen trapping for HE mitigation because they have the potential to be incorporated into microstructures at significant number densities and hence provide a high trapping capacity [297,320,416–420]. They are also known to have a concomitant hardening effect [421,422]. Research in this area has mainly focused on BCC steels with carbide or nitride precipitates based on transition metals (e.g., titanium, vanadium, molybdenum, chromium, and niobium).

The use of microstructural traps to inhibit hydrogen assisted fatigue was theoretically described by Fernandez-Sousa et al. [196] for conditions where the loading cycle was significantly faster than the time required to deliver hydrogen to the process zone by either bulk diffusion or dislocation transport. Efficacy for IHE was experimentally demonstrated by Verbeken, Depover, and their co-workers, using a protocol combining TDA, SSRT, heat treatment (to control the number density of precipitates) and TEM for carbonitride characterization [320,416–420]. Fig. 33 [416] is an example of these results. Fig. 33A and B are example TEM images of carbide precipitates. TDA provided the hydrogen content of each specimen (Fig. 33C) for charging conditions in which the hydrogen reached equilibrium (hydrogen saturation) after a range of heat treatment conditions that led to various carbide densities. The hydrogen capacity was related to the number of carbides, increasing with the number of traps. All specimens were susceptible to HE when saturated with hydrogen. However, specimens with similar hydrogen contents that contain precipitates (here, TiC) displayed lower HE susceptibility (defined by ductility loss). In Fig. 33C, the as-quenched (As-Q) specimen of Alloy C was saturated at 7 wt ppm hydrogen, but the quenched-and-tempered (Q&T) Alloy C with more traps had a capacity of 12 wt ppm (highlighted in red). These specimens were heat-treated for 10 min, 2 h, and 1 h to create specimens that contained little TiC, a low number density of TiC (over-aged), and a high number density of TiC (peak-aged). Specimens were deliberately charged with 7 wt ppm hydrogen for mechanical testing, in order to match the hydrogen content in the differently aged specimens. The tensile strengths and elongations for charged and uncharged specimens in each condition are shown in Fig. 33 D. Those charged with 7 wt ppm hydrogen are marked 'charged*'. For ease of comparison, each heat treatment condition was labeled the uncharged (blue) and 7 wt ppm charged (red) stress-strain curve. The samples containing TiC (Fig. 33E and F) had significantly less loss in ductility when charged with hydrogen. In addition to the number density of carbides, the size of carbides can significantly impact hydrogen embrittlement resistance, particularly with variations in tempering time. In this work, titanium carbides were found to enlarge and lose coherency during the tempering process. Consequently, the corresponding carbides grow excessively large, and their interface with the matrix becomes too incoherent to adequately trap hydrogen from an electrochemical source.

Verbeken, Depover, and their co-workers studied steels containing vanadium, molybdenum, and chromium carbides [417–419], and also confirmed the beneficial role of these carbides for mitigating IHE, consistent with an earlier study of vanadium-alloyed steels [423]. A comparison of the mitigation efficacy of Mo, V, and Cr carbides found that, for similar steel strength, Mo and V carbides were more effective than Cr carbides for HE mitigation [424]. In alloys with the same composition, the microstructures with finer carbides and higher trap density trapped hydrogen more effectively [425]. For NbCs, small well-dispersed NbCs reduced HE susceptibility [426], although undissolved NbC precipitates remaining after austenization did not contribute measurably to HE resistance [427]. More recently, tantalum carbide precipitate (TaCs) was found to have a similar effect on HE mitigation [428,429].

For martensitic steels, Ti and Mo carbides were confirmed to have a positive effect on HE mitigation [424,430]. To further understand HE mechanisms in martensitic steels that contain oxide and carbide
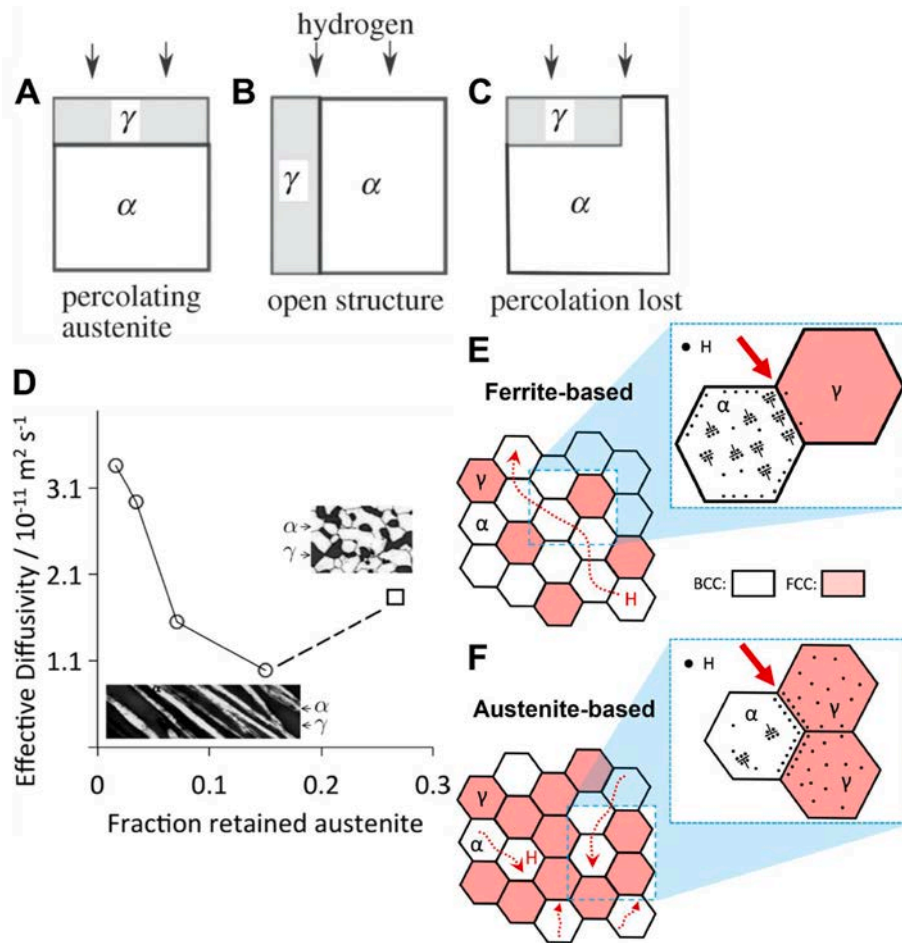
Fig. 35. Hydrogen percolation in austenite-containing steels. (A), (B), and (C) are schematic illustrations of a microstructure with percolating austenite, open structure, or a loss of percolation, respectively, with respect to the hydrogen ingress from the top. (D) shows hydrogen diffusivity as a function of the fraction of retained austenite for percolated austenite in a bainitic ferrite matrix (circular data points) compared to a conventional austenite-ferrite microstructure (square data point). (A)–(D) are reproduced from Ref. [334]. (E) and (F) are schematic illustrations of the hydrogen diffusion and distribution of a steel matrix with disconnected (E) and interconnected (F) austenite, reproduced from Ref. [435].

inclusions, Feaugas, Guedes, and their co-workers combined SSRT testing on notched samples with in-situ hydrogen permeation, TDA, fractography, and finite element modeling (FEM) [370] (Fig. 34). They concluded that the trapped hydrogen leads to ductility loss, but still ductile fracture, whereas the presence of both mobile and trapped hydrogen caused greater ductility loss and brittle fracture. They compared plate tensile martensitic samples with both V- and U-sharped notches under three conditions: i) uncharged, ii) hydrogen-charged and then room-temperature desorbed (leaving only trapped hydrogen in the specimens) and iii) in-situ hydrogen-charged with a high hydrogen flux near the surface. Fig. 34A shows that the specimens with trapped hydrogen (green curve) were slightly less ductile than the uncharged specimens (green), but the specimens with both mobile hydrogen and trapped hydrogen (blue curves, labeled H flux) were much more susceptible to HE. Other studies showed little HE in hydrogen pre-charged then desorbed specimens with a low hydrogen content at the surface [431–433]. Fig. 34B and C shows, respectively, the ductile (dimpled) fracture surface of the uncharged specimen and the specimen with trapped hydrogen. Both specimens contained oxides at the base of the dimples, but the specimens with trapped hydrogen also had dimples associated with small carbide inclusions (Fig. 34D). The specimens with high hydrogen flux at the surface displayed brittle fracture with the HE-characteristic quasi-cleavage (Fig. 34E). These observations suggest that inclusions and carbides, which are hydrogen traps, can enhance ductile fracture, but also be responsible for the nucleation of cracks if

diffusible hydrogen is present.

4.3. Microstructural engineering using second phases

Another strategy is to take advantage of the difference in hydrogen diffusivity in different phases [434]. Because hydrogen diffuses more slowly in austenite than in ferrite, percolated, three-dimensionally interconnected austenite (Fig. 35A) leads to lower hydrogen permeability than an open structure (Fig. 35B) or one in which the austenite is not fully interconnected (Fig. 35C). This is demonstrated in Fig. 35D, which shows the hydrogen diffusivity for steel samples with different fractions of austenite and different levels of interconnectivity. The first three datapoints (circles) show that the hydrogen diffusivity decreases with an increasing fraction of retained austenite in bainite, which can be associated with the degree of connectivity of the austenite. However, the hydrogen diffusivity of a conventional equiaxed ferritic-austenitic microstructure (square data point) is much higher, even though the fraction of austenite is higher, which can be explained by the fact that, unlike for bainite, the austenite is not interconnected (percolated) in this microstructure.

Utilizing austenite as a hydrogen barrier, Sun et al. examined the HE-induced deformation modes of two medium-Mn steels, one austenite-based (percolated) and one ferrite-based (not percolated) schematically illustrated in Fig. 35E and F, respectively [435]. Ductile deformation behavior of the ferrite-based microstructure was attributed to
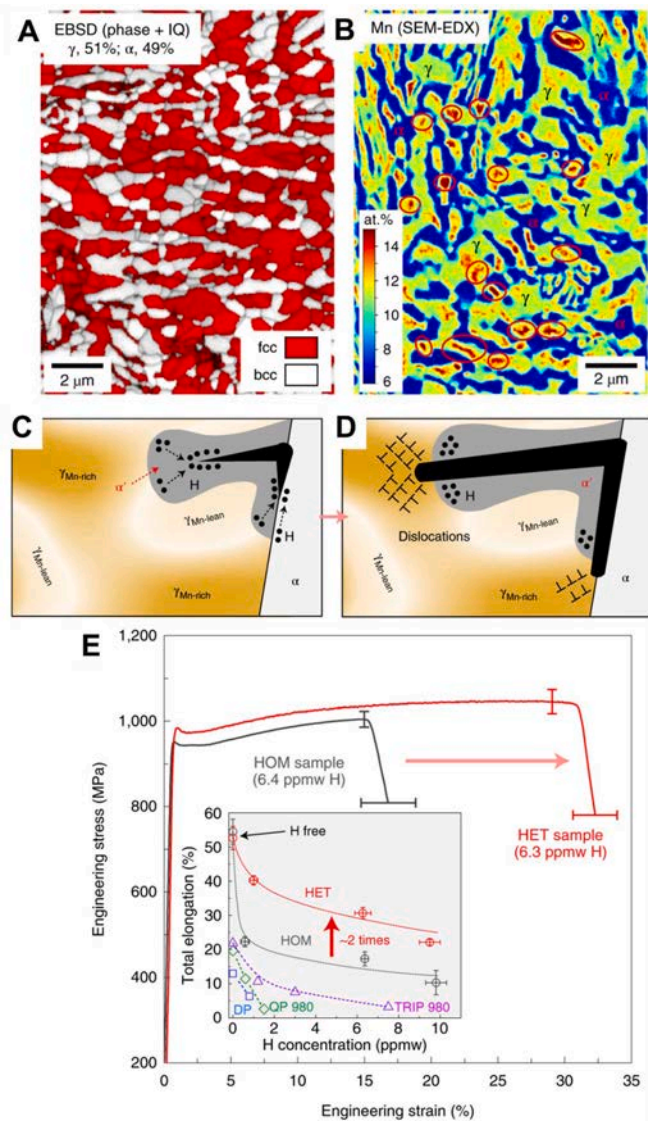
ARTICLE IN PRESS

Y.-S. Chen et al.   International Journal of Hydrogen Energy xxx (xxxx) xxx

Fig. 36. Chemical heterogeneity engineering for HE resistance. (A) and (B) are EBSD and EDX maps showing the austenitic phase distribution and Mn heterogeneity, respectively. (C) and (D) are schematic illustrations of the crack propagation in an austenite grain with Mn heterogeneity, where the Mn-rich regions are less prone to strain-induced martensitic transformation. (E) shows the HE performance of specimens with (red) and without (black) Mn heterogeneity, suggesting that the Mn heterogeneity led to higher HE resistance. Reproduced from Ref. [436]. (For interpretation of the references to color in this figure legend, the reader is referred to the Web version of this article.)

hydrogen-enhanced local plastic flow. The austenite-based microstructure failed by interfacial decohesion attributed to hydrogen accumulation at phase boundaries and a subsequent strain-induced martensitic transformation that is particularly susceptible to HE.

To further optimize the design of a HE-resistant microstructure, Sun et al. took advantage of typically undesirable chemical heterogeneity within the austenite grains in a medium-Mn steel [436] to achieve superior embrittlement resistance. Fig. 36A and B shows the austenite-ferrite dual phase microstructure with an uneven Mn distribution by electron backscattering diffraction (EBSD) and electron energy-dispersive X-ray spectroscopy (EDX), respectively. The mechanism is shown schematically in Fig. 36C and D. Mn enrichment increases the stability of the austenite and suppresses the phase transformation to martensite (Fig. 36C). The Mn-stabilized austenite remains ductile, blunts the crack tip, and ultimately reduces the rate of crack propagation

(Fig. 36D). Fig. 36E shows that HE resistance (represented by the elongation of hydrogen pre-charged specimens) of the specimen with Mn heterogeneity was improved by factor of two.

5. Summary and outlook

We have examined the variables, the causes, and the mechanisms of HE, introduced the principle of hydrogen trapping, described the techniques that have advanced the understanding of hydrogen trapping, and discussed several microstructural designs that can provide increased HE resistance. Much work has been devoted to understanding hydrogen trapping and many studies indicate that the incorporation of suitable traps can decrease EHE when the transport of hydrogen to the process zone is limited, but there is still much research required to further advance our understanding of HE and hydrogen trapping for the development of HE-resistant alloys.

Hydrogen interactions with engineering alloys are multiscale. An understanding requires an understanding of the interaction between hydrogen atoms and the atomic scale microstructural features (grain boundaries, phases, precipitates, solute atoms, solute clusters, interfaces, as well as the multi-scale features that control plasticity and failure (vacancies, dislocations, twins, voids, cracks).

Understanding the time-dependent, multiscale effects of an element that is difficult to measure is a formidable experimental and computational challenge. Experimental and modeling approaches are required from the atomistic to macro length scales. Recent experimental developments at the atomic length-scale, such as cryo-APT, together with improvements in in-situ testing, both on microscopes and at synchrotron and neutron beamlines, now mean that characterization is more viable. Modeling approaches (including new methods using quantum mechanics, crystal plasticity, evolutionary field models and dislocation dynamics) have recently improved to the point where the time and length scales accessible through experiment and modeling now meet.

Further effort to better relate the role of different microstructural traps on plasticity and fracture modes will allow the creation of hydrogen-induced deformation and fracture maps, similar to conventional plasticity and fracture maps with the additional consideration of the influence of hydrogen. Our fundamental understanding of hydrogen trapping so far has involved only unstressed specimens, and stress is likely to change the energetic landscape that drives trapping behavior. Given that mechanical load is always present, it is necessary in the future to consider the relationship between trap strength and applied stress to better understand the efficacy of hydrogen trapping for withstanding HE.

It may also be possible to develop 'hydrogen trap diagrams', similar to conventional phase diagrams but treat individual traps as thermodynamic entities, considering environmental influences such as temperature, pressure, stress, and hydrogen content related to the structural stability of the trap and the trapping strength for hydrogen, much like defect phase diagrams [437].

The embrittlement of high-strength engineering alloys in hydrogen-containing environments is a longstanding problem. Much has been done. There is much more to do. Despite some progress, the issue is still largely managed in industry by using lower strength, less hydrogen-susceptible alloys, sacrificing efficiencies in design. The dawn of a hydrogen economy completely changes the picture. The hydrogen economy requires the extensive use of engineering alloys for applications from electrolyzers to metallic membranes for gas separation, components for high-pressure hydrogen transport and storage (e.g. pipelines), compressors, liquid hydrogen containers and gas turbines for combustion. This new area brings renewed urgency to mitigating the hydrogen embrittlement challenge.

Declaration of competing interest

The authors declare that they have no known competing financial

interests or personal relationships that could have appeared to influence the work reported in this paper.

Acknowledgements

References

[1] IEA. The future of hydrogen. 2019. Paris.

[2] Raabe D, Tasan CC, Olivetti EA. Strategies for improving the sustainability of structural metals. Nature 2019;575. https://doi.org/10.1038/s41586-019-1702-5.

[3] Ma Y, Souza Filho IR, Bai Y, Schenk J, Patisson F, Beck A, van Bokhoven JA, Willinger MG, Li K, Xie D, Ponge D, Zaefferer S, Gault B, Mianroodi JR, Raabe D. Hierarchical nature of hydrogen-based direct reduction of iron oxides. Scripta Mater 2022;213:114571. https://doi.org/10.1016/J.SCRIPTAMAT.2022.114571.

[4] Daehn K, Basuhi R, Gregory J, Berlinger M, Somjit V, Olivetti EA. Innovations to decarbonize materials industries. Nat. Rev. Mater. 2021 2021;7(7):275–94. https://doi.org/10.1038/s41578-021-00376-y. 4.

[5] McQueen S, Stanford J, Satyapal S, Miller E, Stetson N, Papageorgopoulos D, Rustagi N, Arjona V, Adams J, Randolph K, Peterson D, Hill L, Koleva M, Reinhardt T, Frye E, Schrecengost R, Kokkinos A, Litynski J, Conrad R, Soloveichik G, Tew D, Litzelman S, Vetrano J, Onuschak R, Hahn A, Hsieh E, Costa R. Department of energy hydrogen program plan. https://doi.org/10.2172/1721803; 2020.

[6] Yan XL, Hino R, editors. Nuclear hydrogen production handbook. CRC Press; 2016. https://doi.org/10.1201/b10789.

[7] Hydrogen Shot | Department of energy, (n.d.). https://www.energy.gov/eere/fuelcells/hydrogen-shot (accessed April 26, 2023).

[8] Ministry of the Environment. Summary of Japan hydrogen strategy. 2020.

[9] Kwasi kwarteng, UK hydrogen strategy. 2021. London.

[10] The national hydrogen strategy. 2020. Berlin.

[11] Bru T, Rotevatn S. The Norwegian hydrogen strategy. 2020.

[12] O'Regan Seamus. The hydrogen strategy for Canada. 2020. Otawa.

[13] Ren X, Dong L, Xu D, Hu B. Challenges towards hydrogen economy in China. Int J Hydrogen Energy 2020;45:34326–45. https://doi.org/10.1016/J.IJHYDENE.2020.01.163.

[14] Finkel A. Australia's national hydrogen strategy. 2019.

[15] Lessons learned from a hydrogen explosion. https://www.powermag.com/lessons-learned-from-a-hydrogen-explosion/. [Accessed 23 December 2021].

[16] Ohaeri E, Eduok U, Szpunar J. Hydrogen related degradation in pipeline steel: a review. Int J Hydrogen Energy 2018;43:14584–617. https://doi.org/10.1016/j.ijhydene.2018.06.064.

[17] Ohaeri EG, Qin W, Szpunar J. A critical perspective on pipeline processing and failure risks in hydrogen service conditions. J Alloys Compd 2021;857:158240. https://doi.org/10.1016/j.jallcom.2020.158240.

[18] Laureys A, Depraetere R, Cauwels M, Depover T, Hertelé S, Verbeken K. Use of existing steel pipeline infrastructure for gaseous hydrogen storage and transport: a review of factors affecting hydrogen induced degradation. J Nat Gas Sci Eng 2022;101:104534. https://doi.org/10.1016/J.JNGSE.2022.104534.

[19] Li H, Niu R, Li W, Lu H, Cairney J, Chen YS. Hydrogen in pipeline steels: recent advances in characterization and embrittlement mitigation. J Nat Gas Sci Eng 2022;105:104709. https://doi.org/10.1016/J.JNGSE.2022.104709.

[20] Ustolin F, Paltrinieri N, Berto F. Loss of integrity of hydrogen technologies: a critical review. Int J Hydrogen Energy 2020;45. https://doi.org/10.1016/j.ijhydene.2020.06.021.

[21] Yang F, Wang T, Deng X, Dang J, Huang Z, Hu S, Li Y, Ouyang M. Review on hydrogen safety issues: incident statistics, hydrogen diffusion, and detonation process. Int J Hydrogen Energy 2021;46:31467–88. https://doi.org/10.1016/J.IJHYDENE.2021.07.005.

[22] Thompson AW, Bernstein IM. Selection of structural materials for hydrogen pipelines and storage vessels. Int J Hydrogen Energy 1977;2:163–73. https://doi.org/10.1016/0360-3199(77)90007-6.

[23] Martin V, Ashworth P, Petrova S, Wade B, Witt K. Public perceptions of hydrogen: 2021 national survey results. 2021.

[24] Townsend HE, Frank KH, Brignano B, Choi C. Hydrogen embrittlement testing and results of full-size ASTM A354 grade BD rods in the SFOBB. J I Coast Archaeol 2015;11:117–30. https://doi.org/10.3233/BRS-160096.

[25] Iordachescu M, Valiente A, Pérez-Guerrero M, Elices M. Environment-assisted failure of structural tendons for construction and building applications. Construct Build Mater 2018;159:499–507. https://doi.org/10.1016/J.CONBUILDMAT.2017.11.011.

[26] Martínez-Pañeda E. Progress and opportunities in modelling environmentally assisted cracking. RILEM Tech Lett 2021;6:70–7. https://doi.org/10.21809/RILEMTECHLETT.2021.145.

[27] Johnson WH. On some remarkable changes produced in iron and steel by the action of hydrogen and acids. Proc Roy Soc Lond 1874;23:168. https://royalsocietypublishing.org/doi/10.1098/rspl.1874.0024.

[28] Bhadeshia HKDH. Prevention of hydrogen embrittlement in steels. ISIJ Int 2016;56:24–36. <Go to ISI>://WOS:000370582400003.

[29] Martin ML, Connolly MJ, DelRio FW, Slifka AJ. Hydrogen embrittlement in ferritic steels. Appl Phys Rev 2020;7. <Go to ISI>://WOS:000575403700001.

[30] Robertson IM, Sofronis P, Nagao A, Martin ML, Wang S, Gross DW, Nygren KE. Hydrogen embrittlement understood. Metall Mater Trans 2015;46a:2323–41. <Go to ISI>://WOS:000353236700001.

[31] Lynch S. Hydrogen embrittlement phenomena and mechanisms. Corrosion Rev 2012;30:105–23. <Go to ISI>://WOS:000305586200002.

[32] Nagumo M. Fundamentals of hydrogen embrittlement. 1 online resource (ix, 239 pages), https://doi.org/10.1007/978-981-10-0161-1; 2016.

[33] Koyama M, Akiyama E, Lee YK, Raabe D, Tsuzaki K. Overview of hydrogen embrittlement in high-Mn steels. Int J Hydrogen Energy 2017;42:12706–23. <Go to ISI>://WOS:000403381500063.

[34] Dwivedi SK, Vishwakarma M. Hydrogen embrittlement in different materials: a review. Int J Hydrogen Energy 2018;43:21603–16. <Go to ISI>://WOS:000450377300035.

[35] Liu Q, Atrens A. A critical review of the influence of hydrogen on the mechanical properties of medium-strength steels. Corrosion Rev 2013;31:85–103. <Go to ISI>://WOS:000327732900002.

[36] Venezuela J, Liu QL, Zhang MX, Zhou QJ, Atrens A. A review of hydrogen embrittlement of martensitic advanced high-strength steels. Corrosion Rev 2016;34:153–86. <Go to ISI>://WOS:000377548900002.

[37] Liu QL, Zhou QJ, Venezuela J, Zhang MX, Wang JQ, Atrens A. A review of the influence of hydrogen on the mechanical properties of DP, TRIP, and TWIP advanced high-strength steels for auto construction. Corrosion Rev 2016;34:127–52. <Go to ISI>://WOS:000377548900001.

[38] Kappes M, Iannuzzi M, Carranza RM. Hydrogen embrittlement of magnesium and magnesium alloys: a review. J Electrochem Soc 2013;160:C168–78. <Go to ISI>://WOS:000316976800042.

[39] Suman S, Khan MK, Pathak M, Singh RN, Chakravartty JK. Hydrogen in zircaloy: mechanism and its impacts. Int J Hydrogen Energy 2015;40:5976–94. <Go to ISI>://WOS:000353753200023.

[40] Barrera O, Bombac D, Chen Y, Daff TD, Galindo-Nava E, Gong P, Haley D, Horton R, Katzarov I, Kermode JR, Liverani C, Stopher M, Sweeney F. Understanding and mitigating hydrogen embrittlement of steels: a review of experimental, modelling and design progress from atomistic to continuum. J Mater Sci 2018;53. https://doi.org/10.1007/s10853-017-1978-5.

[41] Chapman TP, Dye D, Rugg D. Hydrogen in Ti and Zr alloys: industrial perspective, failure modes and mechanistic understanding. Phil Trans Math Phys Eng Sci 2017;375. <Go to ISI>://WOS:000403358800015.

[42] Gangloff RP, Somerday BP. Gaseous hydrogen embrittlement of materials in energy technologies. Volume 2, Mechanisms, modelling and future developments. Oxford: Woodhead; 2012.

[43] Gangloff RP, Somerday BP. Gaseous hydrogen embrittlement of materials in energy technologies. Vol. 1, the problem, its characterisation and effects on particular alloy classes. Oxford: Woodhead Publishing; 2012.

[44] Alexander Stopher M, Rivera-Diaz-del-Castillo PEJ. Hydrogen embrittlement in bearing steels. Mater Sci Technol 2016;32:1184–93. https://doi.org/10.1080/02670836.2016.1156810.

[45] Rudomilova D, Prosek T, Luckeneder G. Techniques for investigation of hydrogen embrittlement of advanced high strength steels. Corrosion Rev 2018;36:413–34. <Go to ISI>://WOS:000444079400001.

[46] Maroef I, Olson DL, Eberhart M, Edwards GR. Hydrogen trapping in ferritic steel weld metal. Int Mater Rev 2002;47:191–223. <Go to ISI>://WOS:000178668000002.

[47] Nagumo M, Takai K. The predominant role of strain-induced vacancies in hydrogen embrittlement of steels: overview. Acta Mater 2019;165:722–33. <Go to ISI>://WOS:000457665100062.

[48] Hirth JP. 1980 institute of metals lecture the metallurgical-society-of-aime - effects of hydrogen on the properties of iron and steel. Metall Trans A 1980;11:861–90. <Go to ISI>://WOS:A1980JX38400001.

[49] Villalobos JC, Del-Pozo A, Campillo B, Mayen J, Serna S. Microalloyed steels through history until 2018: review of chemical composition, processing and hydrogen service. Metals 2018;8. <Go to ISI>://WOS:000435109300061.

[50] Dadfarnia M, Nagao A, Wang S, Martin ML, Somerday BP, Sofronis P. Recent advances on hydrogen embrittlement of structural materials. Int J Fract 2015;196:223–43. <Go to ISI>://WOS:000369433300009.

[51] Borchers C, Michler T, Pundt A. Effect of hydrogen on the mechanical properties of stainless steels. Adv Eng Mater 2008;10:11–23. <Go to ISI>://WOS:000253741600001.

[52] Grabke HJ, Gehrmann F, Riecke E. Hydrogen in microalloyed steels. Steel Res 2001;72:225–35. <Go to ISI>://WOS:000169766300010.

[53] Pillot S, Coudreuse L. 2 - hydrogen-induced disbonding and embrittlement of steels used in petrochemical refining. In: Gangloff RP, Somerday BP, editors. Gaseous hydrogen embrittlement of materials in energy technologies. Woodhead Publishing; 2012. p. 51–93. https://doi.org/10.1533/9780857093899.1.51.

[54] Atrens A, Liu Q, Zhou Q, Venezuela J, Zhang M. Evaluation of automobile service performance using laboratory testing, vol. 34; 2018. p. 1893–909. https://doi.org/10.1080/02670836.2018.1495903.

[55] Atrens A, Venezuela J, Liu Q, Zhou Q, Verbeken K, Tapia-Bastidas C, Gray E, Christien F, Wolski K. Electrochemical and mechanical aspects of hydrogen embrittlement evaluation of martensitic steels, encyclopedia of interfacial chemistry: Surf Sci Electrochem 2018:201–25. https://doi.org/10.1016/B978-0-12-409547-2.13770-9.

[56] Djukic MB, Bakic GM, Zeravcic VS, Sedmak A, Rajicic B. The synergistic action and interplay of hydrogen embrittlement mechanisms in steels and iron: localized plasticity and decohesion. Eng Fract Mech 2019;216. <Go to ISI>://WOS:000477573000044.

[57] Lynch S. Discussion of some recent literature on hydrogen-embrittlement mechanisms: addressing common misunderstandings. Corrosion Rev 2019;37:377–95. https://doi.org/10.1515/CORRREV-2019-0017/MACHINEREADABLECITATION/RIS.

[58] Gangloff RP. Hydrogen-assisted cracking. Compreh Struc Integr 2003;6:31–101. https://doi.org/10.1016/B0-08-043749-4/06134-6.

[59] Hoschke J, Chowdhury MFW, Venezuela J, Atrens A. A review of hydrogen embrittlement in gas transmission pipeline steels. Corrosion Rev 2023. https://doi.org/10.1515/CORRREV-2022-0052/XML.

[60] Lovicu G, Bottazzi M, D'Aiuto F, de Sanctis M, Dimatteo A, Santus C, Valentini R. Hydrogen embrittlement of automotive advanced high-strength steels. Metall Mater Trans A 2012;43a:4075–87. <Go to ISI>://WOS:000309239900018.

[61] Choo WY, Lee JY. Hydrogen trapping phenomena in carbon-steel. J Mater Sci 1982;17:1930–8. <Go to ISI>://WOS:A1982PB45000011.

[62] Thomas RLS, Scully JR, Gangloff RP. Internal hydrogen embrittlement of ultrahigh-strength AERMET 100 steel. Metallurg Mater Transac A 2003 2003;34 (34):327–44. https://doi.org/10.1007/S11661-003-0334-3. 2.

[63] Ootsuka S, Fujita S, Tada E, Nishikata A, Tsuru T. Evaluation of hydrogen absorption into steel in automobile moving environments. Corrosion Sci 2015;98:430–7. https://doi.org/10.1016/J.CORSCI.2015.05.049.

[64] van Leeuwen HP. The kinetics of hydrogen embrittlement: a quantitative diffusion model. Eng Fract Mech 1974;6:141–61. https://doi.org/10.1016/0013-7944(74)90053-8.

[65] Martínez-Pañeda E, Díaz A, Wright L, Turnbull A. Generalised boundary conditions for hydrogen transport at crack tips. Corrosion Sci 2020;173:108698. https://doi.org/10.1016/J.CORSCI.2020.108698.

[66] Murakami Y, Matsunaga H. The effect of hydrogen on fatigue properties of steels used for fuel cell system. Int J Fatig 2006;28:1509–20. <Go to ISI>://WOS:000240811300011.

[67] Martínez-Pañeda E, Harris ZD, Fuentes-Alonso S, Scully JR, Burns JT. On the suitability of slow strain rate tensile testing for assessing hydrogen embrittlement susceptibility. Corrosion Sci 2020;163:108291. https://doi.org/10.1016/J.CORSCI.2019.108291.

[68] Henry Holroyd N, Burnett TL, Palmer BC, Lewandowski JJ. Estimation of environment-induced crack growth rate as a function of stress intensity factors generated during slow strain rate testing of aluminum alloys. Corrosion Rev 2019;37:499–506. https://doi.org/10.1515/CORRREV-2019-0031/MACHINEREADABLECITATION/RIS.

[69] Sampath D, Akid R, Morana R. Estimation of crack initiation stress and local fracture toughness of Ni-alloys 945X (UNS N09946) and 718 (UNS N07718) under hydrogen environment via fracture surface topography analysis. Eng Fract Mech 2018;191:324–43. https://doi.org/10.1016/J.ENGFRACMECH.2017.12.010.

[70] Golahmar A, Kristensen PK, Niordson CF, Martínez-Pañeda E. A phase field model for hydrogen-assisted fatigue. Int J Fatig 2022;154:106521. https://doi.org/10.1016/J.IJFATIGUE.2021.106521.

[71] Li H, Venezuela J, Zhou Q, Shi Z, Yan M, Knibbe R, Zhang M, Dong F, Atrens A. Effect of plastic strain damage on the hydrogen embrittlement of a dual-phase (DP) and a quenching and partitioning (Q&P) advanced high-strength steel. Mater Sci Eng 2020;785:139343. https://doi.org/10.1016/J.MSEA.2020.139343.

[72] Li H, Venezuela J, Qian Z, Zhou Q, Shi Z, Yan M, Knibbe R, Zhang M, Dong F, Atrens A. Hydrogen fracture maps for sheared-edge-controlled hydrogen-delayed fracture of 1180 MPa advanced high-strength steels. Corrosion Sci 2021;184:109360. https://doi.org/10.1016/J.CORSCI.2021.109360.

[73] Atrens A, Venezuela J, Liu Q, Zhou Q, Verbeken K, Tapia-Bastidas C, Gray E, Christien F, Wolski K. Electrochemical and mechanical aspects of hydrogen embrittlement evaluation of martensitic steels, encyclopedia of interfacial chemistry: Surf Sci Electrochem 2018:201–25. https://doi.org/10.1016/B978-0-12-409547-2.13770-9.

[74] Ramamurthy S, Atrens A. Stress corrosion cracking of high-strength steels. Corrosion Rev 2013;31:1–31. https://doi.org/10.1515/CORRREV-2012-0018/MACHINEREADABLECITATION/RIS.

[75] Ogawa Y, Hosoi H, Tsuzaki K, Redarce T, Takakuwa O, Matsunaga H. Hydrogen, as an alloying element, enables a greater strength-ductility balance in an Fe-Cr-Ni-based, stable austenitic stainless steel. Acta Mater 2020;199. https://doi.org/10.1016/j.actamat.2020.08.024.

[76] Wada K, Yamabe J, Matsunaga H. Mechanism of hydrogen-induced hardening in pure nickel and in a copper–nickel alloy analyzed by micro Vickers hardness testing. Mater Sci Eng 2021;805. https://doi.org/10.1016/j.msea.2020.140580.

[77] Eliezer D, Eliaz N, Senkov ON, Froes FH. Positive effects of hydrogen in metals. Mater Sci Eng, A 2000;280:220–4. https://doi.org/10.1016/S0921-5093(99)00670-X.

[78] Froes FH, Senkov ON, Qazi JI. Hydrogen as a temporary alloying element in titanium alloys: thermohydrogen processing, vol. 49; 2013. p. 227–45. https://doi.org/10.1179/095066004225010550.

[79] Martin ML, Robertson IM, Sofronis P. Interpreting hydrogen-induced fracture surfaces in terms of deformation processes: a new approach. Acta Mater 2011;59:3680–7. <Go to ISI>://WOS:000290692600034.

[80] Martin ML, Fenske JA, Liu GS, Sofronis P, Robertson IM. On the formation and nature of quasi-cleavage fracture surfaces in hydrogen embrittled steels. Acta Mater 2011;59:1601–6. <Go to ISI>://WOS:000287265100028.

[81] Xing X, Cheng R, Cui G, Liu JG, Gou JX, Yang C, Li ZL, Yang F. Quantification of the temperature threshold of hydrogen embrittlement in X90 pipeline steel. Mater Sci Eng A-Struc Mater Prop Microstruc Process 2021;800. <Go to ISI>://WOS:000593914500002.

[82] Zhang L, Imade M, An B, Wen M, Iijima T, Fukuyama S, Yokogawa K. Internal reversible hydrogen embrittlement of austenitic stainless steels based on type 316 at low temperatures. ISIJ Int 2012;52:240–6. <Go to ISI>://WOS:000301323300012.

[83] Harris ZD, Lawrence SK, Medlin DL, Guetard G, Burns JT, Somerday BP. Elucidating the contribution of mobile hydrogen-deformation interactions to hydrogen-induced intergranular cracking in polycrystalline nickel. Acta Mater 2018;158:180–92. https://doi.org/10.1016/J.ACTAMAT.2018.07.043.

[84] Momotani Y, Shibata A, Terada D, Tsuji N. Effect of strain rate on hydrogen embrittlement in low-carbon martensitic steel. Int J Hydrogen Energy 2017;42:3371–9. <Go to ISI>://WOS:000397685800061.

[85] Depover T, Laureys A, Escobar DP, van den Eeckhout E, Wallaert E, Verbeken K. Understanding the interaction between a steel microstructure and hydrogen. Materials 2018;11. <Go to ISI>://WOS:000434711700048.

[86] Koyama M, Rohwerder M, Tasan CC, Bashir A, Akiyama E, Takai K, Raabe D, Tsuzaki K. Recent progress in microstructural hydrogen mapping in steels: quantification, kinetic analysis, and multi-scale characterisation. Mater Sci Technol 2017;33:1481–96. <Go to ISI>://WOS:000406476600002.

[87] Chen Y-S, Lu H, Liang J, Rosenthal A, Liu H, Sneddon G, McCarroll I, Zhao Z, Li W, Guo A, Cairney JM. Observation of hydrogen trapping at dislocations, grain boundaries, and precipitates. Science (1979) 2020;367. https://doi.org/10.1126/science.aaz0122.

[88] Depover T, Pérez Escobar D, Wallaert E, Zermout Z, Verbeken K. Effect of hydrogen charging on the mechanical properties of advanced high strength steels. Int J Hydrogen Energy 2014;39:4647–56. https://doi.org/10.1016/J.IJHYDENE.2013.12.190.

[89] Martínez-Pañeda E, del Busto S, Niordson CF, Betegón C. Strain gradient plasticity modeling of hydrogen diffusion to the crack tip. Int J Hydrogen Energy 2016;41:10265–74. https://doi.org/10.1016/J.IJHYDENE.2016.05.014.

[90] Burns JT, Harris ZD, Dolph JD, Gangloff RP. Measurement and modeling of hydrogen environment-assisted cracking in a Ni-Cu-Al-Ti superalloy. Metall Mater Trans A Phys Metall Mater Sci 2016;47:990–7. https://doi.org/10.1007/S11661-015-3315-4/FIGURES/5.

[91] Takasawa K, Ikeda R, Ishikawa N, Ishigaki R. Effects of grain size and dislocation density on the susceptibility to high-pressure hydrogen environment embrittlement of high-strength low-alloy steels. Int J Hydrogen Energy 2012;37:2669–75. <Go to ISI>://WOS:000301157300066.

[92] Gong P, Nutter J, Rivera-Diaz-Del-Castillo PEJ, Rainforth WM. Hydrogen embrittlement through the formation of low-energy dislocation nanostructures in nanoprecipitation-strengthened steels. Sci Adv 2020;6. <Go to ISI>://WOS:000592174000014.

[93] Dadfarnia M, Somerday BP, Schembri PE, Sofronis P, Foulk JW, Nibur KA, Balch DK. On modeling hydrogen-induced crack propagation under sustained load. JOM (J Occup Med) 2014;66:1390–8. https://doi.org/10.1007/S11837-014-1050-8/FIGURES/10.

[94] Anand L, Mao Y, Talamini B. On modeling fracture of ferritic steels due to hydrogen embrittlement. J Mech Phys Solid 2019;122:280–314. https://doi.org/10.1016/J.JMPS.2018.09.012.

[95] Golahmar A, Kristensen PK, Niordson CF, Martínez-Pañeda E. A phase field model for hydrogen-assisted fatigue. Int J Fatig 2022;154:106521. https://doi.org/10.1016/J.IJFATIGUE.2021.106521.

[96] Serebrinsky S, Carter EA, Ortiz M. A quantum-mechanically informed continuum model of hydrogen embrittlement. J Mech Phys Solid 2004;52:2403–30. https://doi.org/10.1016/J.JMPS.2004.02.010.

[97] Westlake DG. A generalized model for hydrogen embrittlement. Asm Transac Q 1969;62:1000. <Go to ISI>://WOS:A1969F430300020.

[98] Motta AT, Capolungo L, Chen LQ, Cinbiz MN, Daymond MR, Koss DA, Lacroix E, Pastore G, Simon PCA, Tonks MR, Wirth BD, Zikry MA. Hydrogen in zirconium alloys: a review. J Nucl Mater 2019;518:440–60. https://doi.org/10.1016/J.JNUCMAT.2019.02.042.

[99] Jia YJ, Han WZ. Mechanisms of hydride nucleation, growth, reorientation, and embrittlement in zirconium: a review. Materials 2023 2023;16:2419. https://doi.org/10.3390/MA16062419. Vol. 16, Page 2419.

[100] Birnbaum HK. Mechanical-properties of metal-hydrides. J Less Common Met 1984;104:31–41. <Go to ISI>://WOS:A1984AAJ3800004.

[101] Tal-Gutelmacher E, Eliezer D. The hydrogen embrittlement of titanium-based alloys. JOM 2005;57:46–9. <Go to ISI>://WOS:000231964000008.

[102] Winzer N, Atrens A, Song G, Ghali E, Dietzel W, Kainer KU, Hort N, Blawert C. A critical review of the stress corrosion cracking (SCC) of magnesium alloys. Adv Eng Mater 2005;7:659–93. https://doi.org/10.1002/ADEM.200500071.

[103] Winzer N, Atrens A, Dietzel W, Song G, Kainer KU. Evaluation of the delayed hydride cracking mechanism for transgranular stress corrosion cracking of magnesium alloys. Mater Sci Eng 2007;466:18–31. https://doi.org/10.1016/J.MSEA.2007.03.020.

[104] Wayman ML, Smith GC. Effects of hydrogen on deformation and fracture of nickel-iron alloys. Acta Metall 1971;19:227. <Go to ISI>://WOS:A19711754700007.

[105] Song J, Curtin WA. A nanoscale mechanism of hydrogen embrittlement in metals. Acta Mater 2011;59:1557–69. <Go to ISI>://WOS:000287265100024.

[106] Song J, Curtin WA. Atomic mechanism and prediction of hydrogen embrittlement in iron. Nat Mater 2013;12:145–51. <Go to ISI>://WOS:000314627000022.

[107] Shishvan SS, Csányi G, Deshpande VS. Hydrogen induced fast-fracture. J Mech Phys Solid 2020;134:103740. https://doi.org/10.1016/J.JMPS.2019.103740.

[108] v Badding J, Hemley RJ, Mao HK. High-pressure chemistry of hydrogen in metals - insitu study of iron hydride. Science (1979) 1991;253:421–4. <Go to ISI>://WOS:A1991FY28800032.

[109] Johnson HH, Morlet JG, Troiano AR. Hydrogen, crack initiation, and delayed failure in steel, vol. 212. Transactions of the American Institute of Mining and Metallurgical Engineers; 1958. p. 528–36. <Go to ISI>://WOS:A1958WZ70000160.

[110] Oriani RA. Mechanistic theory of hydrogen embrittlement of steels, vol. 76. Berichte Der Bunsen-Gesellschaft Fur Physikalische Chemie.; 1972. p. 848. <Go to ISI>://WOS:A1972N380200061.

[111] Jiang DE, Carter EA. First principles assessment of ideal fracture energies of materials with mobile impurities: implications for hydrogen embrittlement of metals. Acta Mater 2004;52:4801–7. <Go to ISI>://WOS:000223794000009.

[112] van der Ven A, Ceder G. Impurity-induced van der Waals transition during decohesion. Phys Rev B 2003;67:060101. https://doi.org/10.1103/PhysRevB.67.060101.

[113] Tehranchi A, Curtin WA. Atomistic study of hydrogen embrittlement of grain boundaries in nickel: I. Fracture. J Mech Phys Solid 2017;101. https://doi.org/10.1016/j.jmps.2017.01.020.

[114] Alvaro A, Thue Jensen I, Kheradmand N, Løvvik OM, Olden V. Hydrogen embrittlement in nickel, visited by first principles modeling, cohesive zone simulation and nanomechanical testing. Int J Hydrogen Energy 2015;40:16892–900. https://doi.org/10.1016/J.IJHYDENE.2015.06.069.

[115] Katzarov IH, Paxton AT. Hydrogen embrittlement II. Analysis of hydrogen-enhanced decohesion across (111) planes in α -Fe. Phys Rev Mater 2017;1:033603. https://doi.org/10.1103/PHYSREVMATERIALS.1.033603/FIGURES/12/MEDIUM.

[116] Martínez-Pañeda E, Deshpande VS, Niordson CF, Fleck NA. The role of plastic strain gradients in the crack growth resistance of metals. J Mech Phys Solid 2019;126:136–50. https://doi.org/10.1016/J.JMPS.2019.02.011.

[117] Martinez-Paneda E, Niordson CF, Gangloff RP. Strain gradient plasticity-based modeling of hydrogen environment assisted cracking. Acta Mater 2016;117:321–32. <Go to ISI>://WOS:000383005300031.

[118] Kristensen PK, Niordson CF, Martínez-Pañeda E. A phase field model for elastic-gradient-plastic solids undergoing hydrogen embrittlement. J Mech Phys Solid 2020;143:104093. https://doi.org/10.1016/J.JMPS.2020.104093.

[119] Tehranchi A, Curtin WA. The role of atomistic simulations in probing hydrogen effects on plasticity and embrittlement in metals. Eng Fract Mech 2019;216. <Go to ISI>://WOS:000477573000043.

[120] van der Ven A, Ceder G. The thermodynamics of decohesion. Acta Mater 2004;52:1223–35. <Go to ISI>://WOS:000220236100015.

[121] Kirchheim R. Reducing grain boundary, dislocation line and vacancy formation energies by solute segregation. I. Theoretical background. Acta Mater 2007;55:5129–38. <Go to ISI>://WOS:000249896100020.

[122] Lejcek P, Sob M, Paidar V. Interfacial segregation and grain boundary embrittlement: an overview and critical assessment of experimental data and calculated results. Prog Mater Sci 2017;87:83–139. <Go to ISI>://WOS:000398676100003.

[123] Cho L, Bradley PE, Lauria DS, Connolly MJ, Seo EJ, Findley KO, Speer JG, Golem L, Slifka AJ. Effects of hydrogen pressure and prior austenite grain size on the hydrogen embrittlement characteristics of a press-hardened martensitic steel. Int J Hydrogen Energy 2021;46:24425–39. <Go to ISI>://WOS:000669046300006.

[124] Bechtle S, Kumar M, Somerday BP, Launey ME, Ritchie RO. Grain-boundary engineering markedly reduces susceptibility to intergranular hydrogen embrittlement in metallic materials. Acta Mater 2009;57:4148–57. <Go to ISI>://WOS:000268653000018.

[125] Tsuru T, Shimizu K, Yamaguchi M, Itakura M, Ebihara K, Bendo A, Matsuda K, Toda H. Hydrogen-accelerated spontaneous microcracking in high-strength aluminium alloys. Sci Rep 2020;10. <Go to ISI>://WOS:000563469000001.

[126] Beachem CD. New model for hydrogen-assisted cracking (hydrogen embrittlement). Metall Trans A 1972;3:437. <Go to ISI>://WOS:A1972L595400009.

[127] Birnbaum HK, Sofronis P. Hydrogen-enhanced localized plasticity - a mechanism for hydrogen-related fracture. Mater Sci Eng A-Struc Mater Prop Microstruc Process 1994;176:191–202. <Go to ISI>://WOS:A1994ND32100027.

[128] Huang L, Chen D, Xie D, Li S, Zhang Y, Zhu T, Raabe D, Ma E, Li J, Shan Z. Quantitative tests revealing hydrogen-enhanced dislocation motion in α-iron. Nat Mater 2023:1–7. https://doi.org/10.1038/s41563-023-01537-w. 2023.

[129] Kirchheim R. Reducing grain boundary, dislocation line and vacancy formation energies by solute segregation II. Experimental evidence and consequences. Acta Mater 2007;55:5139–48. <Go to ISI>://WOS:000249896100021.

[130] Cottrell AH, Bilby BA. Dislocation theory of yielding and strain ageing of iron. Proc Phys Soc London Section A 1949;62:49–62. <Go to ISI>://WOS:A1949YE40500007.

[131] Robertson IM. The effect of hydrogen on dislocation dynamics. Eng Fract Mech 2001;68:671–92. <Go to ISI>://WOS:000167956200004.

[132] Ferreira PJ, Robertson IM, Birnbaum HK. Hydrogen effects on the interaction between dislocations. Acta Mater 1998;46:1749–57. <Go to ISI>://WOS:000072632800027.

[133] Pundt A, Kirchheim R. Hydrogen in metals: microstructural aspects. Annu Rev Mater Res 2006;36:555–608. <Go to ISI>://WOS:000239807500018.

[134] Liu Q, Zhou Q, Venezuela J, Zhang M, Atrens A. Evaluation of the influence of hydrogen on some commercial DP, Q&P and TWIP advanced high-strength steels during automobile service. Eng Fail Anal 2018;94:249–73. https://doi.org/10.1016/J.ENGFAILANAL.2018.08.011.

[135] Venezuela J, Hill T, Zhou Q, Li H, Shi Z, Dong F, Knibbe R, Zhang M, Dargusch MS, Atrens A. Hydrogen-induced fast fracture in notched 1500 and 1700 MPa class automotive martensitic advanced high-strength steel. Corrosion Sci 2021;188:109550. https://doi.org/10.1016/J.CORSCI.2021.109550.

[136] Saito K, Hirade T, Takai K. Hydrogen desorption spectra from excess vacancy-type defects enhanced by hydrogen in tempered martensitic steel showing quasi-cleavage fracture. Metall Mater Trans A 2019;50a:5091–102. <Go to ISI>://WOS:000491296000015.

[137] Sakaki K, Kawase T, Hirato M, Mizuno M, Araki H, Shirai Y, Nagumo M. The effect of hydrogen on vacancy generation in iron by plastic deformation. Scripta Mater 2006;55:1031–4. <Go to ISI>://WOS:000241242500016.

[138] Oudriss A, Martin F, Creus J, Bouhattate J, Marchetti L, Feaugas X. Contributions of polarized dislocation walls, internal stresses and vacancies on hydrogen trapping processes in tensile strengthening (100) nickel single crystal. Acta Mater 2023;245:118622. https://doi.org/10.1016/J.ACTAMAT.2022.118622.

[139] Jo KR, Cho L, Sulistiyo DH, Seo EJ, Kim SW, de Cooman BC. Effects of Al-Si coating and Zn coating on the hydrogen uptake and embrittlement of ultra-high strength press-hardened steel. Surf Coat Technol 2019;374:1108–19. <Go to ISI>://WOS:000486360000109.

[140] Cho L, Sulistiyo DH, Seo EJ, Jo KR, Kim SW, Oh JK, Cho YR, de Cooman BC. Hydrogen absorption and embrittlement of ultra-high strength aluminized press hardening steel. Mater Sci Eng A-Struc Mater Prop Microstruc Process 2018;734:416–26. <Go to ISI>://WOS:000445993900046.

[141] Yoo J, Kim S, Jo MC, Kim S, Oh J, Kim SH, Lee S, Sohn SS. Effects of Al-Si coating structures on bendability and resistance to hydrogen embrittlement in 1.5-GPa-grade hot-press-forming steel. Acta Mater 2022;225:117561. https://doi.org/10.1016/J.ACTAMAT.2021.117561.

[142] Mori K, Bariani PF, Behrens BA, Brosius A, Bruschi S, Maeno T, Merklein M, Yanagimoto J. Hot stamping of ultra-high strength steel parts. CIRP Ann-Manuf Technol 2017;66:755–77. <Go to ISI>://WOS:000411553700009.

[143] Araujo LS, de Almeida LH, dos Santos DS. Hydrogen embrittlement of a hard chromium plated cylinder assembly. Eng Fail Anal 2019;103:259–65. <Go to ISI>://WOS:000471614600022.

[144] Han H, Lee K, Park S, Park S, Song M. The effect of baking time, fillet radius, and hardness on the lifecycles of pole fastening screws in an electric motor with hydrogen embrittlement. Eng Fail Anal 2015;48:62–77. <Go to ISI>://WOS:000348508100006.

[145] Yu SH, Lyu A, Jang IS, Park HS, Jang M, Lee KY, Lee YK. Hydrogen absorption, desorption and embrittlement of Zn and ZnNi-electrodeposited steels. J Mater Res Technol-Jmr&T 2021;11:1604–10. <Go to ISI>://WOS:000640315400008.

[146] Behera P, Rajagopalan SK, Brahimi S, Venturella CA, Gaydos SP, Straw RJ, Yue S. Effect of brush plating process variables on the microstructures of Cd and ZnNi coatings and hydrogen embrittlement. Surf Coat Technol 2021;417. <Go to ISI>://WOS:000655577700005.

[147] Carr MJ, Robinson MJ. The effects of zinc alloy electroplating on the hydrogen embrittlement of high-strength steels. Trans Inst Met Finish 1995;73:58–64. <Go to ISI>://WOS:A1995RQ69100013.

[148] Laliberte-Riverin S, Bellemare J, Sirois F, Brochu M. Internal hydrogen embrittlement of pre-cracked, cadmium-plated AISI 4340 high strength steel with sustained load tests and incremental step-loading tests. Eng Fract Mech 2020;223. <Go to ISI>://WOS:000504021200023.

[149] An T, Zhang S, Feng M, Luo BW, Zheng SQ, Chen LQ, Zhang L. Synergistic action of hydrogen gas and weld defects on fracture toughness of X80 pipeline steel. Int J Fatig 2019;120:23–32. <Go to ISI>://WOS:000458226900003.

[150] Pandey C, Mahapatra MM, Kumar P, Saini N. Some studies on P91 steel and their weldments. J Alloys Compd 2018;743:332–64. <Go to ISI>://WOS:000427511200039.

[151] vander Vennet S, de Seranno T, Depover T, Verbeken K. Assessment of the hydrogen interaction on the mechanical integrity of a welded martensitic steel, vol. 37; 2021. p. 250–7. https://doi.org/10.1080/02670836.2021.1885099.

[152] Chung Y. Validity of caltrans' environmental hydrogen embrittlement test on grade BD anchor rods in the SAS span. https://www.sacbee.com/news/investigations/bay-bridge/article4254712.ece/BINARY/Validity%20of%20Caltrans%27%20EHE%20Tests.pdf; 2014.

[153] Kim HJ, Park HK, Lee CW, Yoo BG, Jung HY. Baking effect on desorption of diffusible hydrogen and hydrogen embrittlement on hot-stamped boron martensitic steel. Metals 2019;9. <Go to ISI>://WOS:000475356500020.

[154] Morsdorf L, Emelina E, Gault B, Herbig M, Tasan CC. Carbon redistribution in quenched and tempered lath martensite. Acta Mater 2021;205. https://doi.org/10.1016/j.actamat.2020.116521.

[155] Pressouyre GM. Trap theory of Hydrogen embrittlement. Acta Metall 1980;28. https://doi.org/10.1016/0001-6160(80)90106-6.

[156] Venezuela J, Tapia-Bastidas C, Zhou Q, Depover T, Verbeken K, Gray E, Liu Q, Liu Q, Zhang M, Atrens A. Determination of the equivalent hydrogen fugacity during electrochemical charging of 3.5NiCrMoV steel. Corrosion Sci 2018;132. https://doi.org/10.1016/j.corsci.2017.12.018.

[157] Venezuela J, Gray E, Liu Q, Zhou Q, Tapia-Bastidas C, Zhang M, Atrens A. Equivalent hydrogen fugacity during electrochemical charging of some martensitic advanced high-strength steels. Corrosion Sci 2017;127. https://doi.org/10.1016/j.corsci.2017.08.011.

[158] Liu Q, Gray E, Venezuela J, Zhou Q, Tapia-Bastidas C, Zhang M, Atrens A. Equivalent hydrogen fugacity during electrochemical charging of 980DP steel determined by thermal desorption spectroscopy. Adv Eng Mater 2018;20. https://doi.org/10.1002/adem.201700469.

[159] Kiuchi K, McLellan RB. The solubility and diffusivity of hydrogen in well-annealed and deformed iron. Acta Metall 1983;31. https://doi.org/10.1016/0001-6160(83)90192-X.

[160] Long Y, Song W, Fu A, Xie J, Feng Y, Bai Z, Yin C, Ma Q, Ji N, Kuang X. Combined effect of hydrogen embrittlement and corrosion on the cracking behaviour of C110 low alloy steel in O2-contaminated H2S environment. Corrosion Sci 2022;194:109926. https://doi.org/10.1016/J.CORSCI.2021.109926.

[161] Briottet L, Batisse R, de Dinechin G, Langlois P, Thiers L. Recommendations on X80 steel for the design of hydrogen gas transmission pipelines. Int J Hydrogen Energy 2012;37:9423–30. Go to ISI>://WOS:000304976300048.

[162] Holbrook JH, Cialone HJ, Collings EW, Drauglis EJ, Scott PM, Mayfield ME. 5 - control of hydrogen embrittlement of metals by chemical inhibitors and coatings. In: Gangloff RP, Somerday BP, editors. Gaseous hydrogen embrittlement of materials in energy technologies. Woodhead Publishing; 2012. p. 129–53. https://doi.org/10.1533/9780857095374.1.129.

[163] Somerday BP, Sofronis P, editors. International hydrogen conference (IHC 2016): materials performance in hydrogen environments. ASME Press; 2017. https://doi.org/10.1115/1.861387.

[164] Staykov A, Yamabe J, Somerday BP. Effect of hydrogen gas impurities on the hydrogen dissociation on iron surface. Int J Quant Chem 2014;114:626–35. https://doi.org/10.1002/qua.24633.

[165] Somerday BP, Sofronis P, Nibur KA, San Marchi C, Kirchheim R. Elucidating the variables affecting accelerated fatigue crack growth of steels in hydrogen gas with low oxygen concentrations. Acta Mater 2013;61:6153–70. https://doi.org/10.1016/j.actamat.2013.07.001.

[166] Staykov A, Komoda R, Kubota M, Ginet P, Barbier F, Furtado J. Coadsorption of CO and H2 on an iron surface and its implication on the hydrogen embrittlement of iron. J Phys Chem C 2019;123:30265–73. https://doi.org/10.1021/acs.jpcc.9b06927.

[167] Ooi SW, Yan P, Vegter RH. Black oxide coating and its effectiveness on prevention of hydrogen uptake. Mater Sci Technol 2019;35:12–25. <Go to ISI>://WOS:000451829600002.

[168] Forcey KS, Ross DK, Wu CH. The Formation of hydrogen permeation barriers on steels by aluminizing. J Nucl Mater 1991;182:36–51. <Go to ISI>://WOS:A1991FT83700005.

[169] He D, Li S, Liu XP, Zhang C, Yu QH, Wang SM, Jiang LJ. Preparation of Cr2O3 film by MOCVD as hydrogen permeation barrier. Fusion Eng Des 2014;89:35–9. <Go to ISI>://WOS:000331662900007.

[170] Duminica FD, vanden Eynde X, Mandy M, Nabi B, Georges C, Sturel T, Drillet P, Grigorieva R. Investigation of PVD thin films as hydrogen barriers in aluminized press hardened steels (PHS). Surf Coat Technol 2020;397. <Go to ISI>://WOS:000543496400016.

[171] Li S, He D, Liu XP, Wang SM, Jiang LJ. Deuterium permeation of amorphous alumina coating on 316L prepared by MOCVD. J Nucl Mater 2012;420:405–8. <Go to ISI>://WOS:000300462300056.

[172] Li M, Xie DG, Ma E, Li J, Zhang XX, Shan ZW. Effect of hydrogen on the integrity of aluminium-oxide interface at elevated temperatures. Nat Commun 2017;8. <Go to ISI>://WOS:000394458700001.

[173] Li XF, Zhang J, Ma MM, Song XL. Effect of shot peening on hydrogen embrittlement of high strength steel. Int J Miner Metall Mater 2016;23:667–75. https://doi.org/10.1007/s12613-016-1279-z.

[174] Takakuwa O, Soyama H. Preventing hydrogen embrittlement in stainless steel by means of compressive stress induced by cavitation peening. J Eng-Joe 2015;1–4. https://doi.org/10.1049/joe.2015.0065.

[175] Kim J, Hall D, Yan H, Shi Y, Joseph S, Fearn S, Chater RJ, Dye D, Tasan CC. Roughening improves hydrogen embrittlement resistance of Ti-6Al-4V. Acta Mater 2021;220. https://doi.org/10.1016/j.actamat.2021.117304.

[176] Marchi C, Somerday B, Robinson S. Permeability, solubility and diffusivity of hydrogen isotopes in stainless steels at high gas pressures. Int J Hydrogen Energy 2007;32. https://doi.org/10.1016/j.ijhydene.2006.05.008.

[177] Liu Q, Atrens AD, Shi ZM, Verbeken K, Atrens A. Determination of the hydrogen fugacity during electrolytic charging of steel. Corrosion Sci 2014;87:239–58. <Go to ISI>://WOS:000341334800028.

[178] Zhao Y, Park J-M, Lee D-H, Song EJ, Suh J-Y, Ramamurty U, Jang J. Influences of hydrogen charging method on the hydrogen distribution and nanomechanical properties of face-centered cubic high-entropy alloy: a comparative study. Scripta Mater 2019;168. https://doi.org/10.1016/j.scriptamat.2019.04.025.

[179] Wan D, Deng Y, Barnoush A. Hydrogen embrittlement effect observed by in-situ hydrogen plasma Chock for charging on a ferritic alloy. Scripta Mater 2018;151:24–7. <Go to ISI>://WOS:000432105100005.

[180] Wan D, Deng Y, Meling JIH, Alvaro A, Barnoush A. Hydrogen-enhanced fatigue crack growth in a single-edge notched tensile specimen under in-situ hydrogen charging inside an environmental scanning electron microscope. Acta Mater 2019;170:87–99. <Go to ISI>://WOS:000466252400008.

[181] Depover T, Wan D, Wang D, Barnoush A, Verbeken K. The effect of hydrogen on the crack initiation site of TRIP-assisted steels during in-situ hydrogen plasma micro-tensile testing: leading to an improved ductility? Mater Char 2020;167. <Go to ISI>://WOS:000558805700055.

[182] Asadipoor M, Anaraki AP, Kadkhodapour J, Sharifi SMH, Barnoush A. Macro- and microscale investigations of hydrogen embrittlement in X70 pipeline steel by in-situ and ex-situ hydrogen charging tensile tests and in-situ electrochemical micro-cantilever bending test. Mater Sci Eng A-Struc Mater Prop Microstruc Process 2020;772. <Go to ISI>://WOS:000509621500019.

[183] Hageman T, Martínez-Pañeda E. An electro-chemo-mechanical framework for predicting hydrogen uptake in metals due to aqueous electrolytes. Corrosion Sci 2022;208:110681. https://doi.org/10.1016/j.CORSCI.2022.110681.

[184] Suzuki H, Takai K. Summary of round-robin tests for standardizing hydrogen analysis procedures. ISIJ Int 2012;52. https://doi.org/10.2355/isijinternational.52.174.

[185] Kissinger HE. Reaction kinetics in differential thermal analysis. Anal Chem 1957;29. https://doi.org/10.1021/ac60131a045.

[186] Wipf H, editor. Hydrogen in metals III. Springer Berlin Heidelberg; 1997. https://doi.org/10.1007/BFb0103398.

[187] Burr PA, Murphy ST, Lumley SC, Wenman MR, Grimes RW. Hydrogen solubility in zirconium intermetallic second phase particles. J Nucl Mater 2013;443:502–6. https://doi.org/10.1016/J.JNUCMAT.2013.07.060.

[188] Tuli V, Claisse A, Burr PA. Hydrogen solubility in Zr-Nb alloys. Scripta Mater 2022;214:114652.

[189] Hirata K, Iikubo S, Koyama M, Tsuzaki K, Ohtani H. First-Principles study on hydrogen diffusivity in BCC, FCC, and HCP iron. Metall Mater Trans A Phys Metall Mater Sci 2018;49:5015–22. https://doi.org/10.1007/S11661-018-4815-9/FIGURES/10.

[190] Hagi H, Hayashi Y. Effect of dislocation trapping on hydrogen and deuterium diffusion in iron. Transac Japan Instit Metals 1987;28. https://doi.org/10.2320/matertrans1960.28.368.

[191] Kirchheim R, Pundt A. Hydrogen in metals. Phys Metallurg: Fifth Edition 2014;1:2597–705. https://doi.org/10.1016/B978-0-444-53770-6.00025-3.

[192] Chen Y-S, Haley D, Gerstl SSA, London AJ, Sweeney F, Wepf RA, Rainforth WM, Bagot PAJ, Moody MP. Direct observation of individual hydrogen atoms at trapping sites in a ferritic steel. Science (1979) 2017;355:1196–9. <Go to ISI>://WOS:000396351200041.

[193] Chen Y-S, Lu HZ, Liang JT, Rosenthal A, Liu HW, Sneddon G, McCarroll I, Zhao ZZ, Li W, Guo AM, Cairney JM. Observation of hydrogen trapping at dislocations, grain boundaries, and precipitates. Science (1979) 2020;367:171–5. <Go to ISI>://WOS:000506811300034.

[194] Takahashi J, Kawakami K, Kobayashi Y. Origin of hydrogen trapping site in vanadium carbide precipitation strengthening steel. Acta Mater 2018;153. https://doi.org/10.1016/j.actamat.2018.05.003.

[195] Young GA, Richey E, Morton DS. Hydrogen embrittlement in nuclear power systems, gaseous hydrogen embrittlement of materials in energy technologies: the problem. Its Char Eff Particular Alloy Classes 2012:149–76. https://doi.org/10.1533/9780857093899.1.149.

[196] Fernandez-Sousa R, Betegon C, Martinez-Paneda E. Analysis of the influence of microstructural traps on hydrogen assisted fatigue. Acta Mater 2020;199:253–63. <Go to ISI>://WOS:000577994500022.

[197] Flynn CP, Stoneham AM. Quantum theory of diffusion with application to light interstitials in metals. Phys Rev B 1970;1:3966. https://doi.org/10.1103/PhysRevB.1.3966.

[198] Stoneham AM, Flynn CP. On the quantum theory of isotope effects in the electromigration and thermomigration of light interstitials. J Phys F Met Phys 1973;3:505. https://doi.org/10.1088/0305-4608/3/3/008.

[199] Stoneham AM. Non- classical diffusion processes. J Nucl Mater 1978;69–70:109–16. https://doi.org/10.1016/0022-3115(78)90239-8.

[200] Schober HR, Stoneham AM. Motion of interstitials in metals: quantum tunneling at low temperatures. Phys Rev B 1982;26:1819. https://doi.org/10.1103/PhysRevB.26.1819.

[201] Kimizuka H, Mori H, Ogata S. Effect of temperature on fast hydrogen diffusion in iron: a path-integral quantum dynamics approach. Phys Rev B Condens Matter 2011;83:094110. https://doi.org/10.1103/PHYSREVB.83.094110/FIGURES/6/MEDIUM.

[202] Shuki N, Ryosuke M. Volumetric strain dependence of quantum diffusion of hydrogen in bcc iron. ISIJ Int 2021;61. https://doi.org/10.2355/ISIJINTERNATIONAL.ISIJINT-2020-340. ISIJINT-2020-340.

[203] Cheng B, Paxton AT, Ceriotti M. Hydrogen diffusion and trapping in α -iron: the role of quantum and anharmonic fluctuations. Phys Rev Lett 2018;120:225901. https://doi.org/10.1103/PHYSREVLETT.120.225901/FIGURES/3/MEDIUM.

[204] Turnbull A. Hydrogen diffusion and trapping in metals. In: Gaseous hydrogen embrittlement of materials in energy technologies. Elsevier; 2012. https://doi.org/10.1533/9780857095374.1.89.

[205] Shaw MJ, Briddon PR, Goss JP, Rayson MJ, Kerridge A, Harker AH, Stoneham AM. Erratum: importance of quantum tunneling in vacancy-hydrogen complexes in diamond. Phys Rev Lett 2005;95:219901. https://doi.org/10.1103/PhysRevLett.95.219901. Phys. Rev. Lett. 95, 105502 (2005).

[206] Kerridge A, Harker AH, Stoneham AM. Quantum behaviour of hydrogen and muonium in vacancy-containing complexes in diamond. J Phys Condens Matter 2004;16:8743. https://doi.org/10.1088/0953-8984/16/47/024.

[207] Paxton AT, Katzarov IH. Quantum and isotope effects on hydrogen diffusion, trapping and escape in iron. Acta Mater 2016;103. https://doi.org/10.1016/j.actamat.2015.09.054.

[208] Markland TE, Ceriotti M. Nuclear quantum effects enter the mainstream. Nat Rev Chem 2018 2018;2(2):1–14. https://doi.org/10.1038/s41570-017-0109. 3.

[209] Tuckerman M, Ceperley D. Preface: special topic on nuclear quantum effects. J Chem Phys 2018;148:102001. https://doi.org/10.1063/1.5026714.

[210] Svoboda J, Ecker W, Razumovskiy VI, Zickler GA, Fischer FD. Kinetics of interaction of impurity interstitials with dislocations revisited. Prog Mater Sci 2019;101. https://doi.org/10.1016/j.pmatsci.2018.10.001.

[211] Lejček P, Šob M, Paidar V. Interfacial segregation and grain boundary embrittlement: an overview and critical assessment of experimental data and calculated results. Prog Mater Sci 2017;87. https://doi.org/10.1016/j.pmatsci.2016.11.001.

[212] Pundt A, Kirchheim R. Hydrogen in metals: microstructural aspects. Annu Rev Mater Res 2006;36. https://doi.org/10.1146/annurev.matsci.36.090804.094451.

[213] Jiang DE, Carter EA. Diffusion of interstitial hydrogen into and through bcc Fe from first principles. Phys Rev B 2004;70:064102. https://doi.org/10.1103/PhysRevB.70.064102.

[214] Kawakami K, Matsumiya T. Numerical analysis of hydrogen trap state by TiC and V4C3 in bcc-Fe. ISIJ Int 2012;52. https://doi.org/10.2355/isijinternational.52.1693.

[215] Tateyama Y, Ohno T. Stability and clusterization of hydrogen-vacancy complexes in α-Fe: an ab-initio study. Phys Rev B 2003;67:174105. https://doi.org/10.1103/PhysRevB.67.174105.

[216] Ohsawa K, Eguchi K, Watanabe H, Yamaguchi M, Yagi M. Configuration and binding energy of multiple hydrogen atoms trapped in monovacancy in bcc transition metals. Phys Rev B Condens Matter 2012;85:094102. https://doi.org/10.1103/PHYSREVB.85.094102/FIGURES/8/MEDIUM.

[217] You YW, Kong XS, Wu XB, Xu YC, Fang QF, Chen JL, Luo GN, Liu CS, Pan BC, Wang Z. Dissolving, trapping and detrapping mechanisms of hydrogen in bcc and fcc transition metals. AIP Adv 2013;3:012118. https://doi.org/10.1063/1.4789547.

[218] Fullarton ML, Voskoboinikov RE, Middleburgh SC. Hydrogen accommodation in α-iron and nickel. J Alloys Compd 2014;587:794–9. https://doi.org/10.1016/J.JALLCOM.2013.10.169.

[219] Zhang P, Zhao J, Wen B. Vacancy trapping mechanism for multiple hydrogen and helium in beryllium: a first-principles study. J Phys Condens Matter 2012;24:095004. https://doi.org/10.1088/0953-8984/24/9/095004.

[220] Nordlander P, Norskov JK, Besenbacher F. Trends in hydrogen heats of solution and vacancy trapping energies in transition metals. J Phys F Met Phys 1986;16:1161. https://doi.org/10.1088/0305-4608/16/9/007.

[221] Counts WA, Wolverton C, Gibala R. First-principles energetics of hydrogen traps in α-Fe: point defects. Acta Mater 2010;58. https://doi.org/10.1016/j.actamat.2010.05.010.

[222] Samin AJ, Andersson DA, Holby EF, Uberuaga BP. First-principles localized cluster expansion study of the kinetics of hydrogen diffusion in homogeneous and heterogeneous Fe-Cr alloys. Phys Rev B 2019;99:014110. https://doi.org/10.1103/PHYSREVB.99.014110/FIGURES/11/MEDIUM.

[223] Du YA, Ismer L, Rogal J, Hickel T, Neugebauer J, Drautz R. First-principles study on the interaction of H interstitials with grain boundaries in <span class. Phys Rev B 2011;84:144121. https://doi.org/10.1103/PhysRevB.84.144121.

[224] Zhou X, Marchand D, McDowell DL, Zhu T, Song J. Chemomechanical origin of hydrogen trapping at grain boundaries in fcc metals. Phys Rev Lett 2016;116:075502. https://doi.org/10.1103/PhysRevLett.116.075502.

[225] Momida H, Asari Y, Nakamura Y, Tateyama Y, Ohno T. Hydrogen-enhanced vacancy embrittlement of grain boundaries in iron. Phys Rev B 2013;88:144107. https://doi.org/10.1103/PhysRevB.88.144107.

[226] Echeverri Restrepo S, di Stefano D, Mrovec M, Paxton AT. Density functional theory calculations of iron - vanadium carbide interfaces and the effect of hydrogen. Int J Hydrogen Energy 2020;45:2382–9. https://doi.org/10.1016/J.IJHYDENE.2019.11.102.

[227] Kawakami K, Matsumiya T. Ab-initio investigation of hydrogen trap state by cementite in bcc-Fe. ISIJ Int 2013;53:709–13. https://doi.org/10.2355/ISIJINTERNATIONAL.53.709.

[228] di Stefano D, Mrovec M, Elsässer C. First-principles investigation of hydrogen trapping and diffusion at grain boundaries in nickel. Acta Mater 2015;98. https://doi.org/10.1016/j.actamat.2015.07.031.

[229] Shi RJ, Ma Y, Wang ZD, Gao L, Yang XS, Qiao LJ, Pang XL. Atomic-scale investigation of deep hydrogen trapping in NbC/alpha-Fe semi-coherent interfaces. Acta Mater 2020;200:686–98. <Go to ISI>://WOS:000580631600059.

[230] Ma Y, Shi Y, Wang H, Mi Z, Liu Z, Gao L, Yan Y, Su Y, Qiao L. A first-principles study on the hydrogen trap characteristics of coherent nano-precipitates in α-Fe. Int J Hydrogen Energy 2020;45:27941–9. https://doi.org/10.1016/J.IJHYDENE.2020.07.123.

[231] Jones C, Tuli V, Shah Z, Gass M, Burr PA, Preuss M, Moore KL. Evidence of hydrogen trapping at second phase particles in zirconium alloys. Sci Rep 2021;11. https://doi.org/10.1038/s41598-021-83859-w.

[232] Burr PA, Murphy ST, Lumley SC, Wenman MR, Grimes RW. Hydrogen solubility in zirconium intermetallic second phase particles. J Nucl Mater 2013;443. https://doi.org/10.1016/j.jnucmat.2013.07.060.

[233] Burr PA, Murphy ST, Lumley SC, Wenman MR, Grimes RW. Hydrogen accommodation in Zr second phase particles: implications for H pick-up and hydriding of Zircaloy-2 and Zircaloy-4. Corrosion Sci 2013;69. https://doi.org/10.1016/j.corsci.2012.11.036.

[234] Zhang B, Su J, Wang M, Liu Z, Yang Z, Militzer M, Chen H. Atomistic insight into hydrogen trapping at MC/BCC-Fe phase boundaries: the role of local atomic environment. Acta Mater 2021;208:116744. https://doi.org/10.1016/J.ACTAMAT.2021.116744.

[235] Sadoc A, Majzoub EH, Huett VT, Kelton KF. Local structure in hydrogenated Ti–Zr–Ni quasicrystals and approximants. J Alloys Compd 2003;356–357:96–9. https://doi.org/10.1016/S0925-8388(02)01218-5.

[236] Radaković J, Batalović K, Maaревić I, Belošević-Čavor J. Interstitial hydrogen in Laves phases – local electronic structure modifications from first-principles. RSC Adv 2014;4:54769–74. https://doi.org/10.1039/C4RA09082A.

[237] Gesari SB, Pronsato ME, Visintin A, Juan A. Hydrogen storage in AB2 laves phase (A = Zr, Ti; B = Ni, Mn, Cr, V): binding energy and electronic structure. J Phys Chem C 2010;114:16832–6. https://doi.org/10.1021/JP106036V.

[238] Simpson EL, Paxton AT. Effect of applied strain on the interaction between hydrogen atoms and ½ ⟨111⟩ screw dislocations in α-iron. Int J Hydrogen Energy 2020;45:20069–79. https://doi.org/10.1016/J.IJHYDENE.2020.05.050.

[239] Smutna J, Wenman MR, Horsfield AP, Burr PA. The bonding of H in Zr under strain. J Nucl Mater 2023;573:154124. https://doi.org/10.1016/J.JNUCMAT.2022.154124.

[240] Phillpot SR, Antony AC, Shi L, Fullarton ML, Liang T, Sinnott SB, Zhang Y, Biner SB. Charge Optimized Many Body (COMB) potentials for simulation of nuclear fuel and clad. Comput Mater Sci 2018;148:231–41. https://doi.org/10.1016/J.COMMATSCI.2018.02.041.

[241] Senftle TP, Hong S, Islam MM, Kylasa SB, Zheng Y, Shin YK, Junkermeier C, Engel-Herbert R, Janik MJ, Aktulga HM, Verstraelen T, Grama A, van Duin ACT. The ReaxFF reactive force-field: development, applications and future directions. NPJ Comput Mater 2016;2(2):1–14. https://doi.org/10.1038/npjcompumats.2015.11. 1.

[242] Zubatiuk T, Isayev O. Development of multimodal machine learning potentials: toward a physics-aware artificial intelligence. Acc Chem Res 2021;54:1575–85. https://doi.org/10.1021/ACS.ACCOUNTS.0C00868.

[243] Behler J. Perspective: machine learning potentials for atomistic simulations. J Chem Phys 2016;145:170901. https://doi.org/10.1063/1.4966192.

[244] Mishin Y. Machine-learning interatomic potentials for materials science. Acta Mater 2021;214:116980. https://doi.org/10.1016/J.ACTAMAT.2021.116980.

[245] Lin H, Truhlar DG. QM/MM: what have we learned, where are we, and where do we go from here? Theor Chem Acc 2006 2006;117(117):185–99. https://doi.org/10.1007/S00214-006-0143-Z. 2.

[246] Zhao Y, Lu G. QM/MM study of dislocation—hydrogen/helium interactions in α-Fe. Model Simulat Mater Sci Eng 2011;19:065004. https://doi.org/10.1088/0965-0393/19/6/065004.

[247] Marx D, Parrinello M. Ab initio path integral molecular dynamics: basic ideas. J Chem Phys 1998;104:4077. https://doi.org/10.1063/1.471221.

[248] Marx D, Parrinello M. Ab initio path-integral molecular dynamics. Zeitschrift Für Physik B Condensed Matter 1994;95(95):143–4. https://doi.org/10.1007/BF01312185. 2.

[249] Ceriotti M, Bussi G, Parrinello M. Nuclear quantum effects in solids using a colored-noise thermostat. Phys Rev Lett 2009;103:030603. https://doi.org/10.1103/PHYSREVLETT.103.030603/FIGURES/3/MEDIUM.

[250] Ceriotti M, Manolopoulos DE, Parrinello M. Accelerating the convergence of path integral dynamics with a generalized Langevin equation. J Chem Phys 2011;134:084104. https://doi.org/10.1063/1.3556661.

[251] Ceriotti M, Manolopoulos DE. Efficient first-principles calculation of the quantum kinetic energy and momentum distribution of nuclei. Phys Rev Lett 2012;109:100604. https://doi.org/10.1103/PHYSREVLETT.109.100604/FIGURES/3/MEDIUM.

[252] Habershon S, Manolopoulos DE, Markland TE, Miller TF. Ring-polymer molecular dynamics: quantum effects in chemical dynamics from classical trajectories in an extended phase space, vol. 64; 2013. p. 387–413. https://doi.org/10.1146/ANNUREV-PHYSCHEM-040412-110122.

[253] Ceriotti M, More J, Manolopoulos DE. i-PI: a Python interface for ab initio path integral molecular dynamics simulations. Comput Phys Commun 2014;185:1019–26. https://doi.org/10.1016/J.CPC.2013.10.027.

[254] Geng HY. Accelerating ab initio path integral molecular dynamics with multilevel sampling of potential surface. J Comput Phys 2015;283:299–311. https://doi.org/10.1016/J.JCP.2014.12.007.

[255] Paxton AT, Katzarov IH. Quantum and isotope effects on hydrogen diffusion, trapping and escape in iron. Acta Mater 2016;103. https://doi.org/10.1016/j.actamat.2015.09.054.

[256] Hall MJW, Deckert DA, Wiseman HM. Quantum phenomena modeled by interactions between many classical worlds. Phys Rev X 2014;4:041013. https://doi.org/10.1103/PHYSREVX.4.041013/FIGURES/7/MEDIUM.

[257] Sturniolo S. Computational applications of the many-interacting-worlds interpretation of quantum mechanics. Phys Rev E 2018;97:053311. https://doi.org/10.1103/PHYSREVE.97.053311/FIGURES/7/MEDIUM.

[258] Nagano M, Hayashi Y, Ohtani N, Isshiki M, Igaki K. Hydrogen diffusivity in high purity alpha iron. Scripta Metall 1982;16:973–6. https://doi.org/10.1016/0036-9748(82)90136-3.

[259] Wei FG, Tsuzaki K. Quantitative analysis on hydrogen trapping of TiC particles in steel. Metall Mater Trans 2006;37. https://doi.org/10.1007/s11661-006-0004-3.

[260] Lin Y-C, McCarroll IE, Lin Y-T, Chung W-C, Cairney JM, Yen H-W. Hydrogen trapping and desorption of dual precipitates in tempered low-carbon martensitic steel. Acta Mater 2020;196. https://doi.org/10.1016/j.actamat.2020.06.046.

[261] Zafra A, Harris Z, Sun C, Martínez-Pañeda E. Comparison of hydrogen diffusivities measured by electrochemical permeation and temperature-programmed desorption in cold-rolled pure iron. J Nat Gas Sci Eng 2022;98:104365. https://doi.org/10.1016/J.JNGSE.2021.104365.

[262] Ai JH, Ha HM, Gangloff RP, Scully JR. Hydrogen diffusion and trapping in a precipitation-hardened nickel–copper–aluminum alloy Monel K-500 (UNS N05500). Acta Mater 2013;61:3186–99. https://doi.org/10.1016/J.ACTAMAT.2013.02.007.

[263] Pérez Escobar D, Duprez L, Atrens A, Verbeken K. Influence of experimental parameters on thermal desorption spectroscopy measurements during evaluation of hydrogen trapping. J Nucl Mater 2014;450:32–41. https://doi.org/10.1016/J.JNUCMAT.2013.07.006.

[264] Liu Q, Atrens A. Reversible hydrogen trapping in a 3.5NiCrMoV medium strength steel. Corrosion Sci 2015;96. https://doi.org/10.1016/j.corsci.2015.04.011.

[265] Liu Q, Venezuela J, Zhang M, Zhou Q, Atrens A. Hydrogen trapping in some advanced high strength steels. Corrosion Sci 2016;111. https://doi.org/10.1016/j.corsci.2016.05.046.

[266] de Graaf S, Momand J, Mitterbauer C, Lazar S, Kooi BJ. Resolving hydrogen atoms at metal-metal hydride interfaces. Sci Adv 2020;6. https://doi.org/10.1126/sciadv.aay4312.

[267] Ishikawa R, Okunishi E, Sawada H, Kondo Y, Hosokawa F, Abe E. Direct imaging of hydrogen-atom columns in a crystal by annular bright-field electron microscopy. Nat Mater 2011;10. https://doi.org/10.1038/nmat2957.

[268] Baldi A, Narayan TC, Koh AL, Dionne JA. In situ detection of hydrogen-induced phase transitions in individual palladium nanocrystals. Nat Mater 2014;13. https://doi.org/10.1038/nmat4086.

[269] Kim Y-J, Tao R, Klie RF, Seidman DN. Direct atomic-scale imaging of hydrogen and oxygen interstitials in pure niobium using atom-probe tomography and aberration-corrected scanning transmission electron microscopy. ACS Nano 2013;7. https://doi.org/10.1021/nn305029b.

[270] Redhead PA. Hydrogen in vacuum systems: an overview. In: AIP conf proc. AIP; 2003. https://doi.org/10.1063/1.1597372.

[271] Hong SS, Shin YH, Kim JT. Residual gas survey of stainless steel 304 extreme high vacuum chamber with hot cathode ionization gauge. Measurement 2008;41. https://doi.org/10.1016/j.measurement.2008.02.006.

[272] Gupta MK, Priyadarshi A, Khan Z. Hydrogen in stainless steel as killing agent for UHV: a review. Mater Today Proc 2015;2. https://doi.org/10.1016/j.matpr.2015.07.011.

[273] Sundell G, Thuvander M, Andrén H-O. Hydrogen analysis in APT: methods to control adsorption and dissociation of H2. Ultramicroscopy 2013;132. https://doi.org/10.1016/j.ultramic.2013.01.007.

[274] Stevie FA, Zhou C, Hopstaken M, Saccomanno M, Zhang Z, Turansky A. SIMS measurement of hydrogen and deuterium detection limits in silicon: comparison of different SIMS instrumentation. J Vacuum Sci & Technol B, Nanotechnol Microelectron: Mater, Process, Measurement, and Phenomena 2016;34. https://doi.org/10.1116/1.4940151.

[275] Arif M, Hussey DS, Jacobson DL. Neutron imaging for the hydrogen economy. https://doi.org/10.1007/978-0-387-78693-3_11; 2009.

[276] Griesche A, Dabah E, Kannengiesser T, Kardjilov N, Hilger A, Manke I. Three-dimensional imaging of hydrogen blister in iron with neutron tomography. Acta Mater 2014;78. https://doi.org/10.1016/j.actamat.2014.06.034.

[277] Duarte LI, Yetik O, Fagnoni F, Colldeweih A, Zubler R, Bertsch J, Trtik P. Neutron radiography imaging: a tool for determination of hydrogen distribution in unirradiated and irradiated fuel claddings. TopFuel2021 2021:6. https://www.dora.lib4ri.ch/psi/islandora/object/psi%3A40125/. [Accessed 13 June 2023].

[278] Li K, Liu J, Grovenor CRM, Moore KL. NanoSIMS imaging and analysis in materials science. Annu Rev Anal Chem 2020;13. https://doi.org/10.1146/annurev-anchem-092019-032524.

[279] Takahashi J, Kawakami K, Sakiyama Y, Ohmura T. Atomic-scale observation of hydrogen trap sites in bainite–austenite dual-phase steel by APT. Mater Char 2021;178. https://doi.org/10.1016/j.matchar.2021.111282.

[280] Takahashi J, Kawakami K, Tarui T. Direct observation of hydrogen-trapping sites in vanadium carbide precipitation steel by atom probe tomography. Scripta Mater 2012;67. https://doi.org/10.1016/j.scriptamat.2012.04.022.

[281] Takahashi J, Kawakami K, Kobayashi Y, Tarui T. The first direct observation of hydrogen trapping sites in TiC precipitation-hardening steel through atom probe tomography. Scripta Mater 2010;63. https://doi.org/10.1016/j.scriptamat.2010.03.012.

[282] Aboura Y, Martelo DF, Morana R, Akid R, Moore KL. Characterising hydrogen induced cracking of alloy 625+ using correlative SEM - EDX and NanoSIMS. Corrosion Sci 2021;181. https://doi.org/10.1016/j.corsci.2020.109228.

[283] Chen Y-S, Bagot PAJ, Moody MP, Haley D. Observing hydrogen in steel using cryogenic atom probe tomography: a simplified approach. Int J Hydrogen Energy 2019;44. https://doi.org/10.1016/j.ijhydene.2019.09.232.

[284] Chen Y-S, Haley D, Gerstl SSA, London AJ, Sweeney F, Wepf RA, Rainforth WM, Bagot PAJ, Moody MP. Direct observation of individual hydrogen atoms at trapping sites in a ferritic steel. Science (1979) 2017;355. https://doi.org/10.1126/science.aal2418.

[285] Aboura Y, Moore KL. NanoSIMS analysis of hydrogen and deuterium in metallic alloys: artefacts and best practice. Appl Surf Sci 2021;557:149736. https://doi.org/10.1016/J.APSUSC.2021.149736.

[286] McLennan KG, mac A Gray E. An equation of state for deuterium gas to 1000 bar. Meas Sci Technol 2003;15:211. https://doi.org/10.1088/0957-0233/15/1/029.

[287] Chen Y-S, Griffith MJ, Cairney JM. Cryo atom probe: freezing atoms in place for 3D mapping. Nano Today 2021;37. https://doi.org/10.1016/j.nantod.2021.101107.

[288] Chen Y-S, Liu P-Y, Niu R, Devaraj A, Yen H-W, Marceau RKW, Cairney JM. Atom probe tomography for the observation of hydrogen in materials: a review. Microsc Microanal 2023;29:1–15. https://doi.org/10.1093/MICMIC/OZAC005.

[289] Zhao H, Chakraborty P, Ponge D, Hickel T, Sun B, Wu CH, Gault B, Raabe D. Hydrogen trapping and embrittlement in high-strength Al alloys. Nature 2022:437–41. https://doi.org/10.1038/s41586-021-04343-z. 2022 602:7897. 602.

[290] Nishimoto A, Koyama M, Yamato S, Oda Y, Awane T, Noguchi H. Detection of charged hydrogen in ferritic steel through cryogenic secondary ion mass spectrometry. ISIJ Int 2015;55:335–7. <Go to ISI>://WOS:000348554500040.

[291] Li K, Aarholt T, Liu J, Hulme H, Garner A, Preuss M, Lozano-Perez S, Grovenor C. 3D-characterization of deuterium distributions in zirconium oxide scale using high-resolution SIMS. Appl Surf Sci 2019;464:311–20. https://doi.org/10.1016/J.APSUSC.2018.09.101.

[292] Tarzimoghadam Z, Rohwerder M, Merzlikin Sv, Bashir A, Yedra L, Eswara S, Ponge D, Raabe D. Multi-scale and spatially resolved hydrogen mapping in a Ni–Nb model alloy reveals the role of the δ phase in hydrogen embrittlement of alloy 718. Acta Mater 2016;109:69–81. https://doi.org/10.1016/J.ACTAMAT.2016.02.053.

[293] Zhang Z, Moore KL, McMahon G, Morana R, Preuss M. On the role of precipitates in hydrogen trapping and hydrogen embrittlement of a nickel-based superalloy. Corrosion Sci 2019;146:58–69. https://doi.org/10.1016/J.CORSCI.2018.10.019.

[294] Qin W, Thomas A, Cheng ZQ, Gu D, Li TL, Zhu WL, Szpunar JA. Key factors affecting hydrogen trapping at the inclusions in steels: a combined study using microprint technique and theoretical modeling. Corrosion Sci 2022;200:110239. https://doi.org/10.1016/J.CORSCI.2022.110239.

[295] Thomas A, Szpunar JA. Hydrogen diffusion and trapping in X70 pipeline steel. Int J Hydrogen Energy 2020;45:2390–404. https://doi.org/10.1016/J.IJHYDENE.2019.11.096.

[296] Ovejero-García J. Hydrogen microprint technique in the study of hydrogen in steels. J Mater Sci 1985;20:2623–9. https://doi.org/10.1007/BF00556094/METRICS.

[297] Zhang B, Zhu Q, Xu C, Li C, Ma Y, Ma Z, Liu S, Shao R, Xu Y, Jiang B, Gao L, Pang X, He Y, Chen G, Qiao L. Atomic-scale insights on hydrogen trapping and exclusion at incoherent interfaces of nanoprecipitates in martensitic steels. Nat Commun 2022 2022;13(13):1–11. https://doi.org/10.1038/s41467-022-31665-x. 1.

[298] Wang G, Yan Y, Yang X, Li J, Qiao L. Investigation of hydrogen evolution and enrichment by scanning Kelvin probe force microscopy. Electrochem Commun 2013;35:100–3. https://doi.org/10.1016/J.ELECOM.2013.08.006.

[299] Schaller RF, Scully JR. Measurement of effective hydrogen diffusivity using the Scanning Kelvin Probe. Electrochem Commun 2014;40:42–4. https://doi.org/10.1016/J.ELECOM.2013.12.025.

[300] Au JJ, Birnbaum HK. Magnetic relaxation studies of the motion of hydrogen and deuterium in iron. Acta Metall 1978;26. https://doi.org/10.1016/0001-6160(78)90138-4.

[301] Myers SM, Picraux ST, Stoltz RE. Defect trapping of ion-implanted deuterium in Fe. J Appl Phys 1979;50. https://doi.org/10.1063/1.326761.

[302] Kim K-B, Pyun S-I. The effect of vacancies on hydrogen diffusivity and solubility in pure iron at room temperature. Arch für das Eisenhuttenwes 1982;53. https://doi.org/10.1002/srin.198205414.

[303] Kim K-T, Pyun S-I, Riecke EM. Vacancies as hydrogen trap sites in iron. J Mater Sci Lett 1985;4. https://doi.org/10.1007/BF00720050.

[304] Paxton AT. From quantum mechanics to physical metallurgy of steels. Mater Sci Technol 2014;30. https://doi.org/10.1179/1743284714Y.0000000521.

[305] Lee JL, Lee JY. Hydrogen trapping in AISI 4340 steel. Met Sci 1983;17. https://doi.org/10.1179/030634583790420619.

[306] Kumnick AJ, Johnson HH. Deep trapping states for hydrogen in deformed iron. Acta Metall 1980;28. https://doi.org/10.1016/0001-6160(80)90038-3.

[307] Takai K, Homma Y, Izutsu K, Nagumo M. Identification of trapping sites in high-strength steels by secondary ion mass spectrometry for thermally desorbed hydrogen. J Jpn Inst Metals 1996;60. https://doi.org/10.2320/jinstmet1952.60.12_1155.

[308] Choo WY, Lee JY. Thermal analysis of trapped hydrogen in pure iron. Metall Trans A 1982;13. https://doi.org/10.1007/BF02642424.

[309] Bernstein IM. The effect of hydrogen on the deformation of iron. Scripta Metall 1974;8. https://doi.org/10.1016/0036-9748(74)90136-7.

[310] Ono K, Meshii M. Hydrogen detrapping from grain boundaries and dislocations in high purity iron. Acta Metall Mater 1992;40. https://doi.org/10.1016/0956-7151(92)90436-I.

[311] Lin Y-C, Chen D, Chiang M-H, Cheng G-J, Lin H-C, Yen H-W. Response of hydrogen desorption and hydrogen embrittlement to precipitation of nanometer-sized copper in tempered martensitic low-carbon steel. JOM (J Occup Med) 2019;71. https://doi.org/10.1007/s11837-019-03330-0.

[312] Parvathavarthini N, Saroja S, Dayal RK, Khatak HS. Studies on hydrogen permeability of 2.25% Cr–1% Mo ferritic steel: correlation with microstructure. J Nucl Mater 2001;288. https://doi.org/10.1016/S0022-3115(00)00706-6.

[313] Lee HG, Lee J-Y. Hydrogen trapping by TiC particles in iron. Acta Metall 1984;32. https://doi.org/10.1016/0001-6160(84)90210-4.

[314] Pressouyre GM, Bernstein IM. A quantitative analysis of hydrogen trapping. Metall Trans A 1978;9. https://doi.org/10.1007/BF02661939.

[315] Asaoka T, Lapasset G, Aucouturier M, Lacombe P. Observation of hydrogen trapping in Fe-0.15 Wt% Ti alloy by high resolution autoradiography. Corrosion 1978;34. https://doi.org/10.5006/0010-9312-34.2.39.

[316] Pérez Escobar D, Wallaert E, Duprez L, Atrens A, Verbeken K. Thermal desorption spectroscopy study of the interaction of hydrogen with TiC precipitates. Met Mater Int 2013;19. https://doi.org/10.1007/s12540-013-4013-7.

[317] Lin Y-T, Yi HL, Chang ZY, Lin H-C, Yen H-W. Role of vanadium carbide in hydrogen embrittlement of press-hardened steels: strategy from 1500 to 2000 MPa. Front Mater 2021;7. https://doi.org/10.3389/fmats.2020.611390.

[318] Asahi H, Hirakami D, Yamasaki S. Hydrogen trapping behavior in vanadium-added steel. ISIJ Int 2003;43. https://doi.org/10.2355/isijinternational.43.527.

[319] Yamasaki S, Takahashi T. Evaluation method of delayed fracture property of high strength steels. Tetsu-To-Hagane 1997;83. https://doi.org/10.2355/tetsutohagane1955.83.7_454.

[320] Wallaert E, Depover T, Arafin M, Verbeken K. Thermal desorption spectroscopy evaluation of the hydrogen-trapping capacity of NbC and NbN precipitates. Metall Mater Trans 2014;45. https://doi.org/10.1007/s11661-013-2181-1.

[321] Wei F-G, Tsuzaki K. Hydrogen trapping character of nano-sized NbC precipitates in tempered martensite. In: Proceedings of the 2008 international hydrogen conference - effects of hydrogen on materials; 2009. p. 456–63.

[322] Thomas RLS, Li D, Gangloff RP, Scully JR. Trap-governed hydrogen diffusivity and uptake capacity in ultrahigh-strength AERMET 100 steel. Metall Mater Trans 2002;33. https://doi.org/10.1007/s11661-002-0032-6.

[323] Hinotani S, Ohmori Y, Terasaki F. Effects of Fe3C and Mo2C precipitation on hydrogen diffusivity and hydrogen embrittlement in iron alloys. Mater Sci Eng 1985;76. https://doi.org/10.1016/0025-5416(85)90080-1.

[324] Depover T, Verbeken K. Evaluation of the role of Mo2C in hydrogen induced ductility loss in Q&T Fe C Mo alloys. Int J Hydrogen Energy 2016;41. https://doi.org/10.1016/j.ijhydene.2016.05.176.

[325] Wei FG, Tsuzaki K. Response of hydrogen trapping capability to microstructural change in tempered F-0.2C martensite. Scripta Mater 2005;52:467–72.

[326] Hong G-W, Lee J-Y. The interaction of hydrogen and the cementite-ferrite interface in carbon steel. J Mater Sci 1983;18. https://doi.org/10.1007/BF00543835.

[327] Hsu Y-T, Jiang H-Y, Yen H-W, Lin H-C, Hong S. Hydrogen-induced embrittlement of nickel-chromium-molybdenum containing HSLA steels. J Chin Inst Eng 2020; 43. https://doi.org/10.1080/02533839.2019.1676659.

[328] Serra E, Perujo A, Benamati G. Influence of traps on the deuterium behaviour in the low activation martensitic steels F82H and Batman. J Nucl Mater 1997;245. https://doi.org/10.1016/S0022-3115(97)00021-4.

[329] Huang GY, Hu X, Wirth BD. First-principles investigations of hydrogen trapping in Y2O3 and the Y2O3|bcc Fe interface. J Phys Condens Matter 2020;32:495001. https://doi.org/10.1088/1361-648X/ABB17E.

[330] Esteban GA, Peña A, Legarda F, Lindau R. Hydrogen transport and trapping in ODS-EUROFER. Fusion Eng Des 2007;82:2634–40. https://doi.org/10.1016/J.FUSENGDES.2007.02.002.

[331] Turnbull A, Hutchings RB. Analysis of hydrogen atom transport in a two-phase alloy. Mater Sci Eng, A 1994;177. https://doi.org/10.1016/0921-5093(94)90488-X.

[332] Lee KY, Lee J-Y, Kim DR. A study of hydrogen-trapping phenomena in AISI 5160 spring steel. Mater Sci Eng 1984;67. https://doi.org/10.1016/0025-5416(84)90053-3.

[333] Lee J-L, Lee J-Y. The interaction of hydrogen with the interface of Al2O3 particles in iron. Metall Trans A 1986;17. https://doi.org/10.1007/BF02645916.

[334] Li Y, Wang Q, Zhang H, Zhu H, Wang M, Wang H. Role of solute atoms and vacancy in hydrogen embrittlement mechanism of aluminum: a first-principles study. Int J Hydrogen Energy 2023;48:4516–28. https://doi.org/10.1016/J.IJHYDENE.2022.10.257.

[335] Polfus JM, Løvvik OM, Bredesen R, Peters T. Hydrogen induced vacancy clustering and void formation mechanisms at grain boundaries in palladium. Acta Mater 2020;195. https://doi.org/10.1016/j.actamat.2020.06.007.

[336] Qin S-Y, Jin S, Sun L, Zhou H-B, Zhang Y, Lu G-H. Hydrogen assisted vacancy formation in tungsten: a first-principles investigation. J Nucl Mater 2015;465. https://doi.org/10.1016/j.jnucmat.2015.05.040.

[337] Varvenne C, Mackain O, Proville L, Clouet E. Hydrogen and vacancy clustering in zirconium. Acta Mater 2016;102. https://doi.org/10.1016/j.actamat.2015.09.019.

[338] Chiari L, Kojima K, Endo Y, Teshigahara H, Butterling M, Liedke MO, Hirschmann E, Attallah AG, Wagner A, Fujinami M. Formation and time dynamics of hydrogen-induced vacancies in nickel. Acta Mater 2021;219. https://doi.org/10.1016/j.actamat.2021.117264.

[339] Fernandez N, Ferro Y, Kato D. Hydrogen diffusion and vacancies formation in tungsten: density Functional Theory calculations and statistical models. Acta Mater 2015;94. https://doi.org/10.1016/j.actamat.2015.04.052.

[340] Carr NZ, McLellan RB. The thermodynamic and kinetic behavior of metal–vacancy–hydrogen systems. Acta Mater 2004;52. https://doi.org/10.1016/j.actamat.2004.03.024.

[341] Fukai Y. Formation of superabundant vacancies in M–H alloys and some of its consequences: a review. J Alloys Compd 2003;356–357. https://doi.org/10.1016/S0925-8388(02)01269-0.

[342] Xie D, Li S, Li M, Wang Z, Gumbsch P, Sun J, Ma E, Li J, Shan Z. Hydrogenated vacancies lock dislocations in aluminium. Nat Commun 2016;7. https://doi.org/10.1038/ncomms13341.

[343] Itakura M, Kaburaki H, Yamaguchi M, Okita T. The effect of hydrogen atoms on the screw dislocation mobility in bcc iron: a first-principles study. Acta Mater 2013;61. https://doi.org/10.1016/j.actamat.2013.07.064.

[344] Yu P, Cui YG, Zhu GZ, Shen Y, Wen M. The key role played by dislocation core radius and energy in hydrogen interaction with dislocations. Acta Mater 2020; 185:518–27. <Go to ISI>://WOS:000514747400045.

[345] Dadfarnia M, Martin ML, Nagao A, Sofronis P, Robertson IM. Modeling hydrogen transport by dislocations. J Mech Phys Solid 2015;78. https://doi.org/10.1016/j.jmps.2015.03.002.

[346] Chêne J, Brass AM. Hydrogen transport by mobile dislocations in nickel base superalloy single crystals. Scripta Mater 1999;40. https://doi.org/10.1016/S1359-6462(98)00451-5.

[347] Itoh G, Koyama K, Kanno M. Evidence for the transport of impurity hydrogen with gliding dislocations in aluminum. Scripta Mater 1996;35. https://doi.org/10.1016/1359-6462(96)00200-X.

[348] Koyama M, Taheri-Mousavi SM, Yan H, Kim J, Cameron BC, Moeini-Ardakani SS, Li J, Tasan CC. Origin of micrometer-scale dislocation motion during hydrogen desorption. Sci Adv 2020;6. https://doi.org/10.1126/sciadv.aaz1187.

[349] Martin ML, Dadfarnia M, Nagao A, Wang S, Sofronis P. Enumeration of the hydrogen-enhanced localized plasticity mechanism for hydrogen embrittlement in structural materials. Acta Mater 2019;165. https://doi.org/10.1016/j.actamat.2018.12.014.

[350] Ogawa Y, Noguchi K, Takakuwa O. Criteria for hydrogen-assisted crack initiation in Ni-based superalloy 718. Acta Mater 2022;229:117789. https://doi.org/10.1016/J.ACTAMAT.2022.117789.

[351] Oudriss A, Creus J, Bouhattate J, Savall C, Peraudeau B, Feaugas X. The diffusion and trapping of hydrogen along the grain boundaries in polycrystalline nickel. Scripta Mater 2012;66. https://doi.org/10.1016/j.scriptamat.2011.09.036.

[352] He Y, Su Y, Yu H, Chen C. First-principles study of hydrogen trapping and diffusion at grain boundaries in γ-Fe. Int J Hydrogen Energy 2021;46. https://doi.org/10.1016/j.ijhydene.2020.11.238.

[353] Li Q, Mo JW, Ma SH, Duan FH, Zhao YL, Liu SF, Liu WH, Zhao SJ, Liu CT, Liaw PK, Yang T. Defeating hydrogen-induced grain-boundary embrittlement via triggering unusual interfacial segregation in FeCrCoNi-type high-entropy alloys. Acta Mater 2022;241:118410. https://doi.org/10.1016/J.ACTAMAT.2022.118410.

[354] Koyama M, Bashir A, Rohwerder M, Merzlikin Sv, Akiyama E, Tsuzaki K, Raabe D. Spatially and kinetically resolved mapping of hydrogen in a twinning-induced plasticity steel by use of scanning Kelvin probe force microscopy. J Electrochem Soc 2015;162. https://doi.org/10.1149/2.0131512jes.

[355] Raabe D, Sun B, Kwiatkowski Da Silva A, Gault B, Yen H-W, Sedighiani K, Thoudden Sukumar P, Souza Filho IR, Katnagallu S, Jägle E, Kürnsteiner P, Kusampudi N, Stephenson L, Herbig M, Liebscher CH, Springer H, Zaefferer S, Shah V, Wong S-L, Baron C, Diehl M, Roters F, Ponge D. Current challenges and opportunities in microstructure-related properties of advanced high-strength steels. Metall Mater Trans 2020;51. https://doi.org/10.1007/s11661-020-05947-2.

[356] Yen H-W, Chen P-Y, Huang C-Y, Yang J-R. Interphase precipitation of nanometer-sized carbides in a titanium–molybdenum-bearing low-carbon steel. Acta Mater 2011;59. https://doi.org/10.1016/j.actamat.2011.06.037.

[357] Chen M-Y, Gouné M, Verdier M, Bréchet Y, Yang J-R. Interphase precipitation in vanadium-alloyed steels: strengthening contribution and morphological variability with austenite to ferrite transformation. Acta Mater 2014;64. https://doi.org/10.1016/j.actamat.2013.11.025.

[358] Gong P, Palmiere EJ, Rainforth WM. Dissolution and precipitation behaviour in steels microalloyed with niobium during thermomechanical processing. Acta Mater 2015;97. https://doi.org/10.1016/j.actamat.2015.06.057.

[359] Gong P, Liu XG, Rijkenberg A, Rainforth WM. The effect of molybdenum on interphase precipitation and microstructures in microalloyed steels containing titanium and vanadium. Acta Mater 2018;161. https://doi.org/10.1016/j.actamat.2018.09.008.

[360] Shi R, Ma Y, Wang Z, Gao L, Yang XS, Qiao L, Pang X. Atomic-scale investigation of deep hydrogen trapping in NbC/α-Fe semi-coherent interfaces. Acta Mater 2020;200:686–98. https://doi.org/10.1016/J.ACTAMAT.2020.09.031.

[361] di Stefano D, Nazarov R, Hickel T, Neugebauer J, Mrovec M, Elsässer C. First-principles investigation of hydrogen interaction with TiC precipitates in α -Fe. Phys Rev B 2016;93. https://doi.org/10.1103/PhysRevB.93.184108.

[362] Fang J, Xu C, Li Y, Peng R, Fu X. Effect of grain orientation and interface coherency on the hydrogen trapping ability of TiC precipitates in a ferritic steel. Mater Lett 2022;308:131281. https://doi.org/10.1016/J.MATLET.2021.131281.

[363] Breen AJ, Stephenson LT, Sun B, Li Y, Kasian O, Raabe D, Herbig M, Gault B. Solute hydrogen and deuterium observed at the near atomic scale in high-strength steel. Acta Mater 2020;188. https://doi.org/10.1016/j.actamat.2020.02.004.

[364] Yu SH, Lee SM, Lee S, Nam JH, Lee JS, Bae CM, Lee YK. Effects of lamellar structure on tensile properties and resistance to hydrogen embrittlement of pearlitic steel. Acta Mater 2019;172:92–101. https://doi.org/10.1016/J.ACTAMAT.2019.04.040.

[365] Okuno K, Takai K. Determination of hydrogen diffusibility and embrittlement susceptibility of high-strength steel evaluated at different temperatures based on the local equilibrium theory. Acta Mater 2023;246:118725. https://doi.org/10.1016/J.ACTAMAT.2023.118725.

[366] Lin Y-C, McCarroll IE, Lin Y-T, Chung W-C, Cairney JM, Yen H-W. Hydrogen trapping and desorption of dual precipitates in tempered low-carbon martensitic steel. Acta Mater 2020;196. https://doi.org/10.1016/j.actamat.2020.06.046.

[367] Yaguchi H, Kochi T, Nomura M, Watanabe T. Hydrogen trapping behavior of copper precipitates in steel. J Jpn Inst Metals 2007;71. https://doi.org/10.2320/jinstmet.71.781.

[368] Sun H, Lv W, Yang Y, Li D, Yan L, Pang X, He Y, Gao K. Optimizing the hydrogen embrittlement resistance by tuning the structures of Cu-rich nanoprecipitates in high strength martensite stainless steels. Acta Mater 2023;246:118722. https://doi.org/10.1016/J.ACTAMAT.2023.118722.

ARTICLE IN PRESS

Y.-S. Chen et al.   International Journal of Hydrogen Energy xxx (xxxx) xxx

[369] Xing W, Chen X-Q, Liu P, Wang X, Zhang P, Li D, Li Y. First-principles studies of hydrogen behavior interacting with oxygen-enriched nanostructured particles in the ODS steels. Int J Hydrogen Energy 2014;39. https://doi.org/10.1016/j.ijhydene.2014.09.036.

[370] Guedes D, Malheiros LC, Oudriss A, Cohendoz S, Bouhattate J, Creus J, Thebault F, Piette M, Feaugas X. The role of plasticity and hydrogen flux in the fracture of a tempered martensitic steel: a new design of mechanical test until fracture to separate the influence of mobile from deeply trapped hydrogen. Acta Mater 2020;186:133–48. <Go to ISI>://WOS:000518698300013.

[371] Elboujdaini M, Revie RW. Metallurgical factors in stress corrosion cracking (SCC) and hydrogen-induced cracking (HIC). J Solid State Electrochem 2009;13:1091–9. <Go to ISI>://WOS:000265307100014.

[372] Rahman KMM, Mohtadi-Bonab MA, Ouellet R, Szpunar J, Zhu N. Effect of electrochemical hydrogen charging on an API X70 pipeline steel with focus on characterization of inclusions. Int J Pres Ves Pip 2019;173:147–55. <Go to ISI>://WOS:000471731800013.

[373] Otsuka T, Tanabe T. Hydrogen diffusion and trapping process around MnS precipitates in αFe examined by tritium autoradiography. J Alloys Compd 2007;446–447. https://doi.org/10.1016/j.jallcom.2007.02.005.

[374] Peng Z, Liu J, Huang F, Hu Q, Cheng Z, Liu S, Cheng Y. Effect of submicron-scale MnS inclusions on hydrogen trapping and HIC susceptibility of X70 pipeline steels. Steel Res Int 2018;89. https://doi.org/10.1002/srin.201700566.

[375] Li W, Zhu X, Yao J, Jin X, Ding X. Hydrogen traps and hydrogen induced cracking in 20CrMo steel. ISIJ Int 2017;57. https://doi.org/10.2355/isijinternational.ISIJINT-2016-281.

[376] Sekine D, Sakiyama Y, Omura T, Takai K. Dependence of trapping states on the hydrogen content of high-carbon ferrite-austenite dual-phase steel. IOP Conf Ser Mater Sci Eng 2018;461. https://doi.org/10.1088/1757-899X/461/1/012076.

[377] Zhu X, Li W, Zhao H, Wang L, Jin X. Hydrogen trapping sites and hydrogen-induced cracking in high strength quenching & partitioning (Q& P) treated steel. Int J Hydrogen Energy 2014;39. https://doi.org/10.1016/j.ijhydene.2014.06.079.

[378] Ryu JH, Chun YS, Lee CS, Bhadeshia HKDH, Suh DW. Effect of deformation on hydrogen trapping and effusion in TRIP-assisted steel. Acta Mater 2012;60. https://doi.org/10.1016/j.actamat.2012.04.010.

[379] Wu K, Lu X, Zhou P, Li W, Jin X. Improved resistance to hydrogen embrittlement by tailoring the stability of retained austenite. Mater Sci Technol 2017;33. https://doi.org/10.1080/02670836.2017.1280119.

[380] Pinson M, Springer H, Depover T, Verbeken K. The effect of quench cracks and retained austenite on the hydrogen trapping capacity of high carbon martensitic steels. Int J Hydrogen Energy 2021;46. https://doi.org/10.1016/j.ijhydene.2021.02.057.

[381] Chan SLI, Lee HL, Yang JR. Effect of retained austenite on the hydrogen content and effective diffusivity of martensitic structure. Metall Trans A 1991;22. https://doi.org/10.1007/BF02851351.

[382] Cota AB, Ooi SW, Solano-Alvarez W, Bhadeshia HKDH. Infusion of hydrogen into nanostructured bainitic steel. Mater Char 2017;134:96–102. https://doi.org/10.1016/J.MATCHAR.2017.10.006.

[383] Bouaziz O, Allain S, Scott CP, Cugy P, Barbier D. High manganese austenitic twinning induced plasticity steels: a review of the microstructure properties relationships. Curr Opin Solid State Mater Sci 2011;15. https://doi.org/10.1016/j.cossms.2011.04.002.

[384] Hempel N, Mandel M, Schröder C, Quitzke C, Schimpf C, Wendler M, Volkova O, Krüger L. Influence of microstructure on hydrogen trapping and diffusion in a pre-deformed TRIP steel. Int J Hydrogen Energy 2023;48:4906–20. https://doi.org/10.1016/J.IJHYDENE.2022.11.017.

[385] Wu K, Lu X, Zhou P, Li W, Jin X. Improved resistance to hydrogen embrittlement by tailoring the stability of retained austenite. Mater Sci Technol 2017;33. https://doi.org/10.1080/02670836.2017.1280119.

[386] Laureys A, Pinson M, Depover T, Petrov R, Verbeken K. EBSD characterization of hydrogen induced blisters and internal cracks in TRIP-assisted steel. Mater Char 2020;159:110029. https://doi.org/10.1016/J.MATCHAR.2019.110029.

[387] Silverstein R, Eliezer D, Tal-Gutelmacher E. Hydrogen trapping in alloys studied by thermal desorption spectrometry. J Alloys Compd 2018;747. https://doi.org/10.1016/j.jallcom.2018.03.066.

[388] Yan F, Mouton I, Stephenson LT, Breen AJ, Chang Y, Ponge D, Raabe D, Gault B. Atomic-scale investigation of hydrogen distribution in a Ti Mo alloy. Scripta Mater 2019;162. https://doi.org/10.1016/j.scriptamat.2018.11.040.

[389] Breen AJ, Mouton I, Lu W, Wang S, Szczepaniak A, Kontis P, Stephenson LT, Chang Y, da Silva AK, Liebscher CH, Raabe D, Britton TB, Herbig M, Gault B. Atomic scale analysis of grain boundary deuteride growth front in Zircaloy-4. Scripta Mater 2018;156. https://doi.org/10.1016/j.scriptamat.2018.06.044.

[390] Dadfarnia M, Sofronis P, Neeraj T. Hydrogen interaction with multiple traps: can it be used to mitigate embrittlement? Int J Hydrogen Energy 2011;36:10141–8. https://doi.org/10.1016/J.IJHYDENE.2011.05.027.

[391] Wei FG, Tsuzaki K. Hydrogen trapping phenomena in martensitic steels, gaseous hydrogen embrittlement of materials in energy technologies: the problem. Its Char Eff Particular Alloy Classes 2012:493–525. https://doi.org/10.1533/9780857093899.3.493.

[392] Chen S, Zhao M, Rong L. Effect of grain size on the hydrogen embrittlement sensitivity of a precipitation strengthened Fe–Ni based alloy. Mater Sci Eng 2014;594:98–102. https://doi.org/10.1016/J.MSEA.2013.11.062.

[393] Park C, Kang N, Liu S. Effect of grain size on the resistance to hydrogen embrittlement of API 2W Grade 60 steels using in situ slow-strain-rate testing. Corrosion Sci 2017;128:33–41. https://doi.org/10.1016/J.CORSCI.2017.08.032.

[394] Gomes da Silva MJ, Cardoso JL, Carvalho DS, Santos LPM, Herculano LFG, Gomes de Abreu HF, Pardal JM. The effect of prior austenite grain size on hydrogen embrittlement of Co-containing 18Ni 300 maraging steel. Int J Hydrogen Energy 2019;44:18606–15. https://doi.org/10.1016/J.IJHYDENE.2019.05.074.

[395] Macadre A, Nakada N, Tsuchiyama T, Takaki S. Critical grain size to limit the hydrogen-induced ductility drop in a metastable austenitic steel. Int J Hydrogen Energy 2015;40:10697–703. https://doi.org/10.1016/J.IJHYDENE.2015.06.111.

[396] Fan YH, Zhang B, Wang JQ, Han EH, Ke W. Effect of grain refinement on the hydrogen embrittlement of 304 austenitic stainless steel. J Mater Sci Technol 2019;35:2213–9. https://doi.org/10.1016/J.JMST.2019.03.043.

[397] Noh HS, Kang JH, Kim SJ. Effect of grain size on hydrogen embrittlement in stable austenitic high-Mn TWIP and high-N stainless steels. Int J Hydrogen Energy 2019;44:25076–90. https://doi.org/10.1016/J.IJHYDENE.2019.07.227.

[398] Park IJ, min Lee S, hee Jeon H, Lee YK. The advantage of grain refinement in the hydrogen embrittlement of Fe–18Mn–0.6C twinning-induced plasticity steel. Corrosion Sci 2015;93:63–9. https://doi.org/10.1016/J.CORSCI.2015.01.012.

[399] Zan N, Ding H, Guo X, Tang Z, Bleck W. Effects of grain size on hydrogen embrittlement in a Fe-22Mn-0.6C TWIP steel. Int J Hydrogen Energy 2015;40:10687–96. https://doi.org/10.1016/J.IJHYDENE.2015.06.112.

[400] Bai Y, Momotani Y, Chen MC, Shibata A, Tsuji N. Effect of grain refinement on hydrogen embrittlement behaviors of high-Mn TWIP steel. Mater Sci Eng, A 2016;651:935–44. https://doi.org/10.1016/J.MSEA.2015.11.017.

[401] Lawrence SK, Yagodzinskyy Y, Hänninen H, Korhonen E, Tuomisto F, Harris ZD, Somerday BP. Effects of grain size and deformation temperature on hydrogen-enhanced vacancy formation in Ni alloys. Acta Mater 2017;128:218–26. https://doi.org/10.1016/J.ACTAMAT.2017.02.016.

[402] Koyama M, Ichii K, Tsuzaki K. Grain refinement effect on hydrogen embrittlement resistance of an equiatomic CoCrFeMnNi high-entropy alloy. Int J Hydrogen Energy 2019;44:17163–7. https://doi.org/10.1016/J.IJHYDENE.2019.04.280.

[403] Wang H, Koyama M, Hojo T, Akiyama E. Hydrogen embrittlement and associated surface crack growth in fine-grained equiatomic CoCrFeMnNi high-entropy alloys with different annealing temperatures evaluated by tensile testing under in situ hydrogen charging. Int J Hydrogen Energy 2021;46:33028–38. https://doi.org/10.1016/J.IJHYDENE.2021.07.136.

[404] Zhou XY, Yang XS, Zhu JH, Xing F. Atomistic simulation study of the grain-size effect on hydrogen embrittlement of nanograined Fe. Int J Hydrogen Energy 2020;45:3294–306. https://doi.org/10.1016/J.IJHYDENE.2019.11.131.

[405] Song SW, Lee T, Lee CS. Graded grain structure to improve hydrogen-embrittlement resistance of TWIP steel. Crystals 2020;10:1045. https://doi.org/10.3390/CRYST10111045. 2020, Vol. 10, Page 1045.

[406] Fang TH, Li WL, Tao NR, Lu K. Revealing extraordinary intrinsic tensile plasticity in gradient nano-grained copper. Science (1979) 2011;331:1587–90. https://doi.org/10.1126/SCIENCE.1200177/SUPPL_FILE/PAP.PDF.

[407] Depover T, Verbeken K. The detrimental effect of hydrogen at dislocations on the hydrogen embrittlement susceptibility of Fe-C-X alloys: an experimental proof of the HELP mechanism. Int J Hydrogen Energy 2018;43:3050–61. https://doi.org/10.1016/J.IJHYDENE.2017.12.109.

[408] Chen L, Xiong X, Tao X, Su Y, Qiao L. Effect of dislocation cell walls on hydrogen adsorption, hydrogen trapping and hydrogen embrittlement resistance. Corrosion Sci 2020;166:108428. https://doi.org/10.1016/J.CORSCI.2020.108428.

[409] Palumbo G, King PJ, Aust KT, Erb U, Lichtenberger PC. Grain boundary design and control for intergranular stress-corrosion resistance. Scripta Metall Mater 1991;25:1775–80. https://doi.org/10.1016/0956-716X(91)90303-I.

[410] Taji I, Hajilou T, Ebner AS, Scheiber D, Karimi S, Plesiutschnig E, Ecker W, Barnoush A, Maier-Kiener V, Johnsen R, Razumovskiy VI. Hydrogen assisted intergranular cracking of alloy 725: the effect of boron and copper alloying. Corrosion Sci 2022;203:110331. https://doi.org/10.1016/J.CORSCI.2022.110331.

[411] DeMott RW, Kernion S, Leff AC, Taheri ML. Mitigation of hydrogen embrittlement in alloy custom age 625 PLUS® via grain boundary engineering. Mater Sci Eng 2021;818:141377. https://doi.org/10.1016/J.MSEA.2021.141377.

[412] Kwon YJ, Jung SP, Lee BJ, Lee CS. Grain boundary engineering approach to improve hydrogen embrittlement resistance in FeMnC TWIP steel. Int J Hydrogen Energy 2018;43:10129–40. https://doi.org/10.1016/J.IJHYDENE.2018.04.048.

[413] Kwon YJ, Seo HJ, Kim JN, Lee CS. Effect of grain boundary engineering on hydrogen embrittlement in Fe-Mn-C TWIP steel at various strain rates. Corrosion Sci 2018;142:213–21. https://doi.org/10.1016/J.CORSCI.2018.07.028.

[414] Hu H, Zhao M, Chen S, Rong L. Effect of grain boundary character distribution on hydrogen embrittlement in Fe–Ni based alloy. Mater Sci Eng, A 2020;780:139201. https://doi.org/10.1016/J.MSEA.2020.139201.

[415] Kuzmina M, Herbig M, Ponge D, Sandlöbes S, Raabe D. Linear complexions: confined chemical and structural states at dislocations. Science (1979) 2015;349:1080–3. https://doi.org/10.1126/SCIENCE.AAB2633/SUPPL_FILE/KUZMINA-SM.PDF.

[416] Depover T, Verbeken K. The effect of TiC on the hydrogen induced ductility loss and trapping behavior of Fe-C-Ti alloys. Corrosion Sci 2016;112:308–26. https://doi.org/10.1016/J.CORSCI.2016.07.013.

[417] Depover T, Verbeken K. Hydrogen trapping and hydrogen induced mechanical degradation in lab cast Fe-C-Cr alloys. Mater Sci Eng 2016;669:134–49. https://doi.org/10.1016/J.MSEA.2016.05.018.

[418] Depover T, Verbeken K. Evaluation of the effect of V4C3 precipitates on the hydrogen induced mechanical degradation in Fe-C-V alloys. Mater Sci Eng, A 2016;675:299–313. https://doi.org/10.1016/J.MSEA.2016.08.053.

[419] Depover T, Verbeken K. Evaluation of the role of Mo2C in hydrogen induced ductility loss in Q&T FeCMo alloys. Int J Hydrogen Energy 2016;41:14310–29. https://doi.org/10.1016/J.IJHYDENE.2016.05.176.

[420] Depover T, Monbaliu O, Wallaert E, Verbeken K. Effect of Ti, Mo and Cr based precipitates on the hydrogen trapping and embrittlement of Fe–C–X Q&T alloys. Int J Hydrogen Energy 2015;40:16977–84. https://doi.org/10.1016/J.IJHYDENE.2015.06.157.

[421] Funakawa Y, Shiozaki T, Tomita K, Yamamoto T, Maeda E. Development of high strength hot-rolled sheet steel consisting of ferrite and nanometer-sized carbides. ISIJ Int 2004;44:1945–51. https://doi.org/10.2355/ISIJINTERNATIONAL.44.1945.

[422] Chen CY, Yen HW, Kao FH, Li WC, Huang CY, Yang JR, Wang SH. Precipitation hardening of high-strength low-alloy steels by nanometer-sized carbides. Mater Sci Eng 2009;499:162–6. https://doi.org/10.1016/J.MSEA.2007.11.110.

[423] Asahi H, Hirakami D, Yamasaki S. Hydrogen trapping behavior in vanadium-added steel. ISIJ Int 2003;43:527–33. https://doi.org/10.2355/ISIJINTERNATIONAL.43.527.

[424] Lee J, Lee T, Kwon YJ, Mun DJ, Yoo JY, Lee CS. Effects of vanadium carbides on hydrogen embrittlement of tempered martensitic steel. Metals and Mater Int 2016 2016;22(22):364–72. https://doi.org/10.1007/S12540-016-5631-7. 3.

[425] Turk A, San Martín D, Rivera-Díaz-del-Castillo PEJ, Galindo-Nava EI. Correlation between vanadium carbide size and hydrogen trapping in ferritic steel. Scripta Mater 2018;152:112–6. https://doi.org/10.1016/J.SCRIPTAMAT.2018.04.013.

[426] Zhang S, Wan J, Zhao Q, Liu J, Huang F, Huang Y, Li X. Dual role of nanosized NbC precipitates in hydrogen embrittlement susceptibility of lath martensitic steel. Corrosion Sci 2020;164:108345. https://doi.org/10.1016/J.CORSCI.2019.108345.

[427] Seo HJ, Jo JW, Kim JN, Kwon K, Lee J, Choi S, Lee T, Lee CS. Effect of undissolved Nb carbides on mechanical properties of hydrogen-precharged tempered martensitic steel. Sci Rep 2020;10. <Go to ISI>://WOS:000550057200017.

[428] Zhang S, Xu D, Huang F, Gao W, Wan J, Liu J. Mitigation of hydrogen embrittlement in ultra-high strength lath martensitic steel via Ta microalloying. Mater Des 2021;210:110090. https://doi.org/10.1016/J.MATDES.2021.110090.

[429] Zhang S, Chen W, Huang F, Cheng YF, Li K, Hu Q, Liu J. The significant effect of tantalum on the hydrogen-induced cracking of pipeline steel: morphology,

hydrogen permeation, and theoretical studies. Corrosion Sci 2022;200:110213. https://doi.org/10.1016/J.CORSCI.2022.110213.

[430] Nagao A, Martin ML, Dadfarnia M, Sofronis P, Robertson IM. The effect of nanosized (Ti,Mo)C precipitates on hydrogen embrittlement of tempered lath martensitic steel. Acta Mater 2014;74:244–54. https://doi.org/10.1016/J.ACTAMAT.2014.04.051.

[431] Venezuela J, Blanch J, Zulkiply A, Liu Q, Zhou Q, Zhang M, Atrens A. Further study of the hydrogen embrittlement of martensitic advanced high-strength steel in simulated auto service conditions. Corrosion Sci 2018;135:120–35. https://doi.org/10.1016/J.CORSCI.2018.02.037.

[432] Venezuela J, Zhou Q, Liu Q, Zhang M, Atrens A. Influence of hydrogen on the mechanical and fracture properties of some martensitic advanced high strength steels in simulated service conditions. Corrosion Sci 2016;111:602–24. https://doi.org/10.1016/J.CORSCI.2016.05.040.

[433] Venezuela J, Liu QL, Zhang MX, Zhou QJ, Atrens A. The influence of hydrogen on the mechanical and fracture properties of some martensitic advanced high strength steels studied using the linearly increasing stress test. Corrosion Sci 2015;99:98–117. <Go to ISI>://WOS:000362619900008.

[434] Fielding LCD, Song EJ, Han DK, Bhadeshia HKDH, Suh DW. Hydrogen diffusion and the percolation of austenite in nanostructured bainitic steel. Proc R Soc A 2014:470. https://doi.org/10.1098/RSPA.2014.0108.

[435] Sun B, Krieger W, Rohwerder M, Ponge D, Raabe D. Dependence of hydrogen embrittlement mechanisms on microstructure-driven hydrogen distribution in medium Mn steels. Acta Mater 2020;183:313–28. https://doi.org/10.1016/J.ACTAMAT.2019.11.029.

[436] Sun BH, Lu WJ, Gault B, Ding R, Makineni SK, Wan D, Wu CH, Chen H, Ponge D, Raabe D. Chemical heterogeneity enhances hydrogen resistance in high-strength steels. Nat Mater 2021. <Go to ISI>://WOS:000670863700001.

[437] Korte-Kerzel S, Hickel T, Huber L, Raabe D, Sandlöbes-Haut S, Todorova M, Neugebauer J. Defect phases – thermodynamics and impact on material properties. https://doi.org/10.1080/09506608.2021.1930734; 2021.